

Precision Learning Control for Quasi Static MEMS Mirrors

DIPLOMARBEIT

Ausgeführt zum Zwecke der Erlangung des akademischen Grades eines
Diplom-Ingenieurs (Dipl.-Ing.)

unter der Leitung von
Univ.-Prof. Dr.sc.techn. Georg Schitter
Dr. Han Woong Yoo

eingereicht an der
Technischen Universität Wien
Fakultät für Elektrotechnik und Informationstechnik
Institut für Automatisierungs- und Regelungstechnik

von
Matthias Macho BSc.



Wien, im February 2023

Acknowledgement

At this point I would like to thank all people who supported me through my academic studies and guided me to successfully complete this master's thesis.

I want to thank Prof. Schitter for the possibility to work in this interesting topic, his lecture on mechatronic systems, which gave me a good starting point for this work and for his advice and tips throughout this work.

I would like to thank Dr. Han Woong Yoo for his support and patience. He always managed to find time to give me advice to guide me in the right direction.

Furthermore, I would like to thank my fellow students, who were always there to study with me and having fun together to ease of the stress.

Finally, I want to thank my parents for the opportunity to attend university and especially my girlfriend who always showed a lot of patience with me and for the support till the end.

Abstract

This thesis discusses an advanced learning control for quasi-static (QS) MEMS mirror to enhance the scanning accuracy from the induced errors in switching operation. QS MEMS mirrors are small mirrors that are used to deflect laser beams. They have the ability to hold a static position or track an arbitrary motion. Their actuation principle makes it necessary to switch the inputs during usage. This switching operation introduces unwanted oscillation around the resonant frequency to the trajectory. This thesis proposes two methods to reduce the oscillation.

First, the MEMS scanning system is analyzed for its different error sources with the help of dynamic error budgeting (DEB). Then a frequency-domain iterative learning control (ILC) is designed for QS MEMS mirror to reduce the oscillation by switching operation. The ILC are evaluated for sawtooth reference trajectories with various rates and amplitudes, demonstrates error reduction of the oscillations. At its best in terms of the final RMS errors, the ILC reduces the RMS error to 1.2 millidegree from the 84.8 millidegree in feedforward only case for 2 Hz sawtooth trajectory, reducing by a factor of 69.9. Adding a time-variant Q-filter to the ILC only improved the convergence for the different saw-tooth parameters. As proof of concept, a combination of input shaping and ILC with a lower bandwidth to reduce model error is used. Input shaping is applied by adding impulses shortly after the input switching. The input shaping reduces the oscillation but is not performing as well as the ILC with a wide bandwidth. Combining the ILC with a PD feedback controller also improved reduction of the RMS errors for some cases of scan rates and amplitudes that was not compensated well only with feedforward control while the reduced RMS errors is worse for some cases as well. In conclusion, ILCs and input shaping successfully demonstrate the feasibility of reducing the oscillation introduced by input switching operation of the QS MEMS mirror and DEB confirms that the reduction can reach the limitation of the optical feedback.

Zusammenfassung

Quasistatische MEMS-Spiegel sind kleine Spiegel, die zur Ablenkung von Laserstrahlen verwendet werden. Sie haben die Fähigkeit, eine statische Position zu halten oder eine beliebige Bewegung zu verfolgen. Ihr Aktuator Prinzip macht es erforderlich, die Eingänge während der Nutzung umzuschalten, welches eine unerwünschte Oszillation in der Höhe der Resonanzfrequenz erzeugt. Diese Arbeit schlägt zwei Methoden vor, um die Oszillation zu reduzieren.

Im ersten Schritt wird das System mit Hilfe von DEB auf seine verschiedenen Fehlerquellen analysiert. Die erste Methode zur Reduzierung der Oszillation ist eine frequenzbereich iterativ lernende Regelung (ILR). Insgesamt trägt der ILR dazu bei, die Oszillation zu reduzieren. Im besten Fall reduziert es den RMS-Fehler auf 1,2 Milligrad von 84,8 Milligrad im Fall der reinen Steuerung, was zu einem Faktor von 69,9 führt. Das Hinzufügen eines zeitvarianten Q-Filters zum ILR verbesserte nur die Konvergenz für die verschiedenen Sägezahnparameter. Als Machbarkeitsnachweis wird eine Kombination aus Input Shaping und ILR mit geringerer Bandbreite zur Reduzierung von Modellfehlern verwendet. Input Shaping wird angewendet, indem kurz nach der Eingangsumschaltung Impulse hinzugefügt werden. Input Shaping reduziert die Oszillation, ist aber nicht so effektiv wie der ILR mit einer höheren Bandbreite. Die Kombination des ILR mit einem PD-Regler verbesserte auch die Reduzierung von RMS-Fehlern für die einige Frequenz und Amplituden Kombinationen. ILR und Input Shaping demonstrieren erfolgreich die Machbarkeit der Verringerung der Schwingung, die durch Eingangsumschaltung in einem quasistatischen MEMS-Spiegel eingeführt wird, und DEB bestätigt, dass die Verringerung die Begrenzung der optischen Rückkopplung erreichen kann.

Contents

1	Introduction	1
1.1	State of the Art	2
1.1.1	MEMS Mirror	2
1.1.2	Iterative Learning Control	9
1.1.3	Dynamic Error Budgeting	13
1.1.4	Input Shaping	15
1.2	Problem Formulation and Research Goal	18
2	Experimental Setup and Control Design for QS MEMS Mirror	20
2.1	Experimental Setup	20
2.1.1	PSD-Mirror Distance Calibration	20
2.2	Parameter Identification	24
2.2.1	Identification of Spring Constant and Damping Coefficient	24
2.2.2	Identification of Capacitance Derivative	24
2.3	Flatness-Based Feed-Forward Controller	26
2.4	Feedback Controller	27
3	Dynamic Error Budgeting for QS MEMS Mirror	29
3.1	ADC / DAC Noise Model	30
3.2	Square-root-Gain Circuit Noise Model	32
3.3	Sensor Noise Model	32
3.4	External Vibration Model	32
3.5	Simulation Result of DEB	34
4	Iterative Learning Control for QS MEMS Mirror	37
4.1	Frequency-domain Analysis of the Oscillation Induced by Switching	37
4.2	ILC with Feed-Forward Control	37
4.2.1	Transfer Function	40
4.2.2	Result with Simple Lowpass Filter	40
4.3	ILC with Time-Variant Q-filter	48
4.4	Input Shaping with ILC	51
4.5	ILC with Feedback Control	57

Contents

4.6 Discussion	59
5 Conclusion and Outlook	61
5.1 Conclusion	61
5.2 Outlook	62
Appendix A	69

Die approbierte gedruckte Originalversion dieser Diplomarbeit ist an der TU Wien Bibliothek verfügbar
The approved original version of this thesis is available in print at TU Wien Bibliothek.

List of Figures

1.1 (a) example for electromagnetic mirror [1]. (b) example for piezoelectric mirror [2]	2
1.2 Resonant MEMS mirror design. The rotor and the stator electrode are on the same level	3
1.3 Frequency response of the resonant mirror. The mirror shows jumps at certain frequencies [3].	4
1.4 Quasi-static MEMS mirror design. The rotor and the stator electrode are on different level. [4]	4
1.5 Process of creating the different layer for the mirror	5
1.6 Concept of the electrostatic comb drive	5
1.7 Capacitance derivative of the two input from the mirror.	6
1.8 Measured resonance frequency changes over the tilting angle and the estimated electrostatic stiffness k_{el} from the capacitance measurements.	7
1.9 Example for Sliding mode controller	8
1.10 Block diagram of ILC concept. The input signal for the new iteration step depends on the error of the last iteration step.	9
1.11 Example for the effect of the stabilisation methods for inverse models	11
1.12 Example for Phase error	14
1.13 Block diagram of a system for DEB analysis	15
1.14 Response of system for two input impulses	16
1.15 Input shaping for triangular signal	17
1.16 Example for oscillation introduce through input switching	18
2.1 Block diagram of the Mirror setup	21
2.2 Photo of the real setup.	22
2.3 Block diagram of the setup with ILC together	22
2.4 Example of calibration process of the PSD Setup	23
2.5 Calibration process of the test bench	23
2.6 Decay curve of mirror after voltage impulse.	25
2.7 Capacitance derivative curve	26
3.1 Block diagram of the system for DEB analysis	29

List of Figures

3.2	Block diagram of the σ_{adc} conversion to angular signal	31
3.3	Spectrum of the vibration load LV124[5]	33
3.4	Vibration torque model of the mirror	33
3.5	PSD of the different disturbance sources at the output (a) shows the <i>PSDs</i> for 0° operation point. (b) shows the <i>PSDs</i> for 4° operation point	35
3.6	CPS of the different disturbance sources at the output. A spike at 50 Hz is visible. (a) shows the CPS for 0° operation point. (b) shows the CPS for 4° operation point	36
4.1	FFT of the error signal for different frequencies and different amplitudes.	38
4.2	FFT of the error signal for different frequencies and different amplitudes.	39
4.3	Block diagram of the ILC setup	40
4.4	Block diagram of the setup for measuring the transfer function of the mirror at the different angular operation points for the ILC input signal.	41
4.5	Comparison of transfer function for different operation point.	41
4.6	Result for ILC with simple low-pass filter	43
4.7	RMS error for the feedforward only case	44
4.8	RMS error for the feedforward only case	44
4.9	RMS error ILC with simple low-pass filter	45
4.10	3 different result for the ILC with simple Q-filter.	46
4.11	3 different input signal for the ILC with simple Q-filter.	47
4.12	RMS error for time variant Q-filter	49
4.13	Comparison of convergence of ILC with lowpass filter and time-variant Q-filter	49
4.14	Performance factor diagram for time variant Q-filter	50
4.15	Two different results for the time variant Q-filter	50
4.16	Result of the input shaping combined with ILC for sawtooth trajectory with an amplitude of 2° and a frequency of 2 Hz.	52
4.17	RMS error for the feedforward only case.	53
4.18	RMS error for the feedforward with input shaping and ILC case.	53
4.19	Performance-diagram for input-shaping	54
4.20	Four different sawtooth parameter angle signal comparison between ILC with simple low-pass filter and ILC combined with input shaping.	55
4.21	Four different sawtooth parameter error signal comparison between ILC with simple low-pass Q-filter and ILC combined with input shaping.	56
4.22	block diagram of the feedback controller together with the feed forward signal	57
4.23	RMS error for the feedforward with feedback only case.	58
4.24	RMS error for the feedforward with feedback and ILC case.	58
4.25	Performance factor diagram ILC with feedback controller	59
4.26	Two different results for the feedback with simple low-pass Q-filter.	60
1	RMS error in milidegree of the feedforward control only case	69
2	RMS error of the flatness-based feedforward control with ILC	70
3	RMS error in milidegree of the flatness-based feedforward control with ILC and time-variant Q-filter	70

List of Figures

4	RMS error in milidegree of the input shaping with ILC	71
5	RMS error in milidegree of the flatness-based feedforward control with ILC and PD-feedback controller	71

Die approbierte gedruckte Originalversion dieser Diplomarbeit ist an der TU Wien Bibliothek verfügbar
The approved original version of this thesis is available in print at TU Wien Bibliothek.



Acronyms

<i>PSD</i>	power spectral density
AFM	atomic force microscopy
CPS	cumulative power spectrum
DEB	dynamic error budgeting
FFT	Fast Fourier Transform
ILC	iterative learning control
ISMC	integral sliding mode control
LIDAR	light deflection and ranging
MEMS	micro-electro-mechanic system
PSD	position sensitive device

Symbols

$\hat{\theta}$	Calculated angular velocity
C_1	Capacitance between stator and rotor electrode 1
C_2	Capacitance between stator and rotor electrode 2
J	Torque inertia of the mirror
$L(\mathbf{q})$	Learning filter
$P^{-1}(j\omega)$	Measured inversion of the system
$Q(\mathbf{q})$	Q-filter
U_j	Discrete Fourier transformed input
$\dot{\theta}_d$	Desired angular velocity
$\hat{P}^{-1}(j\omega)$	Measured inversion of the system
$\hat{\theta}$	Calculated angle
\mathbf{q}	Forward time-shift operator
$\rho(j\omega)$	Learning gain
θ	rotation angle
θ_d	Desired angle
b	Damping coefficient of mirror
d	Distance between PSD and mirror
e	Error between the desired system output y_d and the measured output y_m
f_r	Fundamental frequency
f_s	Sample rate
i	Iteration index
j	Imaginary unit
k	Time index
k_0	Spring constant
y_d	Desired output
y_m	Measured output

CHAPTER 1

Introduction

MEMS mirror stands for micro-electro-mechanical system mirror, which means that through an electrical signal the mirror can be moved around different axes. These mirrors can perform a high dynamic and precise beam position for various applications such as light deflection and ranging (LIDAR) [6], laser projectors[7] or endoscopy [8]. The benefits are small sized mirrors and the possibility of manufacturing the mirror from a single silicon chip through a fully compatible CMOS process [9]. There are many actuation concepts for the mirror. In most concepts, an electrostatic force [10, 11] is used, but other concepts such as electromagnetic [12], electrothermal [13] or piezoelectric [14] are considered and applied. One state of the art mirrors are the electrostatic resonant mirror [9]. These mirrors oscillate in their resonance frequency, which can go up to 50 kHz[15]. The disadvantage of the resonance mirror is that one dimensional mirrors only have a sinusoidal trajectory and the two-dimensional the Lissajous figure. The quasi-static MEMS mirror does not have this disadvantage but has a lower resonance frequency. The design concept makes it possible to hold a static position or track an arbitrary motion. These mirrors are typically driven with a triangular or sawtooth trajectory for line-scanning motion. One of the problems of the quasi-static mirror is the low damping of the system, which makes it necessary to use a controller. The quasi-static mirror with electrostatic force as an actuation concept can be produced in CMOS-compatible processes, which is well established in the industry. The actuation works by applying a voltage at one input of the mirror. The electrostatic force then pulls the mirror to one side. To rotate the mirror to the other electrode, a voltage has to be applied to the input on the other site. Therefore, during driving the mirror with wide angle trajectories, it is necessary to switch the input. This switching of the input introduces unwanted oscillation, around the resonance frequency, in the trajectory of the mirror. This work focuses on the design of two controller designs to reduce these unwanted oscillations. As a scanning trajectory, a sawtooth signal is used for typical line scanning behavior of the mirror. Since in scanning applications repeating trajectories are used, one of the reduction methods is going to be an iterative learning controller. A second method for repeating trajectories is input shaping. Also, an important step for

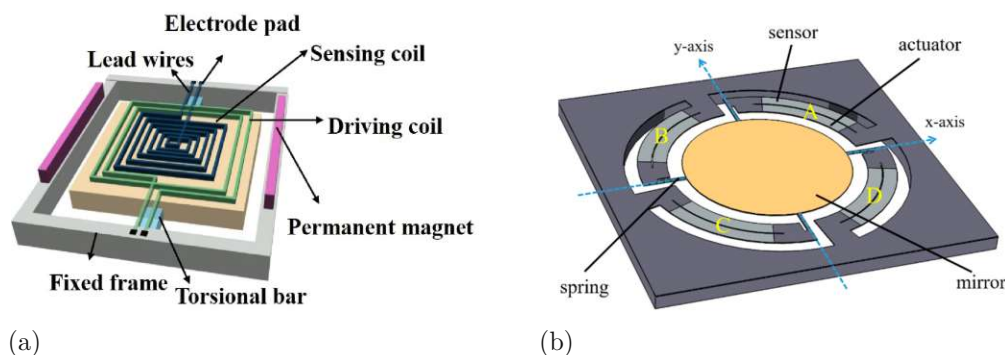


Figure 1.1: (a) example for electromagnetic mirror [1]. (b) example for piezoelectric mirror [2]

designing a controller is the analysis of the different error sources. Therefore, in this work, the system is analyzed by dynamic error budgeting. This provides the possibility of seeing the best performances, which can be achieved for the system.

1.1 State of the Art

1.1.1 MEMS Mirror

For micro-electro-mechanic system (MEMS) mirrors, there are various types of actuation such as electromagnetic, electrostatic or piezoelectric actuation. Electromagnetic actuation works on the principle that the scanner has metal coils on it and is disposed in a static magnetic field generated by a permanent magnet [16]. These type of mirror have the benefit of high torque compared to electrostatic actuation, which can be used to increase the opening angle and robustness of the device [17]. The drawbacks are increased power consumption and a bulkier design due to integrated magnets [18]. Example for a electromagnetic mirror can be seen in 1.1(a). MEMS mirrors with a piezoelectric actuator work by having an outer frame with a piezoelectric ceramic film. Applying voltage to this film deforms it, which then moves the mirror on the inner frame [19]. They have the benefit of providing high force with low power consumption and do not require additional bulky elements and do not have a large displacement compared to the other actuation method. The piezoelectric mirror also requires adding the piezoelectric film, which adds to the production cost [20]. Example for a piezoelectrical mirror can be seen in 1.1(b). Although electrostatic actuated mirrors require high voltages, they still have good displacement and can be quite compact [21]. Since they can be produced through CMOS-technology, they are quite often used in the industry [22].

Electrostatic Resonant MEMS Mirror

Figure 1.2 shows a structure of a resonant MEMS mirror. The mirror has a movable part, which include the mirror and combs electrodes on each end. The movable part is connected to the static part over springs. The stator part has the opposing electrode.

1 Introduction

The mirror is actuated by applying a voltage between the stator combs electrodes and

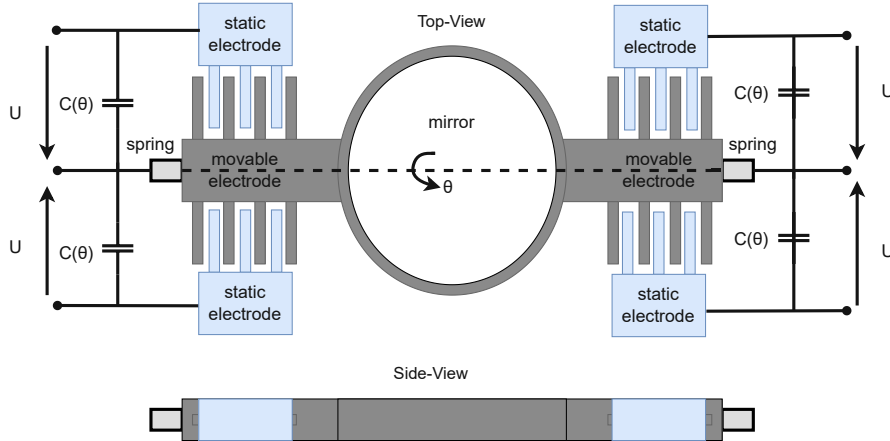


Figure 1.2: Resonant MEMS mirror design. The rotor and the stator electrode are on the same level

the combs electrodes of the movable part. As typical for electrostatic actuation the generated torque can be described through a non-linear function,

$$\tau = \frac{1}{2} \frac{\partial C(\theta)}{\partial \theta} u^2. \quad (1.1)$$

The design of the mirror in combination with the actuation principle only allows a pulling force to the rest position of the mirror. This behavior can be seen as a voltage controllable spring with a positive nonlinear stiffness, where the total mirror stiffness is a combination of the mechanical stiffness and electrostatic stiffness coming from the electrostatic force. By applying a nonlinear voltage the total stiffness of the system can be manipulated and the mirror start to oscillated. This phenomena is called parametric excitation [23]. These parametric oscillator response with a large amplitude for a small excitation, when operated at frequencies around $2f_c/n$, where f_c is the natural frequency of the system and $n \in \mathbb{N}$ is the order of parametric resonance. The mirror response always with an oscillation close to f_c independently of the parametric order, but for the first order the mirror has the highest response. The best result is achieved when the driving voltage is switch on at the maximum deflection and switch off a the zero crossing [24].

Typical behavior of these mirror is that the have multiple stable and unstable frequency responses. The frequency response shows hysteresis between up- and down-sweep and also jumps (bifurcations) [3]. This behavior can be seen in Figure 1.3. The mirror can be treated as a single degree of freedom (DOF) system with the general equation of motion [23]

$$J\ddot{\theta} + b(\theta)\dot{\theta} + k(\theta)\theta = \tau(\theta), \quad (1.2)$$

where J is the torque inertia of the mirror. $b(\theta)$ as damping term and $k(\theta)$ as stiffness term. All term except the torque inertia are nonlinear function depending on the deflection angle [25].

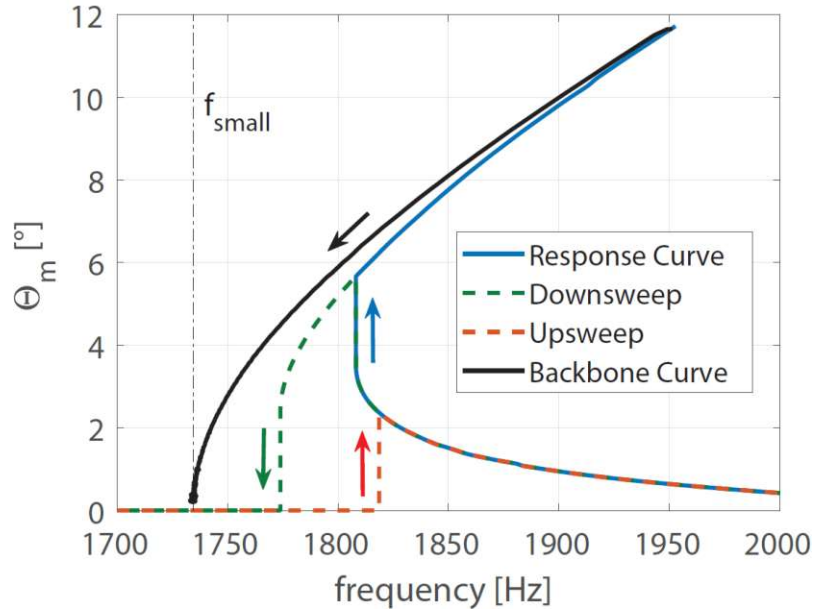


Figure 1.3: Frequency response of the resonant mirror. The mirror shows jumps at certain frequencies [3].

Electrostatic Quasi-static MEMS Mirror

The quasi-static MEMS mirror with electrostatic actuation principle is manufactured from a single silicon chip through a fully compatible CMOS process [9]. Figure 1.4 shows a structure of quasi-static MEMS mirror. The mirror consists of a movable part and four stator electrodes. The movable part contains the mirror itself and the rotor electrodes. The springs on the end connect the moving part to the rest of the mirror. The stator electrodes are one level down. Together with the rotor electrode, the stator electrode builds a comb-shaped structure. The mirror layers are first created

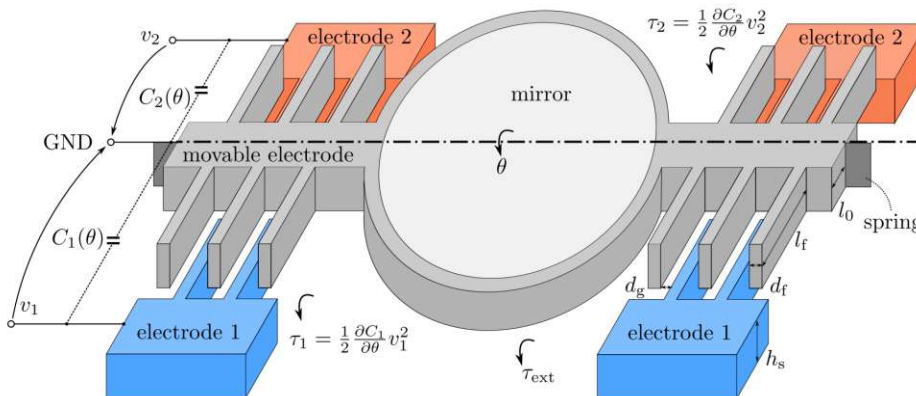


Figure 1.4: Quasi-static MEMS mirror design. The rotor and the stator electrode are on different level. [4]

on the same level and then pressed down with the help of a stamp, which is visible in Figure 1.5 [26]. This procedure is quite delicate and is one reason for uncertainties in the mirror model. From the four stator electrodes the two on the same side build an

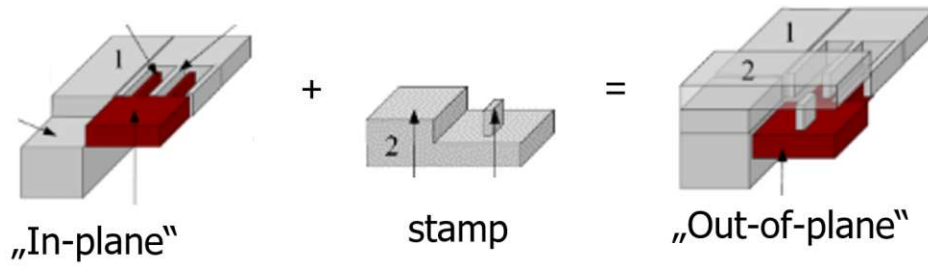


Figure 1.5: Process of creating the different layer for the mirror. The rotor and stator level are first created on the same level. The rotor layer is then pressed down to a different level with the help of a stamp.[26]

input pair, which altogether gives two inputs for the mirror. The mirror is actuated by an electrostatic force. By applying a voltage between the stator electrode pair and the rotor electrode, the mirror will be pulled to the other side, 1.6(b). The springs at the

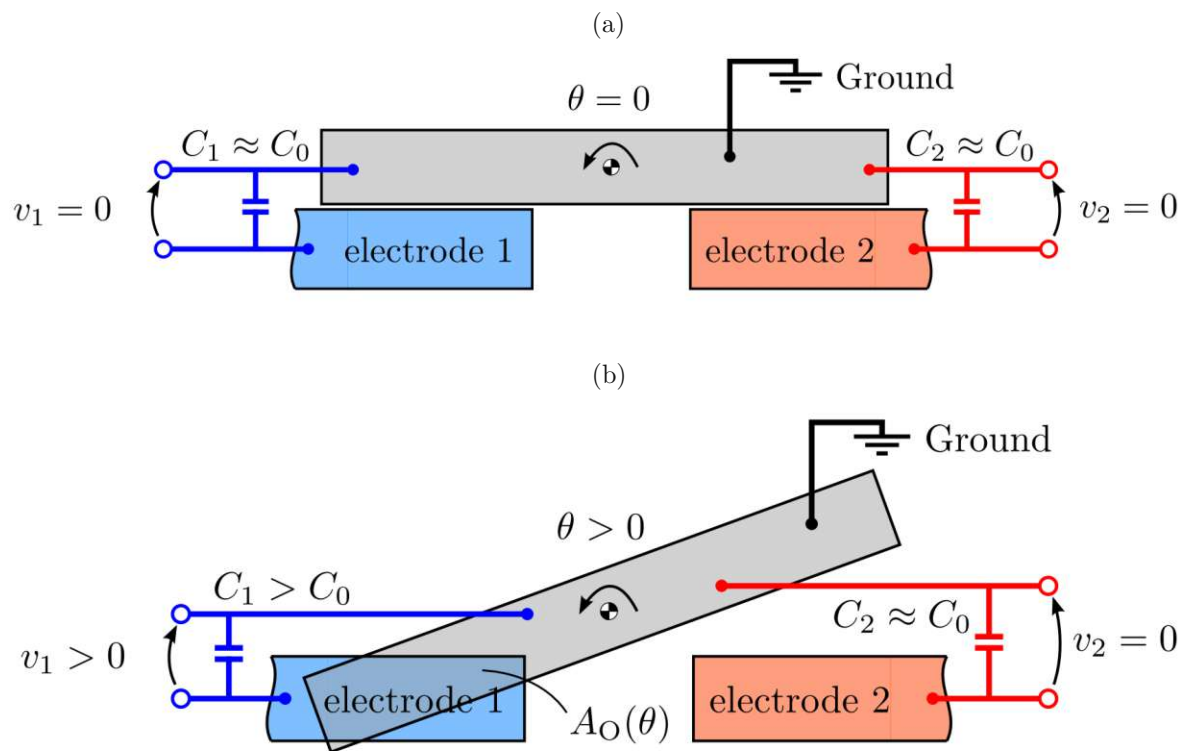


Figure 1.6: Concept of the electrostatic comb drive. (a) show the mirror when no voltage is applied between the electrode. The stator and actor electrode have to be on different levels. (b) When a voltage is applied between the two electrode, a electrostatic torque rotates the mirror to our side. The springs on the rotor apply a counter torque. [4]

edges produce a torque directed in the opposite direction, which allows one to hold the mirror at an arbitrary angle. Since the electrostatic force is only a pulling force, two inputs are necessary. One input is to tilt the mirror with a positive angle, and one is to

1 Introduction

tilt the mirror with a negative angle. The torque, which is generated from the comb drive, is proportional to the change of capacitance of the stator and rotor electrode,

$$\tau = \frac{1}{2} \frac{\partial C(\theta)}{\partial \theta} u^2. \quad (1.3)$$

The capacitance derivative of the mirror used in this project can be seen in [Figure 1.7](#). The mirror itself can be modelled as a spring mass damper system with the electrostatic

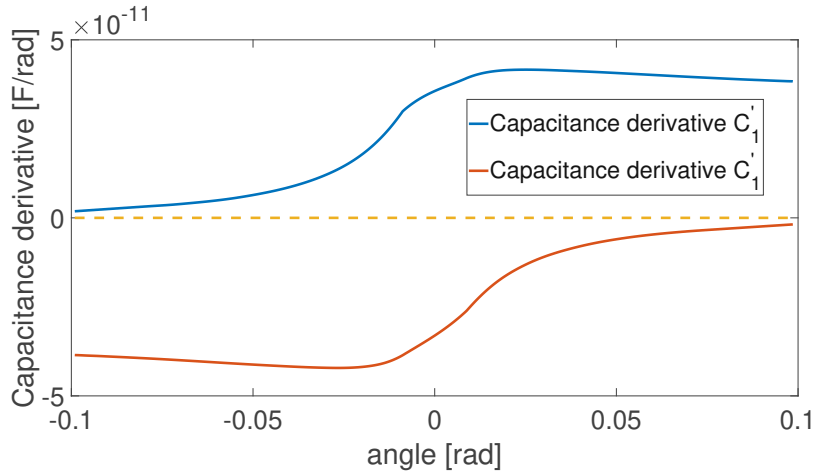


Figure 1.7: Capacitance derivative of the two input from the mirror.

force as an external torque.

$$J\ddot{\theta} + b\dot{\theta} + k_0\theta = \frac{1}{2} \frac{\partial C_1(\theta)}{\partial \theta} u_1^2 + \frac{1}{2} \frac{\partial C_2(\theta)}{\partial \theta} u_2^2, \quad (1.4)$$

where J is the torque inertia of the mirror. b describe the damping coefficient, k_0 the spring constant and C_1 and C_2 the capacitance between the stator and rotor electrodes. The mirror is a low-damped system with a high Q-factor around 90.

Resonance Shift

One important characteristic of the mirror is that it experiences a softening or stiffening of the overall stiffness of the system depending on the current tiling angle [4]. This effect can be seen in the transfer function. To obtain the transfer function, [Equation 1.4](#) is approximated with a Taylor series at the current operation point θ_{op} and u_{op} . Only one input force is used because the mirror is always driven by applying voltage to one of the inputs.

$$J\Delta\ddot{\theta} + b\Delta\dot{\theta} + k_0\Delta\theta = k_{el}\Delta\theta + K_{el}\Delta u, \quad (1.5)$$

with the local linear parameter,

$$k_{el} = \frac{1}{2} \left. \frac{\partial^2 C(\theta)}{\partial \theta^2} u^2 \right|_{\theta=\theta_{op}, u=u_{op}}, \quad (1.6)$$

1 Introduction

as electrostatic stiffness and

$$K_{el} = \left. \frac{\partial C(\theta)}{\partial \theta} u \right|_{\theta=\theta_{op}, u=u_{op}}, \quad (1.7)$$

as the voltage coefficient. Equation 1.5 is then Laplace transformed to get the transfer function at the operation point,

$$G = \frac{K_{el}}{Js^2 + bs + k_0 - k_{el}}, \quad (1.8)$$

where $k_0 - k_{el}$ is the total stiffness of the system. Since k_{el} depends on the tilt angle, the stiffness changes at different operating points. Together with the stiffness, the resonance frequency of the mirror also changes. The shift of the resonance frequency adds a challenge to the designing of a controller.

Figure 1.8 shows the resonance frequency at different operating points, together with the electrostatic stiffness. It first drops to a minimum at 0.5° and then increases again. The resonance frequency was determined by measuring the mirror transfer function (cf. subsection 4.2.1. k_{el} was calculated with the measured mirror parameters.

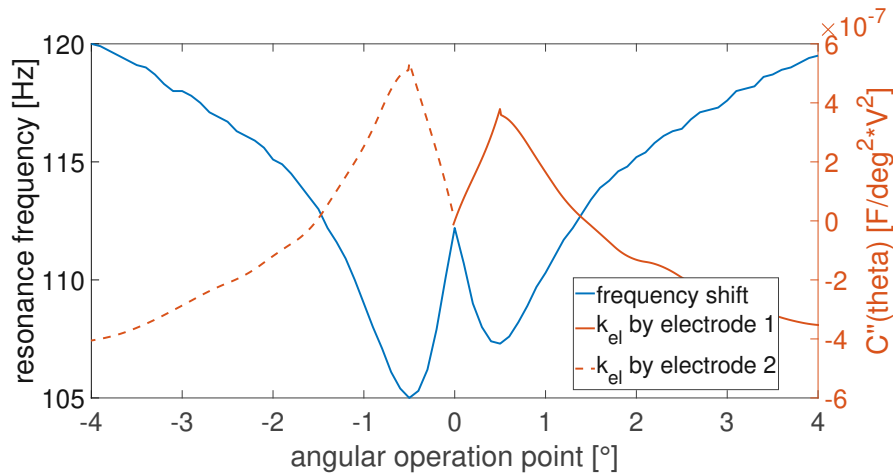


Figure 1.8: Measured resonance frequency changes over the tilting angle and the estimated electrostatic stiffness k_{el} from the capacitance measurements.

MEMS Mirror Controller Methods

Similar to the actuation principle, there exist various controller methods for MEMS mirrors. The first controller design implemented for MEMS mirrors is a PID [11, 27]. Both papers use two PID controllers for each axis of a 2D electrostatic MEMS mirror. The PID controllers are compared to a steady-state feed-forward controller. Both PIDs have a faster settling time and a lower overshoot for an angular step signal. A possibility of better linearization is to use a square root block between the PID controller and mirror [11].

As an other controller method an integral sliding mode control (ISMC) for a electromagnetic actuated polymer MEMS mirror is proposed [12]. ISMC is a non-linear feedback

controller. Its benefits are a fast system response and insensitivity to plant uncertainties. The idea behind ISMC is that the error trajectory in the error state-space slides along a certain surface to the origin. During this sliding, the error oscillates around this surface, an example for the sliding can be seen in Figure 1.9 To decrease the steady-state error,

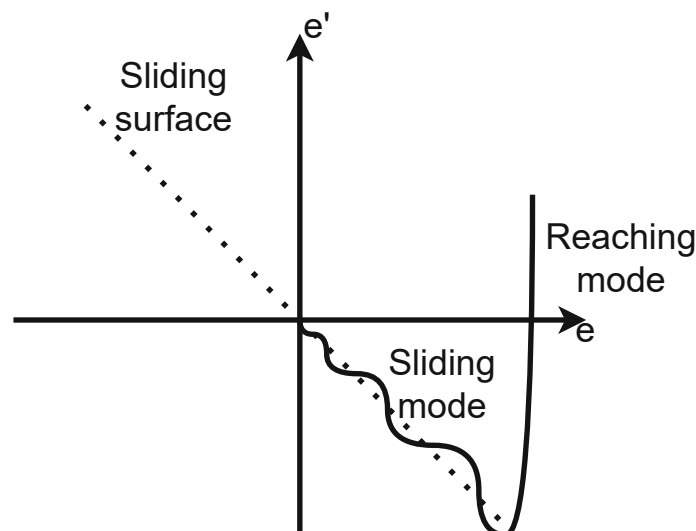


Figure 1.9: Example for Sliding mode controller. In the reaching mode, the error trajectory moves to the sliding surface. In the sliding mode the error trajectory oscillates around the sliding surface to the origin

an integrator part is added. The ISMC is compared to the feed-forward open-loop system, where the new controller shows an improvement of the settling time from 50 ms to 10 ms, without overshoot. Also, compared to a closed-loop PID controller, an improvement could be seen by a lower position error. The performance of the ISMC for tracking the ability of a triangular trajectory is also evaluated. The test result also shows an improvement in performance compared to the open-loop and PID controller. A disadvantage of the sliding mode controller is high frequency actuation, called chattering, due to the fast change of the input signal along the sliding surface [28, 29]. In the previous paper [29] a feed-forward controller based on steady-state signal is used to show the performance of the sliding mode controller. In [10] an advanced feed-forward controller for electrostatic MEMS mirror is introduced by using the property that the input and system states can be written as functions of the output and its derivatives, which is called differential flat. Through the flat output, the necessary input for a desired trajectory can be calculated. On the contrary to the steady-state feed-forward controller, this method is also useful for dynamic trajectories. The flatness-based feedforward controller shows a mean error of 30 millidegrees for a triangular trajectory with 10 Hz and 5° amplitude. This result was then improved by adding a closed-loop PID controller to the system. This reduced the mean error down to 7 millidegrees

1.1.2 Iterative Learning Control

Iterative learning control (ILC) is a type of learnt feed-forward control. The basic idea is that the performance of the system, which executes the same task repeatedly, can be improved by learning from the previous execution. This method makes the ILC ideal for reducing repeating error. [30, 31]

The ILC learning algorithm is often described as

$$u_{i+1}(k) = Q(\mathbf{q})[u_i(k) + L(\mathbf{q})e_i(k)], \quad (1.9)$$

where i is the iteration index, k is the time index and \mathbf{q} is the forward time-shift operator $\mathbf{q}x(k) \equiv x(k+1)$. e is the error between the desired system output y_d and the measured output y_m ,

$$e_i(k) = y_{i,m}(k) - y_{i,d}(k). \quad (1.10)$$

The block diagram of ILC can also be seen in Figure 1.10.

$L(\mathbf{q})$ is the learning filter or learning function described as a proper rational function of \mathbf{q} and $Q(\mathbf{q})$ is the called Q-filter.

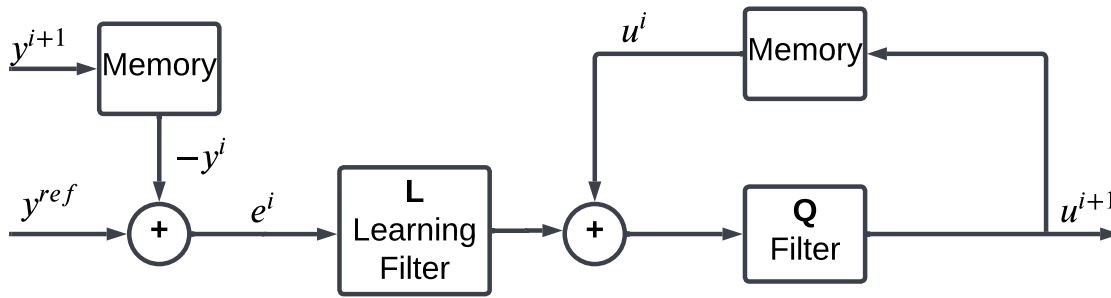


Figure 1.10: Block diagram of ILC concept. The input signal for the new iteration step depends on the error of the last iteration step.

Learning Filter

The learning filter defines behavior of the the ILC and its conversion rate. There are many methods for designing the learning filter. The PD-Type uses the well-known concept of the PID-Controller. Similarly to the PID-controller, the PD learning filter is often just tuned in and, therefore, does not require an accurate model of the system. In contrast to the PID-controller the learning filter normally does not use an integration part, because the learning algorithm already has an integration behavior. [32, 33].

Inverse Model Learning Filter

The idea to use the inverse model P^{-1} as learning filter comes from the solution to set the of the error evolution equation zero. The error evolution equation for ILC in the frequency domain is

$$E_{i+1}(z) = (1 - P(z)L(z))E_i(n). \quad (1.11)$$

As a note, this is the simplified error evolution equation, where Q-filter $Q(z) = 1$. The learning filter is typically designed as $L(z) = \rho \hat{P}^{-1}(z)$, where $\hat{P}(z)$ is the designed system model and ρ the learning gain with the characteristic that for a smaller learning gain the robustness to model error increases. One of the major challenges in using the inversion based design lies on stable inversion of a non-minimum phase plant model. To guarantee a stable learning filter two methods can be used, the zero phase approximation [34] and the time delay approximation [35]. The zero phase approximation method is based on the zero phase error tracking control. It is assumed that the plant model can be represented as

$$P(z) = \frac{B^u(z)B^s(z)z^{-k_d}}{A(z)}, \quad (1.12)$$

where $B^s(z)$ are the minimum phase zeros, $B^u(z)$ the non-minimum phase zeros, $A(z)$ the poles of the plant and z^{-k_d} a time delay. The zero phase approximation of the model inversion is then

$$\hat{P}_{zp}^{-1}(z) = \frac{A(z)B^u(z^{-1})z^{k_d}}{(B^u(1))^2 B^s(z)}. \quad (1.13)$$

Through the inversion, the time delay changes to a time advance. Since the ILC works with a recorded measurement, the time advance can be implemented by shifting either the input signal or the output signal. An example of the effect of the zero phase approximation can be seen in Figure 1.11. The zero phase approximation gives a good approximation for the model phase, but clearly diverges from the plant magnitude at higher frequencies. In the case of the time delay approximation the system with the non-minimum phase zeros is approximated with a system with only minimum phase zeros and a time delay.

$$\hat{P}_{td}^{-1}(z) = \frac{A(z)z^{k_d+k_a}}{\hat{B}^u(z)B^s(z)}, \quad (1.14)$$

where $\hat{B}^u(z)$ are an approximated minimum phase zeros and k_a is an additional input delay for phase correction. The effect of this method can be seen again in Figure 1.11. This time the method gives a good approximation for the magnitude but shows a phase error. Also visible is an example for the time delay approximation without the addition time delay, where the phase error is much greater.

A typically the inverse model method is used in the time domain. However, the time domain has the disadvantages that for a stable inverse the previously discussed methods have to be used for non-minimum phase systems and every time the next iteration is calculated a convolution together with signal padding have to be done. A better solution is to use the inverse model method in the frequency domain since in the frequency domain non-minimum phase system can be used without mentioned extra steps [37].

Frequency-domain ILC

The idea of the frequency-domain ILC is based on the desired output signal y_d and the input signal for every iteration u_i being periodic with length N , the signal can be represented by a limited number of harmonic frequencies of the fundamental frequency $f_r = f_s/N$ with f_s as the sample rate [38]. The ILC can then be design in frequency domain,

$$U_{i+1}(n) = U_i(n) + \rho(j\omega)\hat{P}^{-1}(n)E_i(n), \quad (1.15)$$

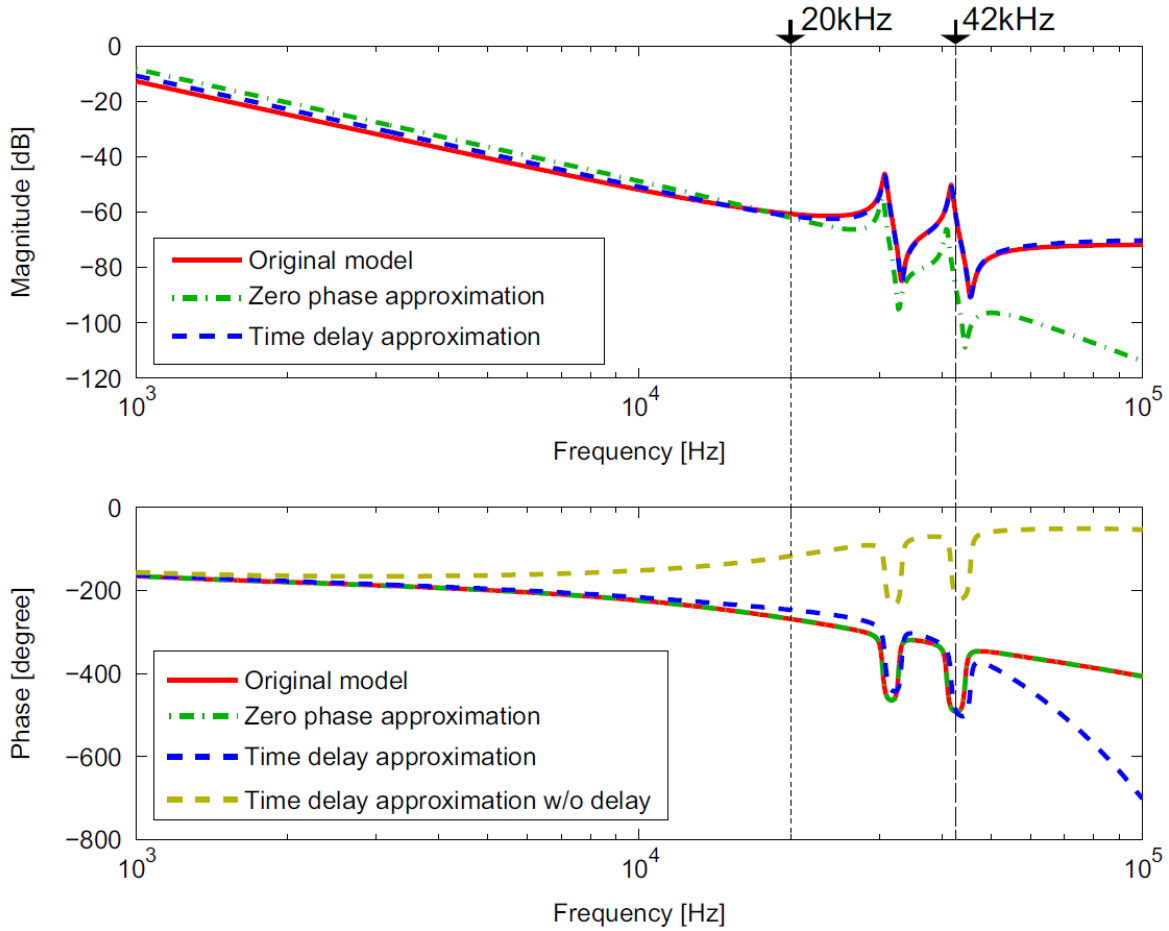


Figure 1.11: Example for the effect of the stabilisation methods for inverse models. The original model is a galvanometer scanner [36]

where the capital letters represent the discrete Fourier transform coefficients defined as

$$X_i(n) = \sum_{k=0}^{N-1} x_i e^{-j \frac{2\pi}{N} nk}, \quad (1.16)$$

and n is the index of harmonic frequencies for the fundamental frequency $\frac{2\pi}{N}$. $\rho(j\omega)\hat{P}^{-1}$ is the learning filter which uses measured inversion of the system $\hat{P}^{-1}(j\omega)$ and a learning gain $\rho(j\omega)$. The learning gain is so selected that

$$\rho = \begin{cases} r & \text{for } \omega \leq \omega_B \\ 0 & \text{for } \omega > \omega_B, \end{cases} \quad (1.17)$$

with $r \leq 1$ and ω_B as cutoff frequency, which is selected as a frequency higher than the highest frequency component of the error signal. r decided the convergence rate of the ILC, but also its robustness.

Model-Free ILC

Model-Free ILC incorporates the system identification during learning. This removes

the need for a dynamic system model and the related modelling process [39]. This method of ILC is used when a reasonable frequency response cannot be measured [40]. The model-free ILC algorithm often treats the plant as a linear system, like the secant method [41]. There are also algorithms for certain nonlinear systems. In [42] an algorithm based on the Newton method is proposed, which can also handle nonlinearity to a certain degree. A steepest-descent algorithm for nonlinear systems is proposed in [43].

Q-Filter

The Q-filter is used to reject learning from non-repeating disturbance and measurement noise and increase the robustness of the ILC. It comes with the trade-off of reduced performance. The simplest Q-filter is a low-pass filter to reject the higher frequency part, which is not included in the repeating error and would only include noise.

Time-Variant Q-Filter

Time-variant Q-filters have the combined characteristics of different filters. They give the enhanced robustness of low bandwidth filter, while taking advantage of the performance of high bandwidth Q-filter [44]. In [45] a linear time-variant Q-filter is proposed for a micro-scale robotic deposition system. The mix of motion with high acceleration and constant velocity for high precision makes it necessary to have a filter with changing bandwidth. To design the time-variant low-pass filter, the ILC learning algorithm from Equation 1.9 is written in the lifted-system representation Equation 1.18, which is described in more detail in [33]. The components of the vector are the values at different time steps. i is the iteration index. The components of the matrix are the impulse response components. Non-zero values in the upper triangular means that the filter is a zero-phase filter. Since ILC uses a sequence of N -sample, an acausal filter can be used and would also be recommended to not have a time delay in the calculated signal.

$$\underbrace{\begin{pmatrix} u_{i+1}(0) \\ u_{i+1}(1) \\ \vdots \\ u_{i+1}(N-1) \end{pmatrix}}_{u_{i+1}} = \underbrace{\begin{pmatrix} q_0 & q_{-1} & \cdots & q_{-(N-1)} \\ q_1 & q_0 & \cdots & q_{-(N-2)} \\ \vdots & \vdots & \ddots & \vdots \\ q_{N-1} & q_{N-2} & \cdots & q(0) \end{pmatrix}}_Q \cdot \underbrace{\begin{pmatrix} u_i(0) \\ u_i(1) \\ \vdots \\ u_i(N) \end{pmatrix}}_{u_j} + \underbrace{\begin{pmatrix} l_0 & l_{-1} & \cdots & l_{-(N-1)} \\ l_1 & l_0 & \cdots & l_{-(N-2)} \\ \vdots & \vdots & \ddots & \vdots \\ l_{N-1} & l_{N-1} & \cdots & l(0) \end{pmatrix}}_L \underbrace{\begin{pmatrix} e_i(0) \\ e_i(1) \\ \vdots \\ e_i(N) \end{pmatrix}}_{e_j} \quad (1.18)$$

Since the rows in the filter matrix describe the values at different time steps to obtain a filter which has a certain characteristic at a certain time step, the component of the impulse response has to be in the right row. The matrix Equation 1.19

$$Q = \begin{pmatrix} q_0^1 & q_{-1}^1 & \cdots & q_{-(N-1)}^1 \\ q_1^1 & q_0^1 & \cdots & q_{-(N-2)}^1 \\ q_2^2 & q_1^2 & \cdots & q_{-(N-3)}^2 \\ \vdots & \vdots & \ddots & \vdots \\ q_{N-1}^2 & q_{N-2}^2 & \cdots & q_{(0)}^2 \end{pmatrix}, \quad (1.19)$$

shows an example of a time variant filter, which is combined with different filters. The upper indices 1 and 2 are the filter indices for filter 1 and 2.

Problem with Model Error for ILC

The ILC is asymptotically stable if and only if

$$\|Q(j\omega) [1 - \rho(j\omega)\tilde{L}(j\omega)P(j\omega)]\| < 1, \forall \omega. \quad (1.20)$$

Entering the measured inverse system transfer function $\hat{P}^{-1}(j\omega)$ for $\tilde{L}(j\omega)$ leads to

$$\tilde{L}(j\omega)P(j\omega) = \hat{P}^{-1}(j\omega)P(j\omega) = (P(j\omega) + \Delta(j\omega))^{-1}P(j\omega) = \Delta_m(j\omega)e^{j\Delta_\theta(\omega)}. \quad (1.21)$$

Since the measured model always has a certain error, we get the gain error $\Delta_m(j\omega)$ and the phase error $e^{j\Delta_\theta(\omega)}$. For a Q-filter $Q(j\omega) = 1$ the phase error must be $\Delta_\theta(\omega) < 90^\circ$. Instability can occur for non-linear systems, where the resonance frequency depends on the operation point. In [Figure 1.12](#) the transfer functions of the quasi-static MEMS mirror are shown for two operation points, -1° and -4° . If one of the transfer functions is used as the inverse system $\hat{P}^{-1}(j\omega)$ in ILC, because of the low damping of the mirror, in a certain frequency range, the error between the two transfer functions would be 180° and therefore lead to an unstable ILC. This could lead to a performance problem with the ILC. Adding an Q-filter beside the trivial $Q(j\omega) = 1$ would increase the convergence radius[46].

ILC for Optical Scanning Application

Optical scanning devices usually use a repeating pattern as their scanning trajectory, which makes the use of learning-type control algorithms like ILC ideal. The use of ILC can reduce the need for real-time feedback control by training the device a priori and saving the resulting waveform in the MEMS controller [47]. Some usage of ILC in optical scanning application can be, reduction of overshoot and settling time for near-field scanning optical microscope [48] and improving the profile tracing for selective laser melting application [49].

1.1.3 Dynamic Error Budgeting

Dynamic Error Budgeting (DEB) is a tool to calculate the effect of different noise sources on the output of a system. DEB makes it possible to combine stochastic signals (disturbance) with Bode plots[50, 51]. When working with normal distributed stochastic signals, the system performance is typically measured with the standard deviation σ of

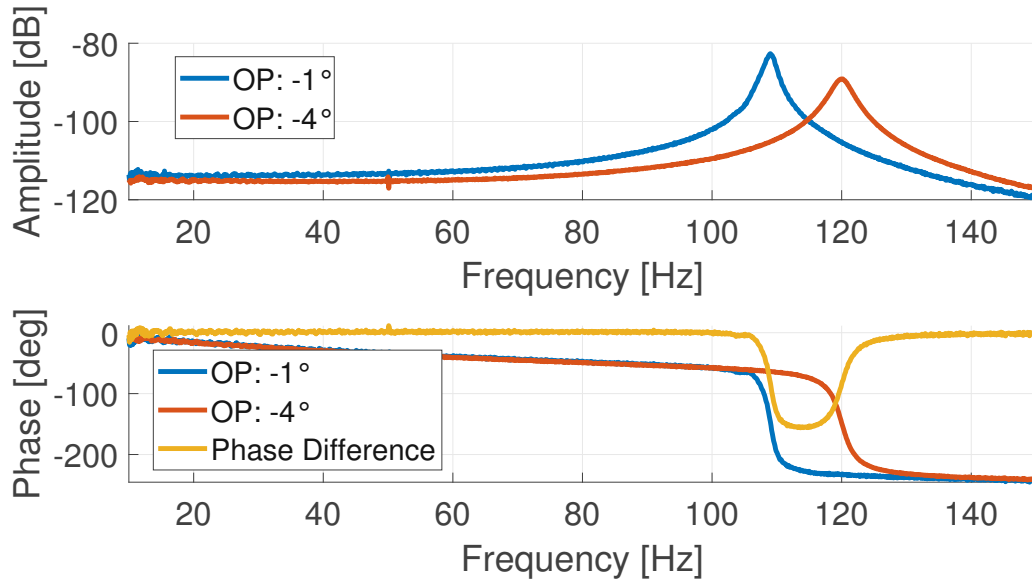


Figure 1.12: Resonance frequency shift of the MEMS mirror depending on the angular operation point. This leads to a phase difference of 180° for a certain frequency range between the different transfer functions

the signal $x(t)$, which is the square root of the variance,

$$\sigma^2 = \|x - \bar{x}\|^2 = \lim_{T \rightarrow \infty} \frac{1}{2T} \int_{-T}^T (x(t) - \bar{x})^2 dt. \quad (1.22)$$

For the DEB the DC components \bar{x} are normally not considered, and therefore can be set to 0. Using Parseval's theorem, the standard deviation is connected to the frequency domain. Parseval's theorem also states that the energy in the time domain equals the energy in the frequency domain,

$$\sigma^2 = \|x\|^2 = \lim_{T \rightarrow \infty} \frac{1}{2T} \int_{-T}^T x(t)^2 dt = \int_0^\infty PSD(f) df. \quad (1.23)$$

$PSD(f)$ describes the single-sided power spectral density function of $x(t)$. In a power spectral density (PSD) plot is it difficult to decide if a small peak at a higher frequency or a broad bulge at lower frequency has more or less energy. By calculating the cumulative power spectrum (CPS)

$$CPS(f) = \int_0^f PSD(v) dv, \quad (1.24)$$

this problem is solved. f is the frequency. The goal of DEB is to get the final performance of the system. For this, it is necessary to understand the way individual $PSDs$ propagate through the system and are combined at the output. For uncorrelated disturbances, this can be calculated by

$$PSD_{output}(f) = \sum_i H_i(f)^2 PSD_i(f). \quad (1.25)$$

H_i is the transfer function from the disturbance PSD_i to the output. In Figure 1.13 an example of a block diagram of a system can be seen for the DEB analysis with the different disturbances PSD . To determine the standard deviation of the final error, the root of the total CPS value must be taken [52].

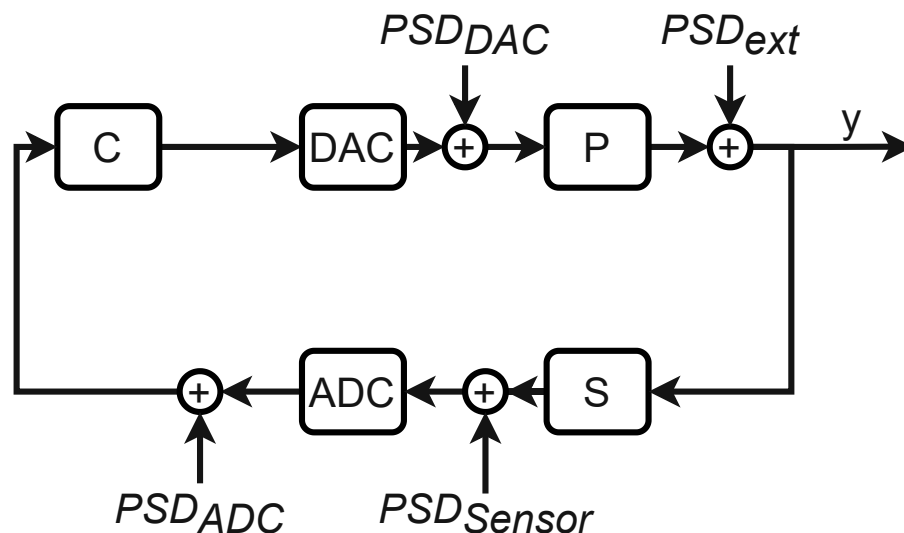


Figure 1.13: Block diagram of a system for DEB analysis

For a non-linear system, an extra step is necessary to calculate the DEB. DEB assumes that the system is linear. The non-linear signal-transformations must therefore be linearized. An example is given in [53], where a performance estimation for a direct-drive permanent magnet synchronous motor is analyzed by DEB. The transfer function and noise function are transformed into the same coordination system. Due to the linearization, the transformation depends on the operating point of the system, therefore DEB is calculated for the zero velocity case and for the constant velocity case.

1.1.4 Input Shaping

Input shaping is a method in which the shape of the input signal is changed in a way that reduces the excitation of unwanted system dynamics or counters external disturbance. The shaping always occurs in an interval half of the period of the system resonance frequency $\frac{T_c}{2}$. These changes of the original input signal can be seen as a convolution of impulses [54]. A simple example of this concept can be seen in Figure 1.14. At first the system undergoes an impulse at its inputs, this could come from an external disturbance or system uncertainties during the design of the input signal. The system responds with an oscillation at the resonance frequency. If second impulses, with lower amplitudes, with an interval that is half of the period of the resonance frequency occur, the system again responds with an oscillation at the resonance frequency. The second oscillation has a phase shift of 180° to the first. The two oscillations cancel each other out.

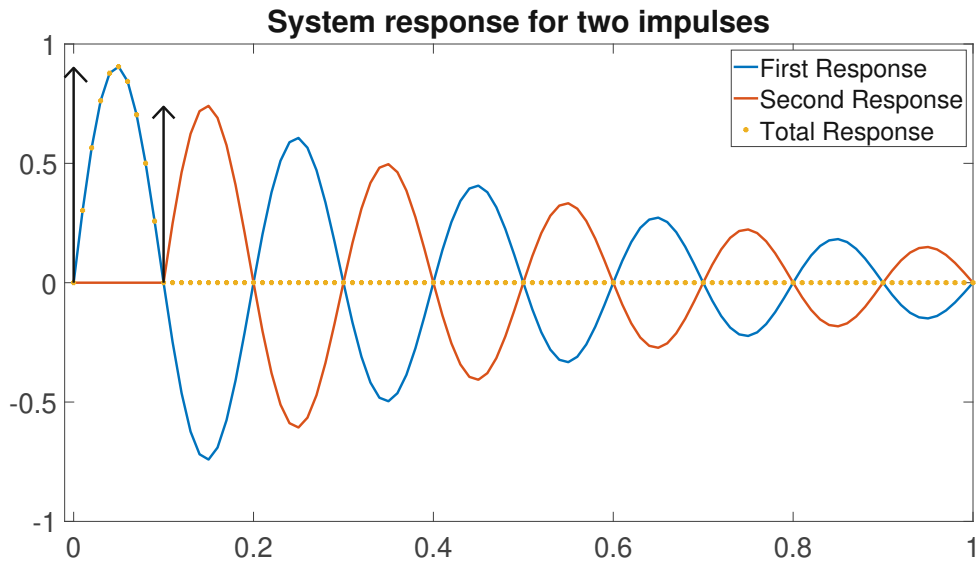


Figure 1.14: Response of system for two input impulses. If the impulses are correctly timed, the two impulses-responses are 180° shifted and cancel each other out.

In general, input shaping can be seen as a convolution of the desired input signal with an impulse sequence [55]. The new input signal is not limited to adding impulses to the signal. Through the convolution sharp changes are added to the new input signal. In [56] the triangular trajectory was cut at the top and so two new sharp changes with in a distance of $\frac{T_c}{2}$, were introduced. [Figure 1.15](#).

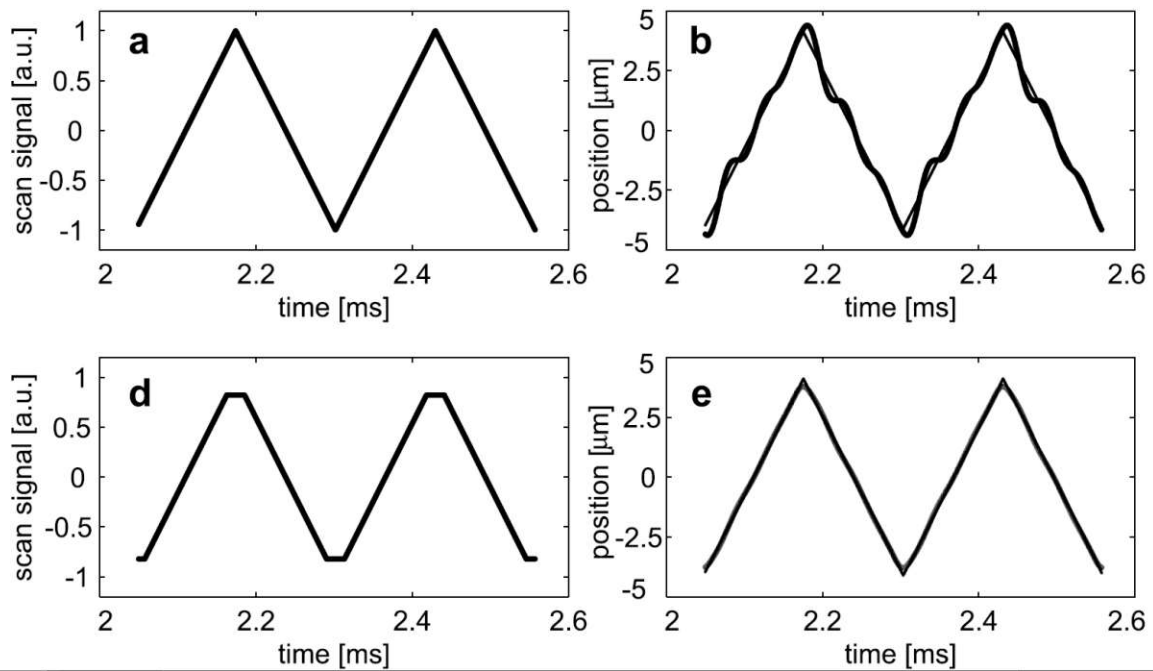


Figure 1.15: Input shaping for triangular signal. (a) show the desired signal before input shaping was used. (b) shows the out of the system with the undesired oscillation. (c) show the desired signal after input shaping with the added sharp changes. (d) shows the new output where the undesired oscillation was reduced. [56]

1.2 Problem Formulation and Research Goal

The electrostatic force, coming from the actuation signal, can only pull the comb drives together, which means that for scanning trajectory like a sawtooth, it is necessary to switch the input when going from negative angle value to positive or the other way around. However, during the input switching, oscillations around the resonance frequency are excited. This effect can be seen in [Figure 1.16](#). In the example, a sawtooth signal is used as the desired trajectory.

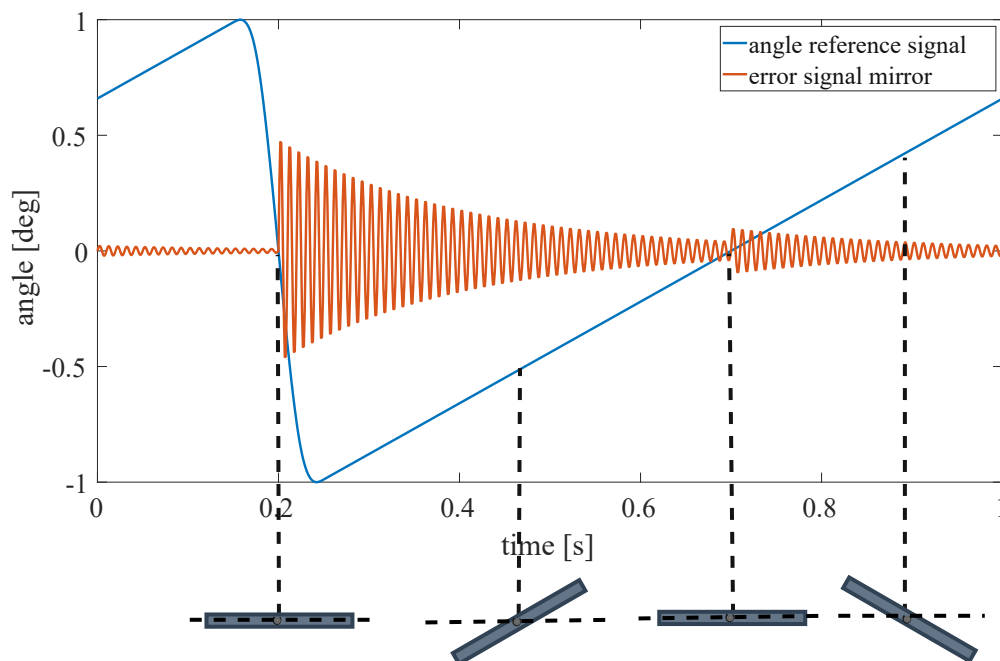


Figure 1.16: Example for oscillation introduced through input switching

Every time the trajectory goes through zero, the input switches and an oscillation is excited. The oscillation then slowly decays due to the low damping of the mirror. This effect is much more visible in the fast turnaround of the saw-tooth signal. In the linear region, the oscillation is only slightly increasing.

1 Introduction

Due to their cheap manufacturing and flexibility with the driving trajectory, quasi-static MEMS mirrors with electrostatic actuation principle, receive much attention by the industry [22]. To make it possible to be used in the varied applications, the mirrors control need a high precision. A method is required to compensate for the introduced oscillation through input switching. To understand the efficiency of the used method, it is also necessary to know the limitation of the test-bench setup. Therefore, two research questions are raised.

What are the limitations of a quasi-static MEMS mirror controlled with optical feedback and where are the bottlenecks in the system?

Can iterative learning control or input shaping reduce the oscillation, introduced through input switching in a quasi-static MEMS mirror?

The idea of a basic feed-forward and feedback controller and a mirror test-setup is discussed in [Chapter 2](#). [Chapter 3](#) deals with the DEB and its results. The two methods to reduce the oscillation and the results are discussed in [Chapter 4](#). Finally, the [Chapter 5](#) conclude the thesis.

Experimental Setup and Control Design for QS MEMS Mirror

This chapter describes the setup of the mirror, parameter identification, the flatness-based feedforward controller, which is used as the basic controller, and the feedback controller.

2.1 Experimental Setup

The measurement setup can be seen in [Figure 2.1](#). The setup is similar to the one described in [\[57\]](#). The input signal for the mirror is provided from the DAC of a dSpace MicroLabBox, which goes through square root(sqrt) circuit. The sqrt-circuit calculates the square root from [Equation 2.11](#). After the sqrt-circuit, the signal goes through a high voltage gain and then to the mirror input. The mirror itself is placed on a six degree of freedom (DOF) stage to adjust the mirror plane to the position sensitive device (PSD) plane. Together with a laser, which is aimed at the mirror, and the PSD the tilted angle of the mirror can be measured. The tilt angle is obtained by

$$\theta = \arctan\left(\frac{u_{diff}}{u_{sum}} \frac{l_{PSD}}{2d}\right). \quad (2.1)$$

where u_{diff} is the difference voltage of two PSD output voltages and u_{sum} is the added PSD voltage. l_{PSD} is the length of the PSD and d the distance between the PSD and the mirror. The PSD is placed on a 1 DOF stage to calibrate the distance d . The picture of the setup can be seen in [Figure 2.2](#).

2.1.1 PSD-Mirror Distance Calibration

To extract the mirror tilt angle it is necessary to know the distance d between the mirror and PSD. The distance is calculated using a similar approach as in [\[57\]](#), but adjusted for QS MEMS mirrors. The PSD is going to be set to zero position. Then

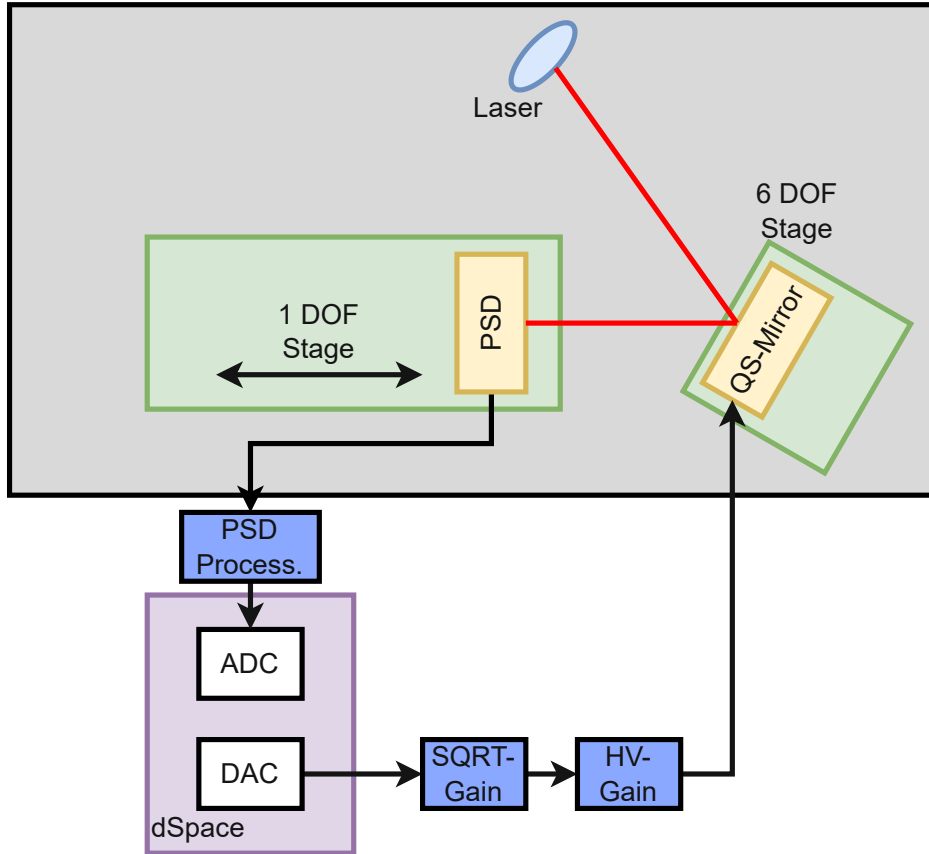


Figure 2.1: Block diagram of the Mirror setup. The mirror reflects a laser beam to a PSD, which is then used to measure the tilting angle of the mirror. The mirror signal is generated through a DAC from a dSpace system, which then goes through a square root circuit and a high voltage gain.

an input voltage signal from -60 V to 60 V with a fixed step size is applied. For every step a short pause is set to let the mirror get to steady state before the position of the laser beam on the PSD is saved. When the signal is completed, the PSD is moved a certain step d_{step} and the process is repeated. In Figure 2.4 the process is displayed for a fixed angle. The blue dots are measured positions on the PSD.

The measured points with the same input voltage are then linearly interpolated. The distance of the mirror is then extrapolated by the point where every line crosses each other with the least square method because of measurement uncertainties the lines are not going to cross each other at the same point. The results of the interpolated lines for every measured point can be seen in Figure 2.5. The red dot indicates the position of the mirror to the starting point of the PSD.

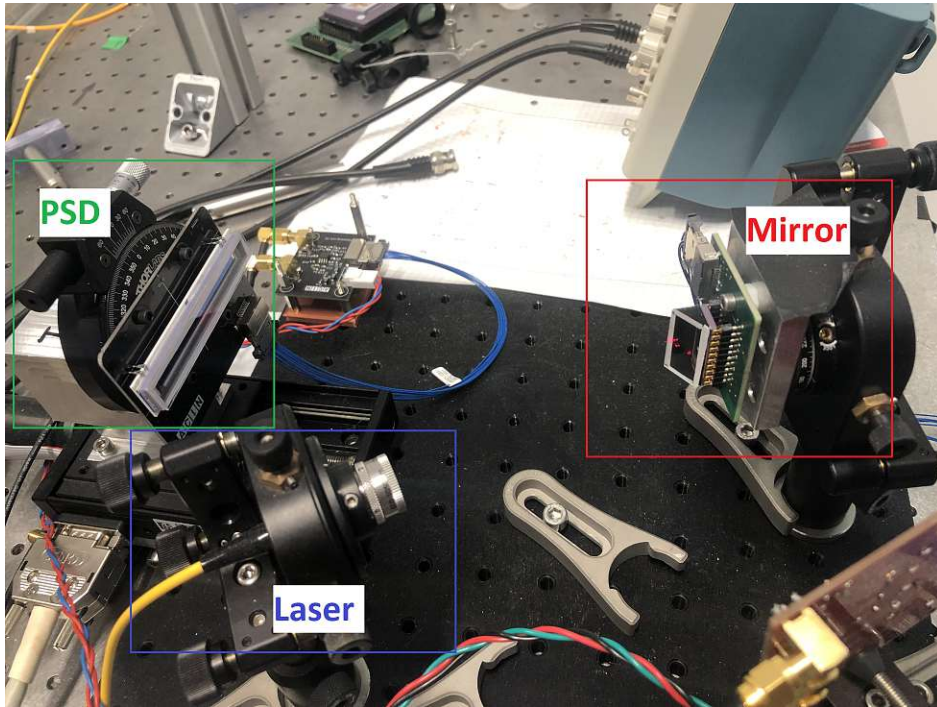


Figure 2.2: Photo of the real setup.

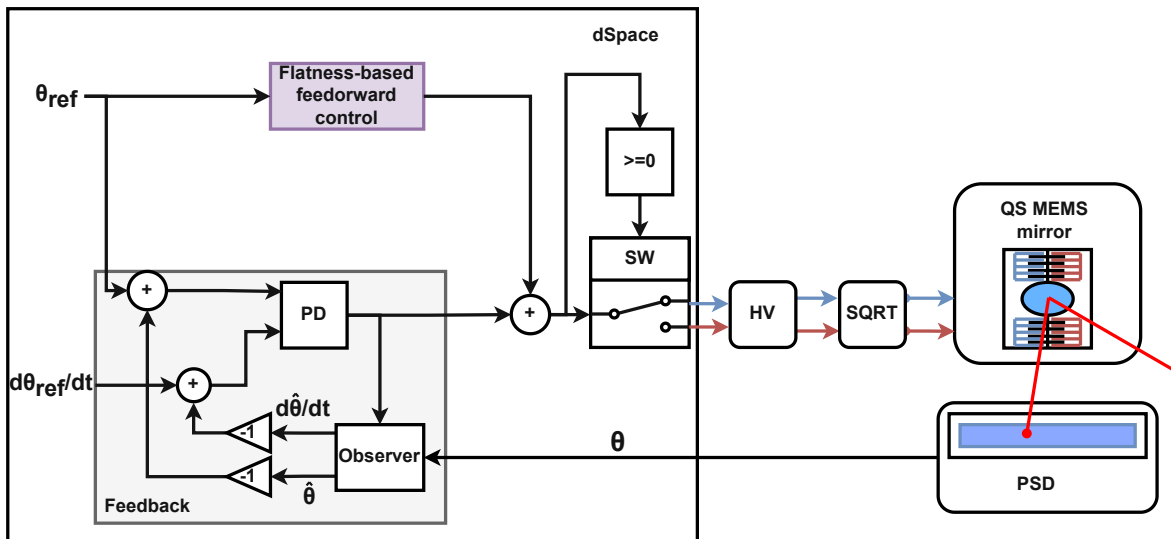


Figure 2.3: Block diagram of the setup with ILC together

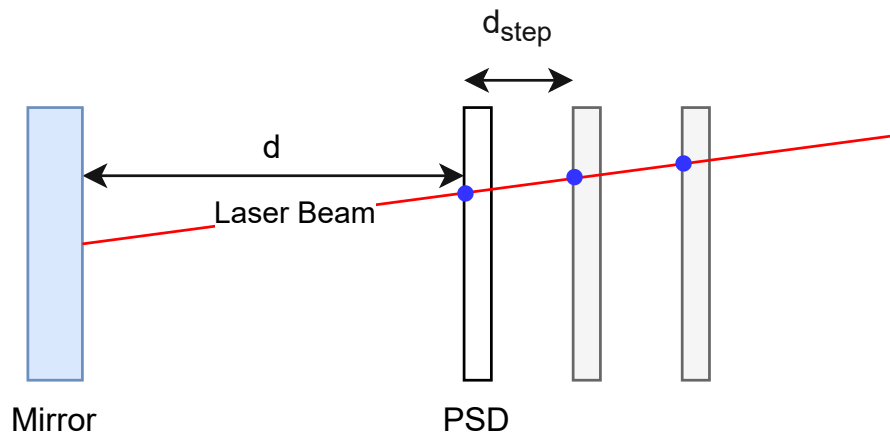


Figure 2.4: Calibration process of the PSD Setup. The individual lines calculated by extrapolated ever point on the PSD with the same input voltage. The Point where all line crossed each other is the position of the mirror.

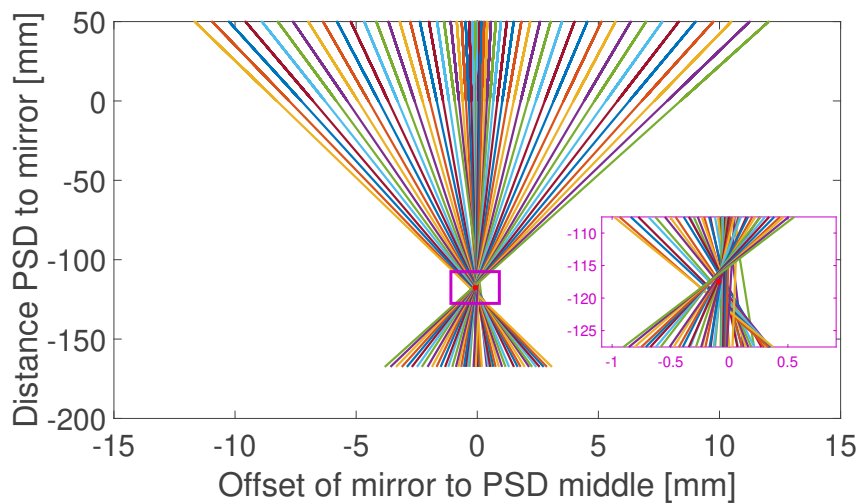


Figure 2.5: Calibration process of the test bench. The individual lines calculated by interpolated ever point on the PSD with the same input voltage. The Point where all line crossed each other is the position of the mirror, which is indicated with a red dot.

2.2 Parameter Identification

Manufacturing tolerances make it necessary to identify certain mirror parameters. This section describes the identification of the spring constant, damping coefficient, and the capacitance derivative curve, which is described in more detail in [4]. The torque inertia value can be taken from the manufacturer's information due to the low production tolerance.

2.2.1 Identification of Spring Constant and Damping Coefficient

The impulse response of a mass spring damper system with a constant damping coefficient decays exponentially with a cosine oscillation, which can be described as

$$\theta_T = \hat{\theta}_0 e^{-\delta t} \cos\left(\sqrt{1 - d_0^2} \omega_0 t\right), \quad (2.2)$$

where $\hat{\theta}_0$ is the starting deflection angle, δ the decay constant and d_0 the Lehr's damping with the connection

$$\delta = d_0 \omega_0 = \frac{b}{2J}. \quad (2.3)$$

To identify the spring constant and damping coefficient, an impulse with the duration of $1/f_0$, with f_0 as eigenfrequency of the mirror and an amplitude of 25 V is applied to one of the mirror inputs. The decay curve is measured, and the Equation 2.2 is fit to the measurement. In Figure 2.6 the measured decay curve together with the fitted curve can be seen.

2.2.2 Identification of Capacitance Derivative

For the identification of the capacitance derivative the static voltage-deflection-angle curve is used together with mirror equation Equation 1.4, where the dynamic parts are set to zero $\dot{\theta} = 0$ and $\ddot{\theta} = 0$ and

$$C'_1(\theta) = 2 \frac{\tau(\theta)}{u_1^2} \quad \text{for } \theta > 0^\circ, \quad (2.4a)$$

$$C'_2(\theta) = 2 \frac{\tau(\theta)}{u_2^2} \quad \text{for } \theta < 0^\circ. \quad (2.4b)$$

The static voltage-deflection-angle curve is measured by applying a sinus voltage with a frequency much smaller than the eigenfrequency $f_0/1000$ to one of the mirror inputs, depending on the angle. For small input voltages, the values u_1, u_2 the Equation 2.5 diverge, because of measurement uncertainties. For a continuous curve, a polynomial is going to be fitted on the calculated capacitance derivative curve. For identifying C'_1 for $\theta < 0$ and C'_2 for $\theta > 0$ it is necessary to apply a voltage to both inputs. The

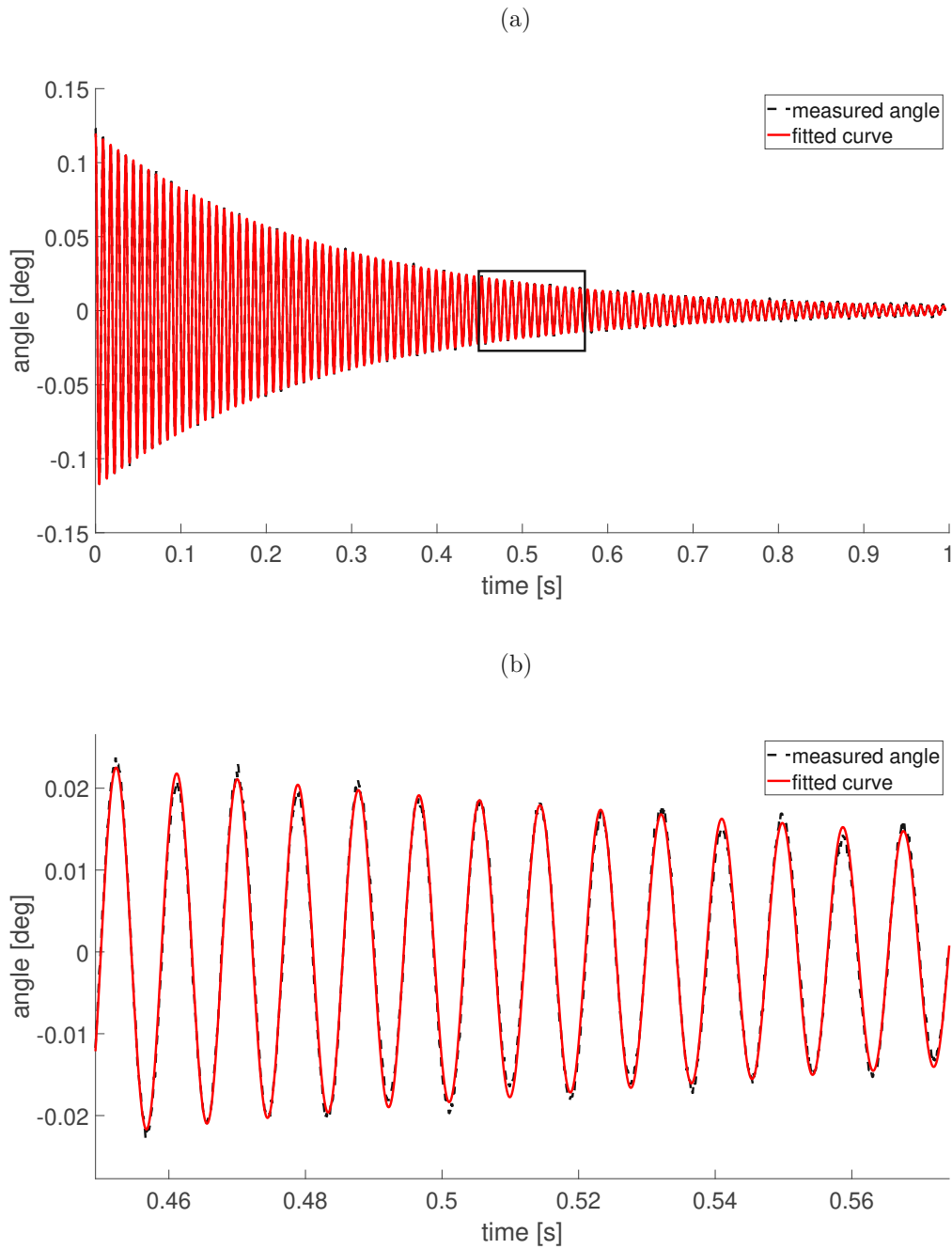


Figure 2.6: Decay curve of mirror after voltage impulse (a). (b) shows the zoomed in part of the decay curve.

capacitance derivative can be calculated with

$$C'_1(\theta) = 2\frac{\tau(\theta)}{u_1^2} - C'_2(\theta)\frac{1}{k_u^2} \quad \text{for } \theta < 0^\circ, \quad (2.5a)$$

$$C'_2(\theta) = 2\frac{\tau(\theta)}{u_2^2} - C'_2(\theta)\frac{1}{k_u^2} \quad \text{for } \theta > 0^\circ, \quad (2.5b)$$

where k_u is the voltage ration

$$k_u = \begin{cases} \frac{u_1}{u_2} & \text{for } \theta < 0, \\ \frac{u_2}{u_1} & \text{for } \theta > 0, \end{cases} \quad (2.6)$$

with $k_u = 0.9$. The calculated capacitance derivative curve, together with the fitted curve, can be seen in Figure 2.7. The fitted curve give a good approximation of the measured. Only around the 0° a different between the fitted curve differ from the measured. This difference could lead to error in the input signal coming from the flatness based feedforward-controller around the 0° . This could be the reason for the oscillation introduced through the input switching operation.

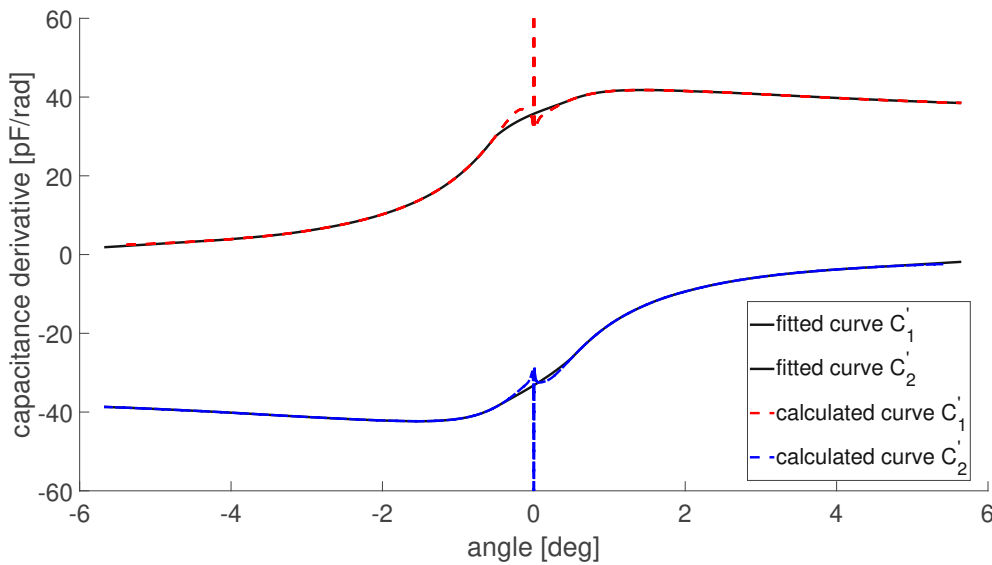


Figure 2.7: Capacitance derivative curve

2.3 Flatness-Based Feed-Forward Controller

As a Basic controller a flatness-based feedforward controller [10] is used for the mirror setup.

A system is differentially flat when the input v and the state vector \mathbf{x} can be written as a function of the output and its derivatives. To show that the mirror system is flat, Equation 1.4 is going to be written in the state-space representation with the state $\mathbf{x} = (x_1, x_2) = (\theta, \dot{\theta})$,

$$\dot{x}_1 = x_2, \quad (2.7a)$$

$$\dot{x}_2 = \frac{b}{J}x_2 - \frac{k}{J}x_1 + \frac{C_1'(\theta)}{2J}u_1^2 + \frac{C_2'(\theta)}{2J}u_2^2, \quad (2.7b)$$

$$y = x_1. \quad (2.7c)$$

The two inputs are to be combined into a new input v

$$v = \frac{C'_1(\theta)}{2J}u_1^2 + \frac{C'_2(\theta)}{2J}u_2^2. \quad (2.8)$$

Together with Equation 2.7 and Equation 2.8 the input can be written as

$$v(y, \dot{y}, \ddot{y}) = \ddot{y} + \frac{b}{J}\dot{y} + \frac{k}{J}y. \quad (2.9)$$

For the flatnessbased feed-forward controller the output in Equation 2.9 is just replaced with the desired trajectory $(\ddot{\theta}_d, \dot{\theta}_d, \theta_d)$

$$v(y, \dot{\theta}_d, \ddot{\theta}_d) = \ddot{\theta}_d + \frac{b}{J}\dot{\theta}_d + \frac{k}{J}\theta_d. \quad (2.10)$$

Mirror comb drives can only produce a pulling force. Therefore, only one of the two inputs is active at a time. The voltages u_1, u_2 for the two inputs are calculated with the following relation.

$$u_1(v_d, \theta_d) = \begin{cases} \sqrt{\frac{2Jv_d}{C'_1(\theta_d)}} & \text{for } v_d > 0, \\ 0 & \text{for } v_d \leq 0, \end{cases} \quad (2.11a)$$

$$u_2(v_d, \theta_d) = \begin{cases} 0 & \text{for } v_d > 0, \\ \sqrt{\frac{2Jv_d}{C'_2(\theta_d)}} & \text{for } v_d \leq 0, \end{cases} \quad (2.11b)$$

where comb 1 is active for a positive tiled and comb 2 for a negative tiled.

2.4 Feedback Controller

PD feedback controller and observer together with the feed-forward controller are designed based on [9]. The PD controller equation is

$$\Lambda(e, \dot{e}) = Pe + D\dot{e}. \quad (2.12)$$

e is the position error $e = \theta_d - \hat{\theta}$ with θ_d as the desired angle and $\hat{\theta}$ as the calculated angle from the observer and \dot{e} is the velocity error $\dot{e} = \dot{\theta}_d - \dot{\hat{\theta}}$. The parameters P and D are set according to the eigenfrequency $\omega_0 2\pi f$ with the constant $k_\lambda > 0$

$$P = 3\lambda^3, D = 3\lambda, \lambda = k_\lambda \omega_0 \quad (2.13)$$

The velocity signal cannot be directly derived from the angle signal because of the noise in the angle signal. A Luenberger observer is used to get the velocity and position for the feedback controller. The observer is implemented as follows

$$\dot{\hat{\theta}} = \int \ddot{\theta}_d + \Lambda(e, \dot{e}) + l_2(\hat{\theta} - \theta) dt \quad \hat{\theta} = \int \dot{\hat{\theta}} + l_1(\hat{\theta} - \theta) dt. \quad (2.14)$$

2 Experimental Setup and Control Design for QS MEMS Mirror

The observer gain l_1 and l_2 are placed with the Ackermann formula at

$$l_1 = 2\hat{\lambda}, \quad l_2 = \hat{\lambda}^2, \quad \hat{\lambda} = k_{\hat{\lambda}}\omega_0, \quad k_{\hat{\lambda}} > 1. \quad (2.15)$$

Dynamic Error Budgeting for QS MEMS Mirror

This chapter describes the DEB for the QS mirror system. It explains the calculation of the different parts of the system, it discusses the end result, and a way to reduce the main disturbance source.

Figure 3.1 shows the block diagram of the system for DEB analysis. It consists of the sensor, ADC, DAC, PD feedback controller and $G(s)$. For the ADC, DAC and feedback controller the MicroLabBox dSpace system is used. $G(s)$ contain the square root circuit, the high voltage gain, and the mirror system. An important note is that the mirror system of Equation 1.4 is here divided into two parts. The voltage square component V^2 part described that the input voltage is squared in the mirror system. External vibrations are not affected by the input Equation 2.9 and therefore are set after the V^2 part. For the transfer function $G(s)$, it is necessary that the system is linear.

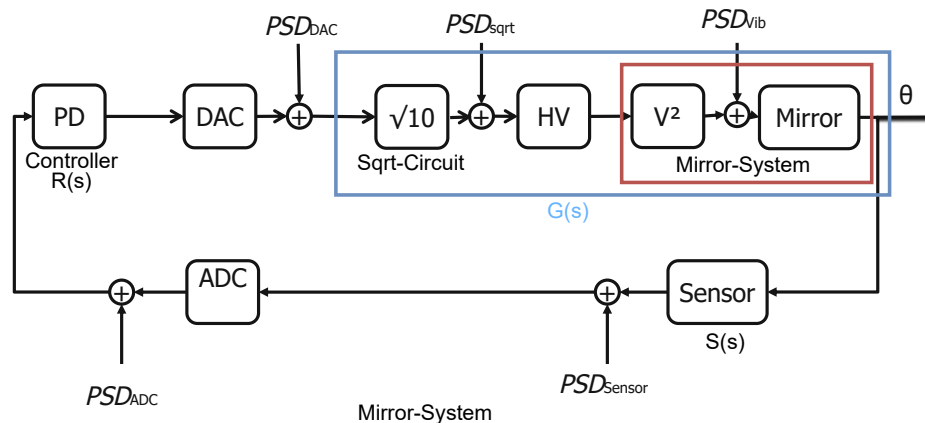


Figure 3.1: Block diagram of the system for DEB analysis

The sqrt-circuit cancels the squaring of the input voltage, so only the angle-dependent capacitance would remain as non-linear part. The mirror sqrt-circuit system could be linearized similar to Equation 1.5, but since DEB is used to approximate the total

output error, another method would be to set the derivative of the capacitance to a constant value, so that the error would maximise, leading to

$$G(s) = \frac{1}{2} \frac{C'_{max} \sqrt{10} H V_{gain}^2}{J s^2 + b s + k}. \quad (3.1)$$

$R(s)$ the transfer function of the controller, a PD controller with values $P = 1.35 \cdot 10^5$ and $D = 635.89$ and $S(s)$ is the transfer function of the sensor, which is set to $S(s) = 1$ since the PSD acts as a low-pass filter with a bandwidth higher than the interesting frequency for the mirror system.

The next sections describes the contribution of each sources of errors.

3.1 ADC / DAC Noise Model

ADC and the DAC both have similar approaches to calculate the *PSD* [58, 59]. In general, the ADC and DAC error source can be split into quantization noise and thermal or electrical noise. Quantization noise can be calculated with

$$\sigma_{quan} = \frac{LSB}{\sqrt{12}}, \quad (3.2)$$

where LSB is the least significant bit, calculated with

$$LSB = \frac{v_r}{2^B}, \quad (3.3)$$

where v_r is the voltage range of the ADC or DAC and B the Bit range. Both the ADC and the DAC have a voltage range of 20 V and a bit range of 16 Bits. This give

$$\sigma_{quan} = \frac{LSB}{\sqrt{12}} = \frac{LSB}{\sqrt{12}} = \frac{20V}{\sqrt{12} \cdot 2^{16}} = 8.8097 \cdot 10^{-05} V_{rms}. \quad (3.4)$$

Electrical noise can be estimated with,

$$\sigma_{el} = \frac{LSB/2/\sqrt{2}}{10^{\frac{SNR}{20}}} \quad (3.5)$$

with SNR as the signal-to-noise ratio. In addition to calculating the *PSD*, it can also be measured. For this, the ADC input of the dSpace system is short-circuited, and the output is measured. For the DAC, the input is set to 0 V and the output is also measured with the help of the ADC input of the dSpace system. The total σ of ADC and DAC can then be calculated with

$$\sigma_{adc/dac} = \sqrt{\sigma_{quan}^2 + \sigma_{el}^2}. \quad (3.6)$$

The value of the ADC is used to calculate the rotation angle of the mirror. The same transformation from voltage to degree has to be done with the *PSD* of the ADC. The idea behind the transformation can be seen in [Figure 3.2](#). To calculate the σ of the ADC for the position value, it is necessary to calculate the way sum signal and the

3 Dynamic Error Budgeting for QS MEMS Mirror

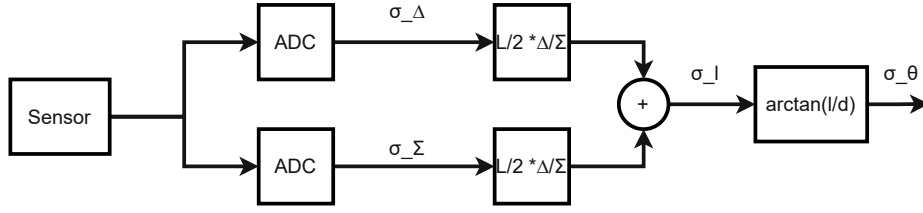


Figure 3.2: Block diagram of the σ_{adc} conversion to angular signal

difference signal of the sensor propagate through the position equation.

$$P(\Delta, \Sigma) = \frac{L \Delta}{2 \Sigma}, \quad (3.7)$$

with Σ as the sum signal and Δ as the difference signal. In the first step, the expected value of $P(\Delta, \Sigma)$ is defined as

$$\mathbb{E}(P(\Delta, \Sigma)) \approx P(\mu_\Delta, \mu_\Sigma), \quad (3.8)$$

where μ_Δ and μ_Σ the operation point is. The variance of $P(\Delta, \Sigma)$ is then calculated with,

$$\begin{aligned} \text{Var}(P(\Delta, \Sigma)) &= \mathbb{E}([P(\Delta, \Sigma) - \mathbb{E}(P(\Delta, \Sigma))]^2) \approx \mathbb{E}([P(\Delta, \Sigma) - P(\mu_\Delta, \mu_\Sigma)]^2) \\ &\approx P_\Delta'^2(\mu_\Delta, \mu_\Sigma) \text{Var}(\Delta) \\ &+ 2P_\Delta'(\mu_\Delta, \mu_\Sigma)P_\Sigma'(\mu_\Delta, \mu_\Sigma) \text{Cov}(\Delta, \Sigma) \\ &+ P_\Sigma'^2(\mu_\Delta, \mu_\Sigma) \text{Var}(\Sigma), \end{aligned} \quad (3.9)$$

where

$$P_\Delta'(\mu_\Delta, \mu_\Sigma) = \left. \frac{\partial P(\Delta, \Sigma)}{\partial \Delta} \right|_{\Delta=\mu_\Delta, \Sigma=\mu_\Sigma} = \frac{L}{2} \frac{1}{\mu_\Sigma} \quad (3.10)$$

and

$$P_\Sigma'(\mu_\Delta, \mu_\Sigma) = \left. \frac{\partial P(\Delta, \Sigma)}{\partial \Sigma} \right|_{\Delta=\mu_\Delta, \Sigma=\mu_\Sigma} = -\frac{L \mu_\Delta}{2 \mu_\Sigma^2}. \quad (3.11)$$

The disturbances of the two ADC are uncorrelated $\text{Cov}(\Delta, \Sigma) = 0$, together with [Equation 3.9](#), [Equation 3.10](#) and [Equation 3.11](#)

$$\sigma_{len} = 1/2 \sqrt{\frac{L^2 \sigma_{adc}^2}{\mu_\Sigma^2} + \frac{L^2 \mu_\Delta^2 \sigma_{adc}^2}{\mu_\Sigma^4}}. \quad (3.12)$$

The angular *PSD* follows a similar step, which in the end leads to

$$\sigma_\theta = \left(\frac{1}{d \left(\frac{l_0^2}{d^2} + 1 \right)} \right)^2 \sigma_{len}. \quad (3.13)$$

Finally, the transfer functions for ADC and DAC are.

$$H_{adc}(s) = -\frac{G(s)R(s)}{1 + G(s)R(s)S(s)} \quad (3.14)$$

$$H_{dac}(s) = \frac{G(s)}{1 + G(s)R(s)S(s)} \quad (3.15)$$

3.2 Square-root-Gain Circuit Noise Model

The disturbance of the Square-root(sqrt) circuit PSD_{sqrt} influences the system after the circuit itself. This means that to get the transfer function, the system has to be linearized again. Similarly to $G(s)$ the derivative of the capacitance is set to a constant value, so only the squared input has to be linearized, hence follows

$$G_{\sqrt{}}(s) = \frac{C'_{max}HV_{gain}^2u_r}{Js^2 + bs + k}, \quad (3.16)$$

with u_r as the operation point voltage.

The PSD_{sqrt} from sqrt-circuit is measured by applying an input voltage between 0 V to 10 V to get different PSD for different operating points and the output is measured with the dSpace ADC.

3.3 Sensor Noise Model

As a sensor, a position sensitive device is used. The PSD of the sensor is obtained by aiming a laser beam at the sensor and measuring the sum and difference voltage signal with the dSpace ADC. The two signals are then used to calculate the angle-time signal. From the angle-time signal the PSD_{sensor} is determined. This process is done for every 5mm on the PSD to get different operation points. The transfer function is as follows

$$H_{sensor}(s) = -\frac{G(s)R(s)}{1 + G(s)R(s)S(s)}. \quad (3.17)$$

3.4 External Vibration Model

One of the main applications for the mirror is going to be used as LIDAR in automotive. Therefore, it is also interesting to see the affects of external vibration of the road on the total error. As an external force, a vibration profile similar to [60] is used, namely Profile D from LV124 [5]. This vibration profile is chosen to simulate a typical vibration load for automotive lidar applications. The spectrum of vibration can be seen in Figure 3.3.

This vibration profile simulates that the mirror is mounted on the front of the car. Also similar to [60] the acceleration is assumed to be normal to the surface of the mirror plate. Since the vibration profile describes an acceleration a , it is necessary to calculate the resulting torque on the mirror. The torque on the mirror is the result of a mismatch of L between the center of rotation and the center of mass m [61], which can be seen in

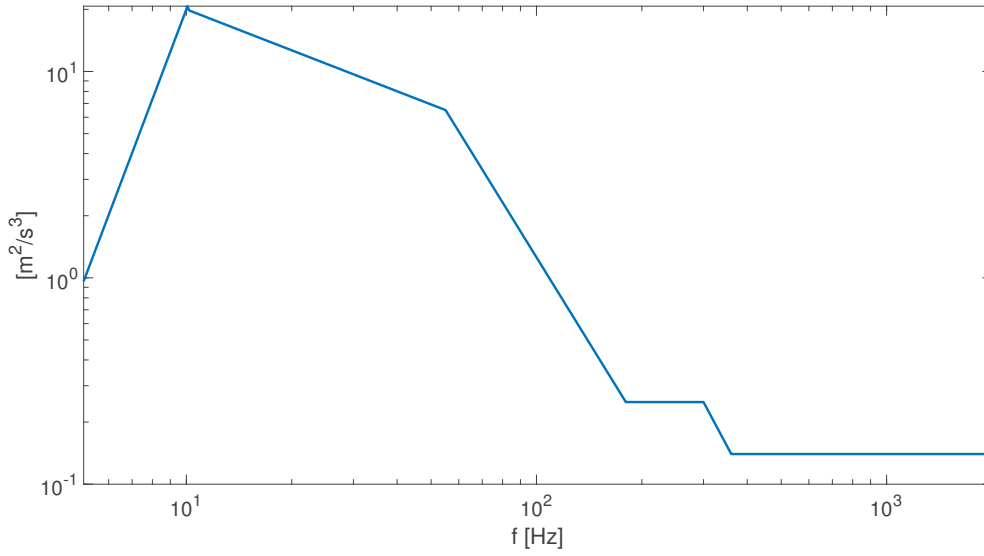


Figure 3.3: Spectrum of the vibration load LV124[5]

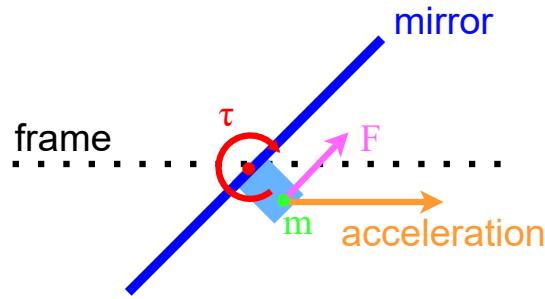


Figure 3.4: Vibration torque model of the mirror

Figure 3.4. The generated torque depends on the direction of the vibration. In this case, a vibration direction parallel to the stator comb is selected, which is the worst-case scenario. The resulting torque is then,

$$\tau = Lm \cdot \cos(\theta) \cdot a = T(s), \quad (3.18)$$

where $a = 2 \cdot 10^{-14}$ is selected. The transfer function of the vibration disturbance is then,

$$H_{vibration}(s) = T(s) \frac{G_m(s)}{1 + G(s)R(s)S(s)}. \quad (3.19)$$

$G_m(s)$ describes the transfer function of the torque to angle, which is just the transfer function of the mirror without the electrical torque,

$$G_m(s) = \frac{1}{Js^2 + bs + k}. \quad (3.20)$$

3.5 Simulation Result of DEB

Together with the calculated *PSDs* and the transfer functions for the various components of the system, the *PSDs* for the individual part of the output of the system, and with Equation 1.25 the total *PSD* can be calculated, which can be seen in Figure 3.5. The calculations are done for the operation point at 0° and 4° to show that the operation point of the mirror does not really change the outcome. In the *PSD* it is already visible that the sensor has a spike at 50 Hz. However, as already mentioned in the *PSD* is it hard to decide how much this spike is contributing to the overall error. Therefore, the CPS also has to be calculated. The result for both operating points can be seen in Figure 3.6. The CPS shows that the 50 Hz spike does not contribute that much to the error. The sensor error slowly rises over the frequency and at the end is the biggest error source. A possibility to reduce the overall error in the system is to reduce the bandwidth to 1 kHz. The standard deviation for both operation points is 1.3 mdeg for a bandwidth up to 25 kHz.

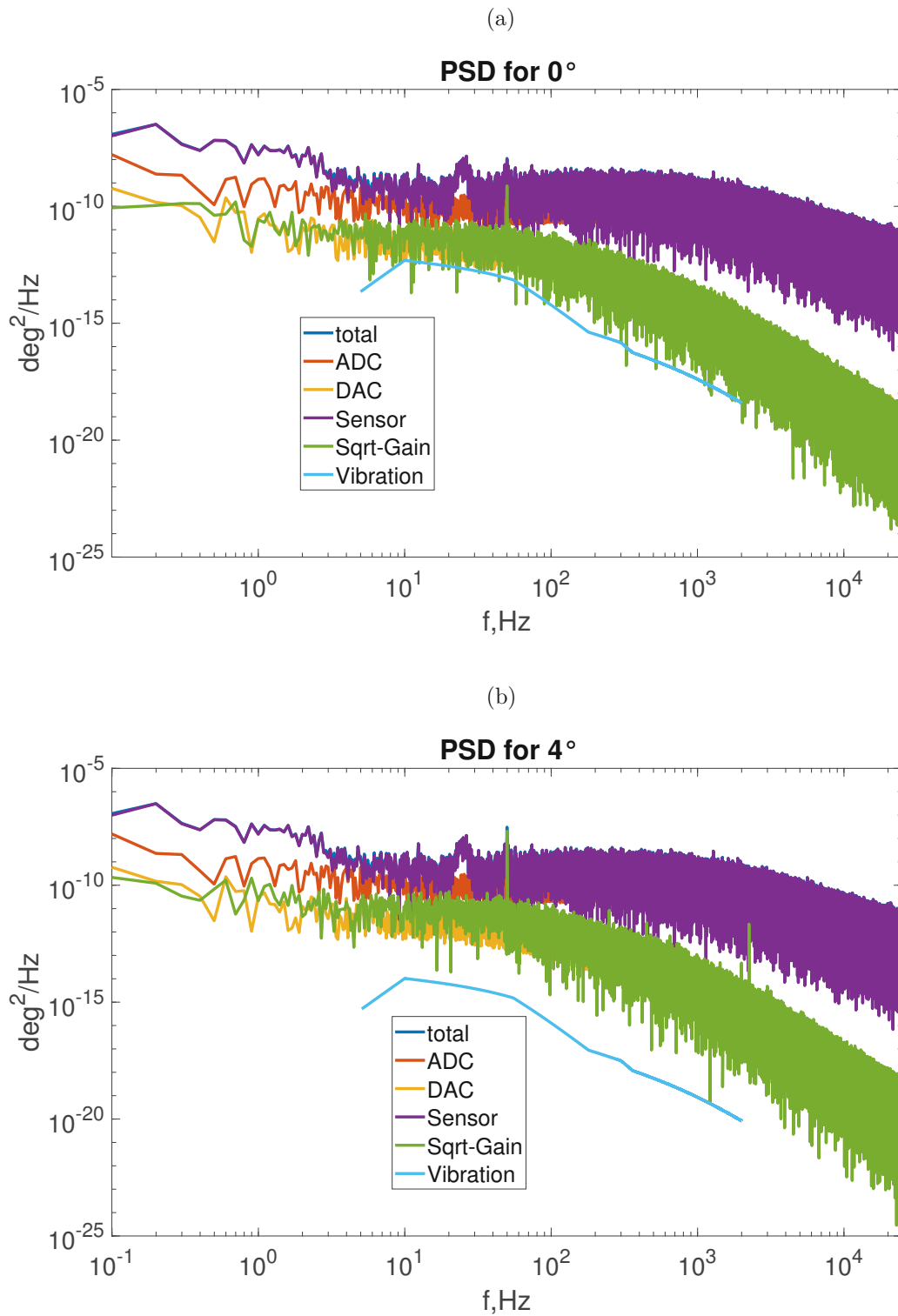


Figure 3.5: PSD of the different disturbance sources at the output (a) shows the *PSDs* for 0° operation point. (b) shows the *PSDs* for 4° operation point

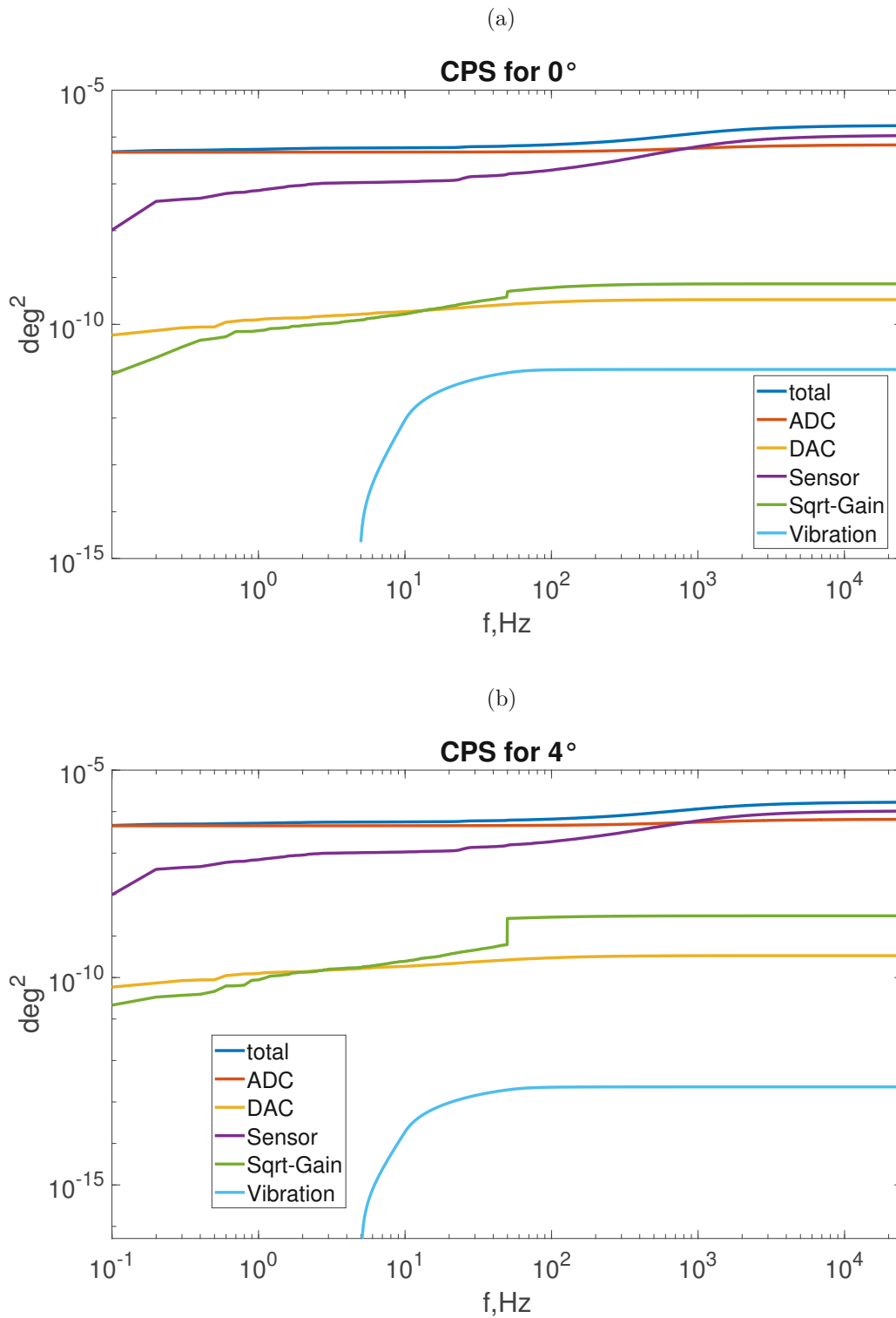


Figure 3.6: CPS of the different disturbance sources at the output. A spike at 50 Hz is visible. (a) shows the CPS for 0° operation point. (b) shows the CPS for 4° operation point

Iterative Learning Control for QS MEMS Mirror

In this chapter the design of frequency-domain iterative learning control (ILC) is explained and the result for the ILC used in the setup is discussed.

4.1 Frequency-domain Analysis of the Oscillation Induced by Switching

For designing a better method to reduce the oscillation, it is necessary to have a better understanding of the error, which is excited through the input switching. Therefore, an FFT is going to be used for the error signal. As desired signal, a sawtooth with different frequency and amplitude settings is used and 10 periods are measured and then transformed to have higher resolution. The result of the FFT can be seen in [Figure 4.1](#) and [Figure 4.2](#).

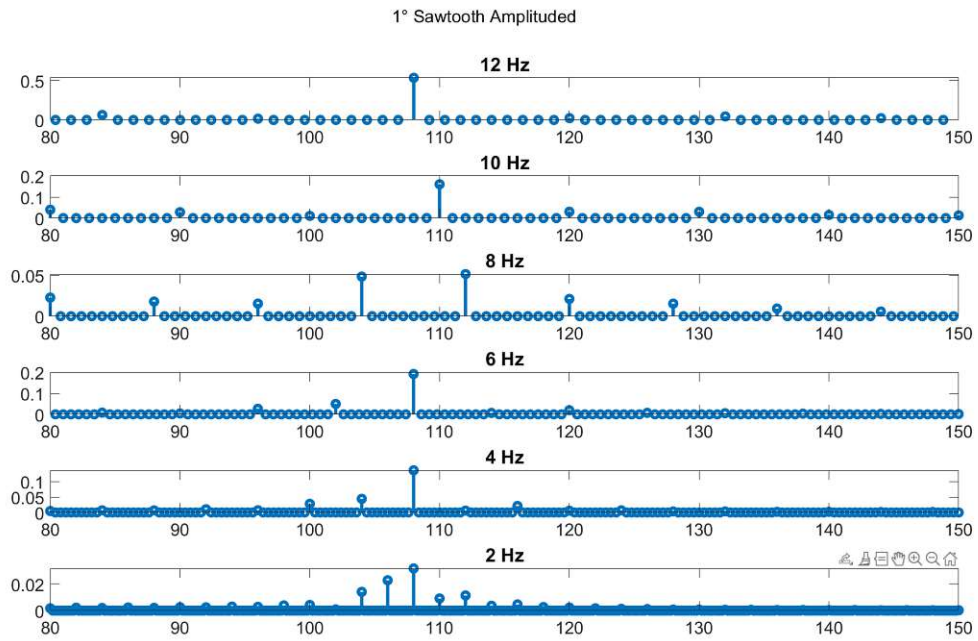
From [subsubsection 1.1.1](#) it can already be expected that the frequency of the excited oscillation is between 105 Hz and 120 Hz. For the sawtooth signal with the amplitudes 1° and 2° the highest peak is around 108 Hz to 112 Hz. For the amplitudes 3° and 4° the error shifts to higher frequencies with up to 115 Hz. However, at the higher sawtooth frequencies the peak is about the same value. In general, the frequency components of the oscillation of the error signal are between 102 Hz and 115 Hz. So the bandwidth of the controllers should go up to minimum of 115 Hz.

4.2 ILC with Feed-Forward Control

[Figure 4.3](#) shows the whole ILC setup. The starting input signal u^0 is calculated through the flatness-based feed-forward controller.

4 Iterative Learning Control for QS MEMS Mirror

(a)



(b)

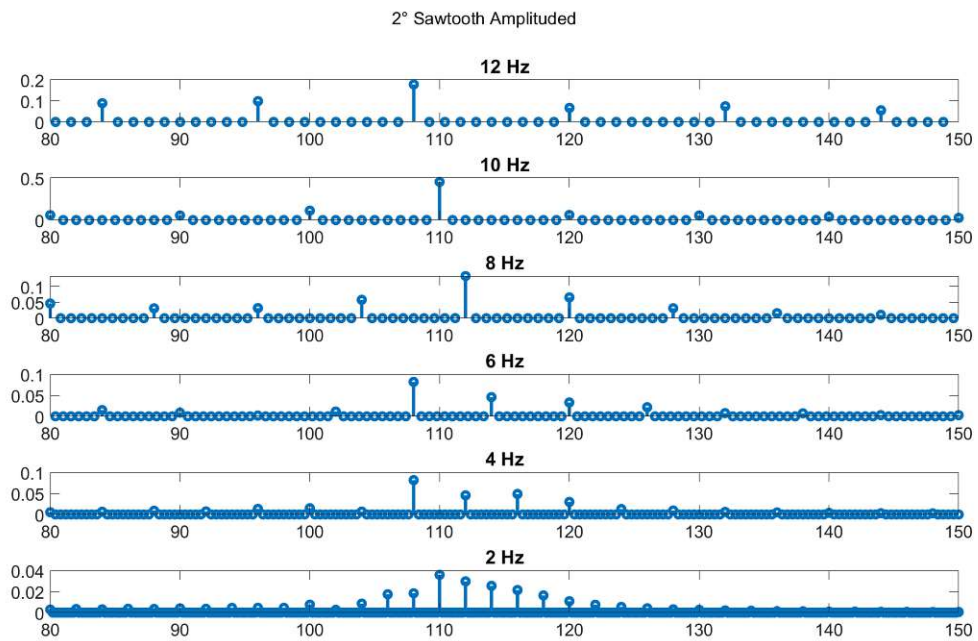
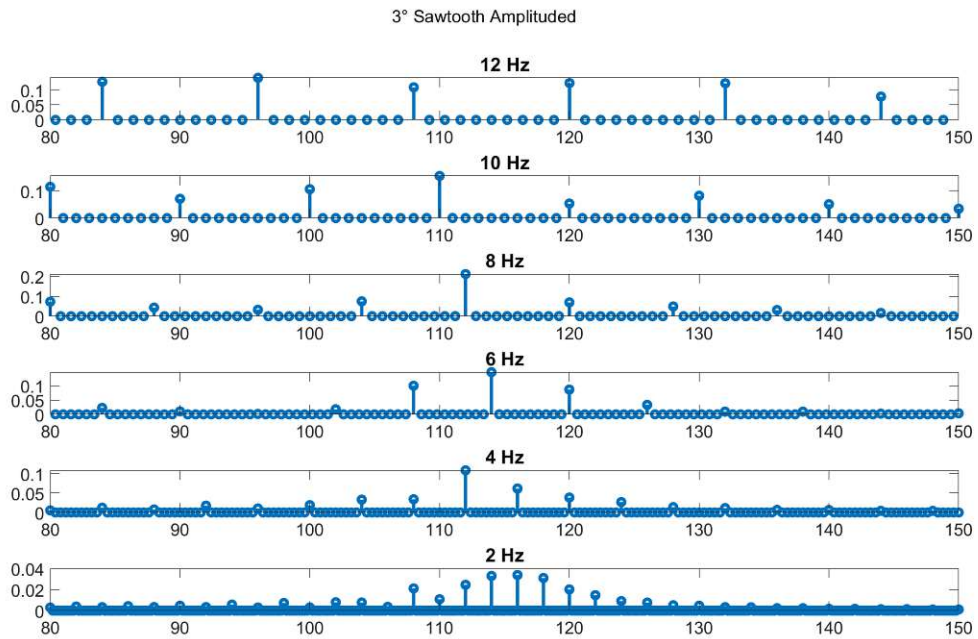


Figure 4.1: FFT of the error signal for different frequencies and different amplitudes.

4 Iterative Learning Control for QS MEMS Mirror

(a)



(b)

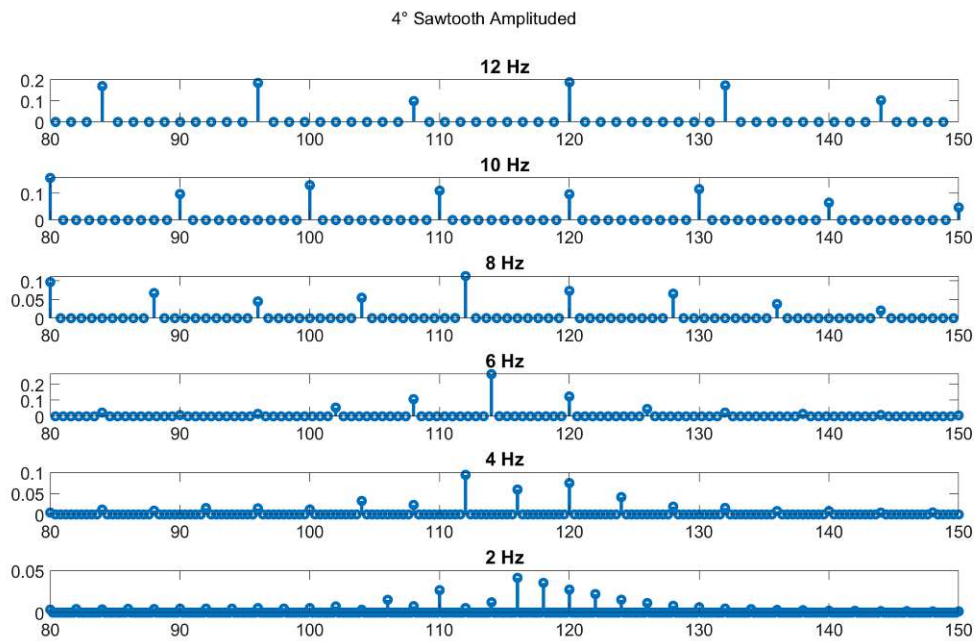


Figure 4.2: FFT of the error signal for different frequencies and different amplitudes.

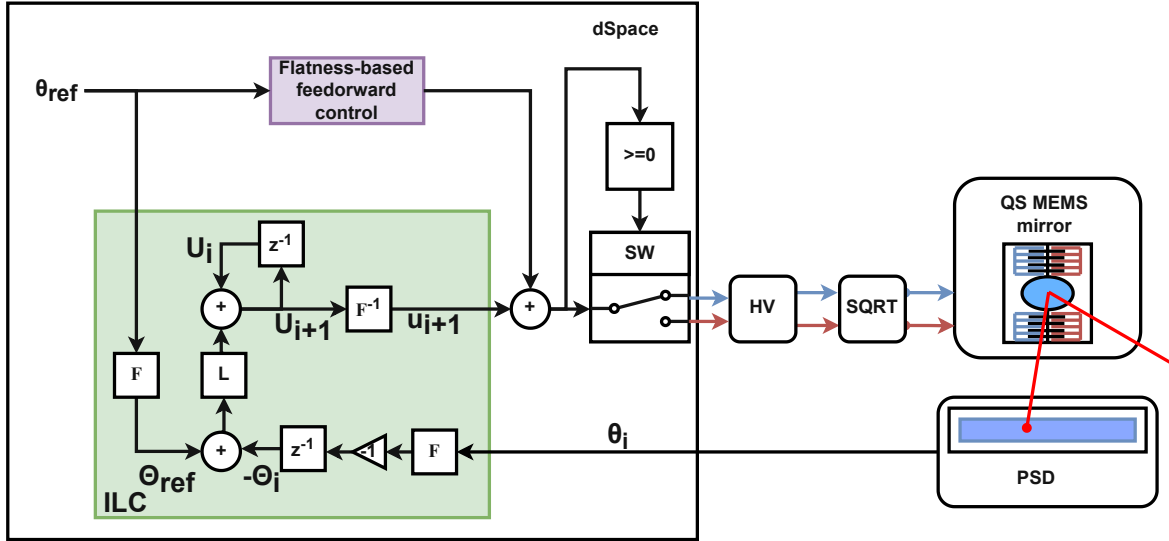


Figure 4.3: Block diagram of the ILC setup

4.2.1 Transfer Function

As learning algorithm, the frequency-domain ILC is used, which use the inverse of the system. For measuring the transfer function, the empirical transfer function estimate (ETF E) is used [62]. As input signal a chirp signal with a trapeziform windowing is used.

$$u(k) = r(k) \sin \left(\omega_{start} k T_a + \frac{\omega_{end} - \omega_{start}}{N T_a} \frac{(k T_a)^2}{2} \right) \quad (4.1)$$

$$r(k) = \hat{u} \text{sat} \left(\frac{10k}{N} \right) \text{sat} \left(\frac{10(N-k)}{N} \right) \quad (4.2)$$

$$\text{sat}(k) = \begin{cases} 1 & \text{for } k \geq 1 \\ k & \text{for } -1 < x < 1 \\ 1 & \text{for } k \leq -1 \end{cases} \quad (4.3)$$

The different angular operation point was set by calculating the constant input signal with the same method as the flatness-based feedforward controller use. The concept can be seen in Figure 4.4. As the amplitude for the chirp signal $\hat{u} = 100$ is used and as the starting and stopping frequency $\omega_{start} = 2\pi \cdot 0.1$ $\omega_{end} = 2\pi \cdot 300$.

By testing different inverse system transfer functions, the best is selected. The transfer function for different operation points can be seen in Figure 4.5

4.2.2 Result with Simple Lowpass Filter

For the learning gain $\rho = 0.1$ is selected and for the cutoff frequency of the learning gain $\omega_B = 2\pi \cdot 200$ is selected to still include all frequencies from the error signal. Figure 4.6 shows a comparison between feedforward only case and the flatness-based feedforward control with ILC. As reference signal a sawtooth signal with an amplitude of 2° and a frequency of 2 Hz is used. The errors before the learning process, 4.6(b),

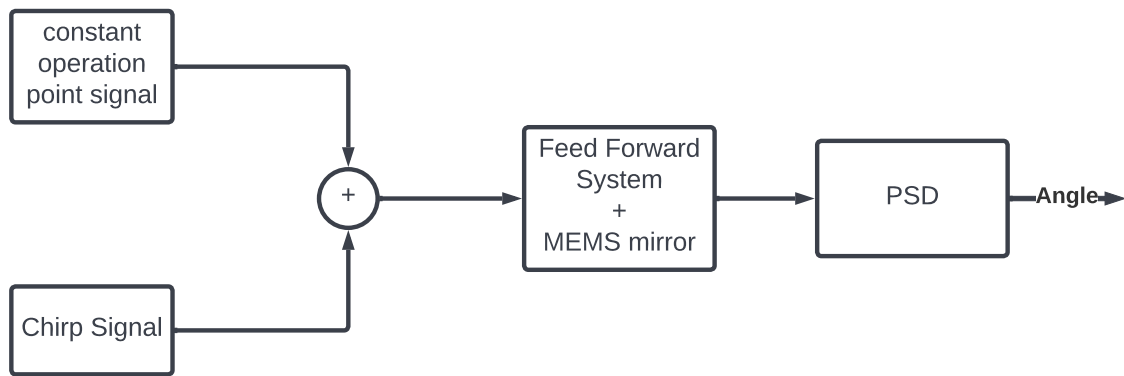


Figure 4.4: Block diagram of the setup for measuring the transfer function of the mirror at the different angular operation points for the ILC input signal.

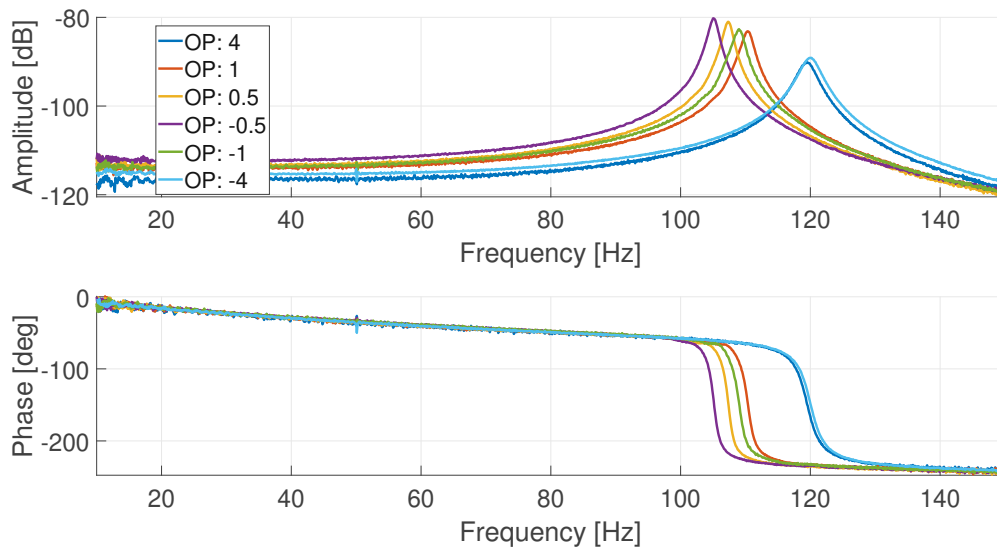


Figure 4.5: Comparison of transfer function for different operation points.

clearly show the excited oscillation after zero crossing. The model error from the flatness-based feedforward controller is visible by the slight offset of the error signal, which becomes much greater at the fast turnaround of the sawtooth signal. The ILC reduces the error that comes from the model uncertainties and the oscillation at the eigenfrequency. The RMS error is reduced from 84.8 millidegrees for the feedforward only case to 1.21 millidegrees with the ILC, which coincides with the calculated RMS error from the DEB in Chapter 3. This is an RMS reduction by a factor of 69.9. Only around the fast turnaround is a small oscillation visible, 4.6(c). For the rest of the signal, the oscillation is completely rejected. The error converges in about 80 iterations. This slow convergence comes from the low learning gain $\rho = 0.1$. The minimum is found at 148 iterations

In Figure 4.8 the RMS error diagram can be seen, showing the lowest RMS error for the feedforward controller with ILC for a variety of sawtooth reference signals ranging

from 1 to 10 Hz and 1° to 4° . Each pixel represents one result for one sawtooth reference signal. For comparison the RMS error diagram if the feedforward only case can be seen in [Figure 4.7](#). In general, the comparison shows that the ILC reduces the RMS error. The variety test shows that the error reduction decreases as the sawtooth parameters increase. In the range around 1 Hz-2 Hz and $1^\circ - 2^\circ$ the oscillation is almost completely rejected. An example of this can be seen in [4.10\(a\)](#). For parameters in the middle range, the RMS error increases by a factor of 10 compared to the low range parameters. The ILC still shows an improvement of the oscillation, but not as good as in the low parameters. At the edge of the parameters, the RMS error again increases by a factor of 10. An example of this can be seen in [4.10\(b\)](#). In this area, the ILC often only improves the model error but does not reduce the oscillation. An example for this can be seen in [4.10\(c\)](#). The input signal after learning can be seen in [Figure 4.11](#). For all cases, the ILC shifts the chance of the input to an early point of time.

The d and c in [Figure 4.9](#) shows at which sawtooth parameters the ILC converges and at which the ILC becomes unstable. A c in the diagram means that the ILC did converge, which was verified by letting the ILC run for 150 iterations and a d that the ILC diverge. The ILC does convergence for the parameters where the algorithm also get a low RMS error. By achieving convergence at the other sawtooth trajectories, an overall performance improvement of the ILC at the whole range could be possible. This convergence could be achieved by changing the Q-filter to a more specified filter.

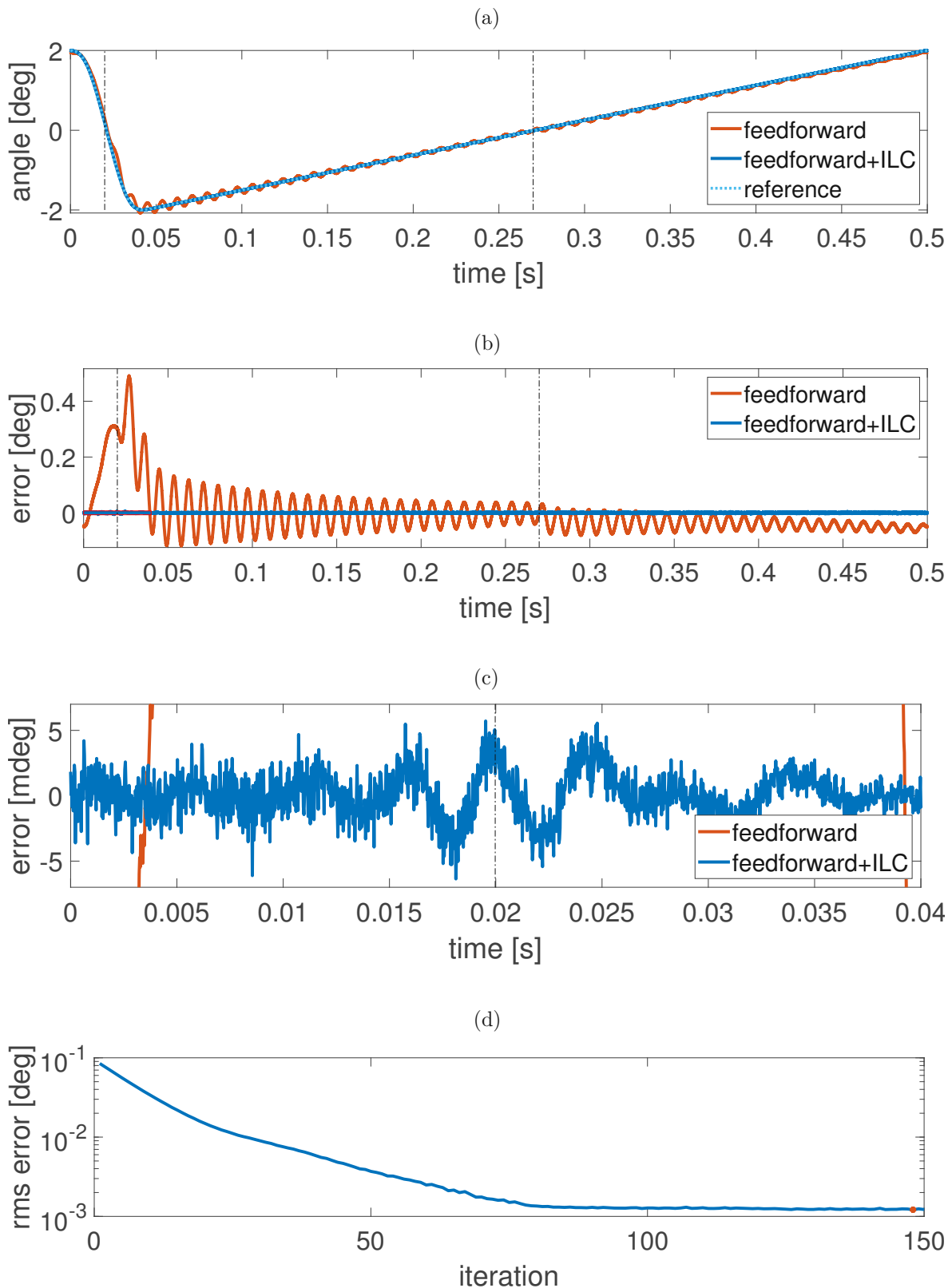


Figure 4.6: Result of the ILC for sawtooth trajectory with an amplitude of 2° and a frequency of 2 Hz. (a) shows the measured angle signal before and after learning process together with the reference signal. In (b) the error between measured angle and reference signal from before learning as well as after learning. (c) is the enhanced error from the read box. The RMS error of the learning iteration can be seen in (d). The learning converge at about 75 iterations

4 Iterative Learning Control for QS MEMS Mirror

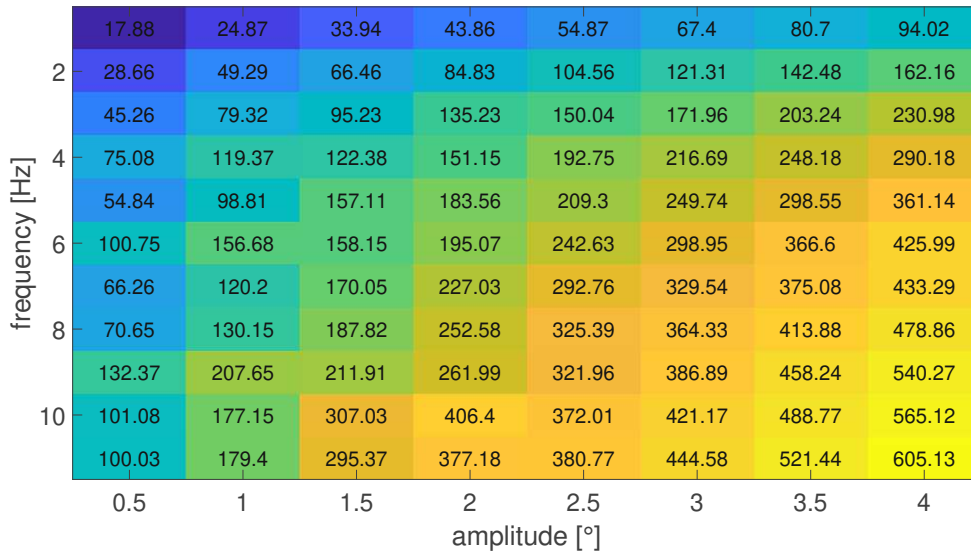


Figure 4.7: RMS error for the feedforward only case.

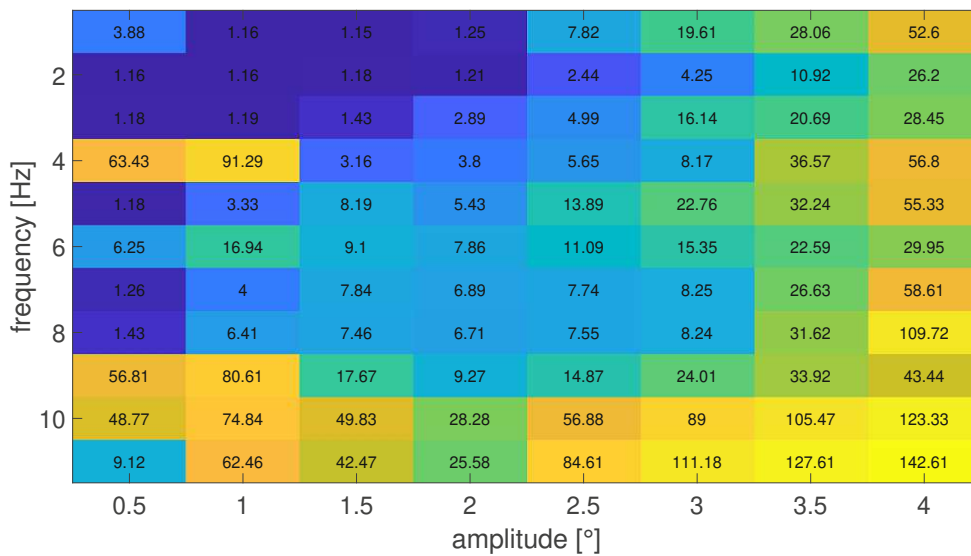


Figure 4.8: RMS error for the feedforward only case.

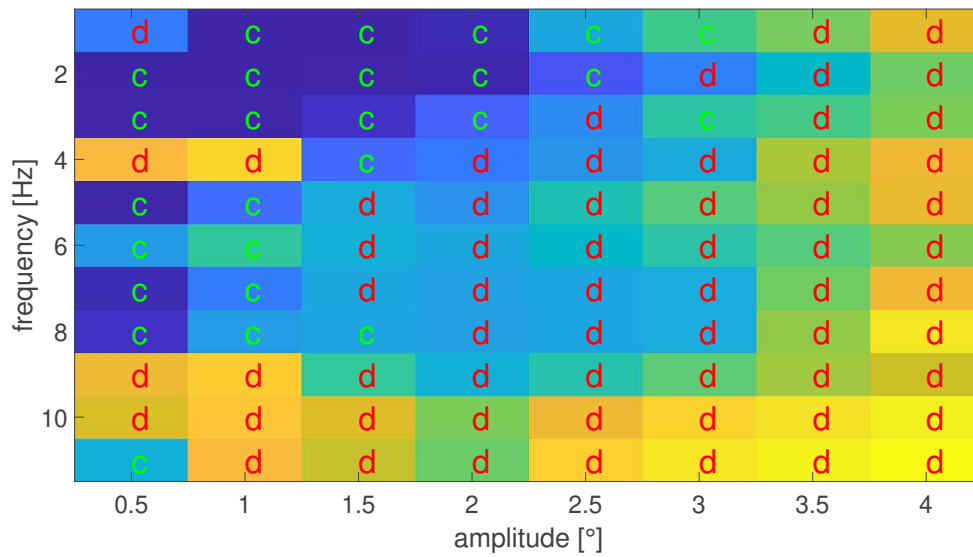


Figure 4.9: RMS error after the learning process for different amplitude and frequency settings. Green c shows that the ILC did converge and red d shows that the ILC diverge

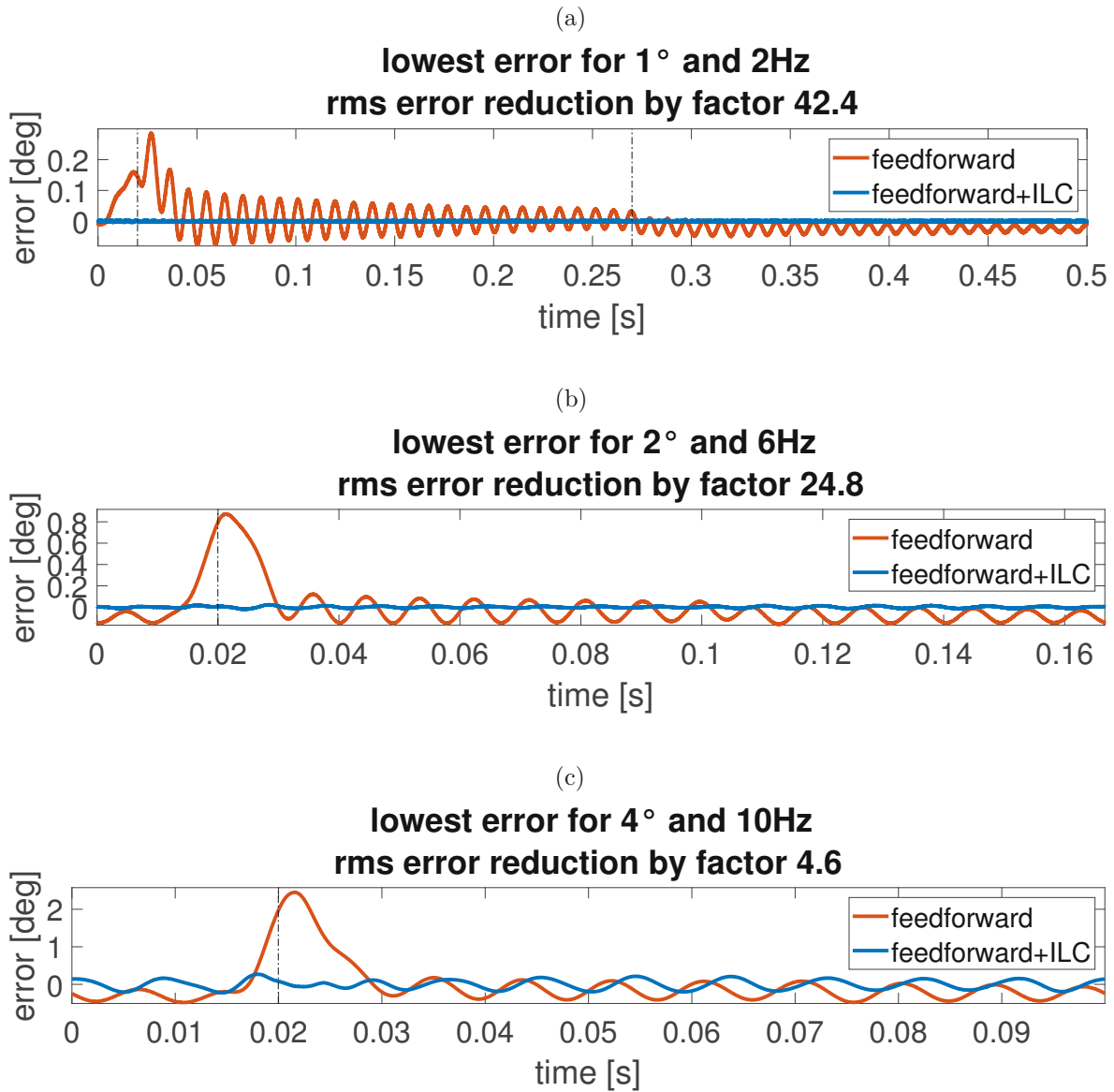


Figure 4.10: 3 different result for the ILC with simple Q-filter. (a) shows an example for one of the best results for the ILC.(b) shows a an example in the middle parameter set range. (c) shows an example in the higher parameter set range.

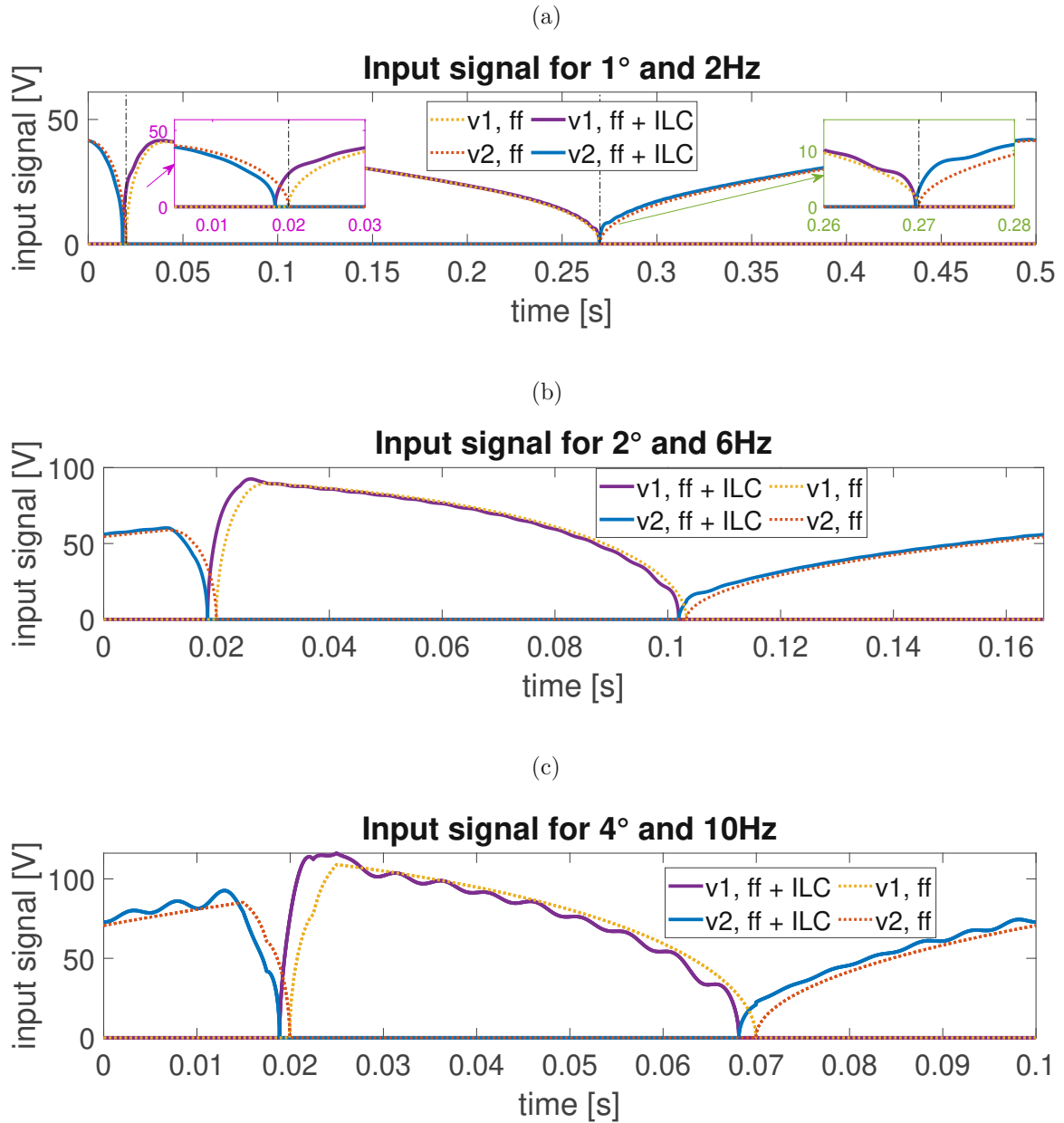


Figure 4.11: 3 different input signal for the ILC with simple Q-filter. (a) shows an example of the input signal for one of the best results for the ILC. (b) shows an example of the input signal in the middle parameter set range. (c) shows an example of the input signal in the higher parameter set range.

4.3 ILC with Time-Variant Q-filter

The result of the previous section shows that the ILC with a simple low-pass Q-filter does not converge for most sawtooth parameters. Performance improvement could be achieved by achieving convergence for all parameters. Through introducing a Q-filter, which is more specific for the problem, the ILC could converge in all areas.

Figure 4.9 shows that for amplitude lower than 2° ILC achieves a good error reduction and converges for lower frequencies. The idea is to use two different low-pass filters. One with a high bandwidth for part of the angle signal, which is between -2° and 2° and one with a lower bandwidth for the other part of the angle signal. A time-variant low-pass filter can be designed to have exactly this characteristic. The two filter characteristic combined in the time-variant Q-filter uses a zero-phase Butterworth filter with an order of 7 as base. The high bandwidth filter has a crossover frequency at 160 Hz. These values are selected, so that the frequency components of the error signal are still included, described in section 4.1. The lower bandwidth filter has its crossover frequency at 100 Hz, so that the resonance frequencies are reduced around 3 dB . A high reduction would guarantee a more stable ILC, but at the cost of efficiency of error reduction.

Figure 4.12 shows the RMS error diagram together with the convergence diagram of the new ILC. With the time-variant Q-filter the ILC does now converge for most of the sawtooth parameters. An example of convergence due to the new Q filter can be seen in Figure 4.13. Only for an amplitude of 0.5° and one frequency at 3° does the ILC become unstable. The efficiency of the ILC with the new Q-filter can be seen in the performance factor diagram Figure 4.14, which shows the value of the performance factor for the different sawtooth trajectories.

$$\text{performance factor} = 20 \log_{10} \left(\frac{\text{RMS error old}}{\text{RMS error new}} \right), \quad (4.4)$$

with *RMS error old* as the lowest resulting RMS error from the ILC with simple lowpass filter and *RMS error new* as the resulting RMS error from the new method. Values above 0 mean that the new ILC method has a lower RMS error. This is only true for some edge value. The error signal for sawtooth 1° and 2 Hz shows an example for a negative performance factor and can be seen in 4.15(a). The new Q-filter decreases the performance of the ILC so much that nearly no error is reduced. In 4.15(b) the error signal for 4° and 1 Hz can be seen. Here the time-variant Q-filter does help with reducing the RMS-error furthermore. By adding a time-variant Q-filter to the ILC the convergence is improved from 29.5% of all cases to 78.4% of all cases, but 87.5% of all cases have a decrease of performance. The reduction of the performance could be the result of a non-optimal Q-filter algorithm. Analysis of the filter algorithm shows that it introduces some small error in the filtered signal. Due to the lack of time while conducting the project, the filter algorithm cannot be improved.

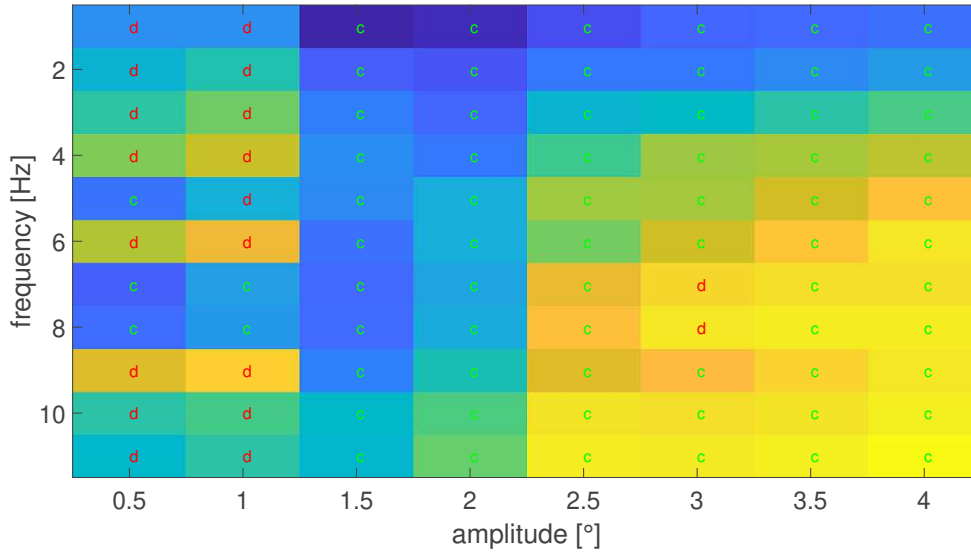


Figure 4.12: RMS error for time variant Q-filter after the learning process for different amplitude and frequency settings. Green one shows that the ILC did converge and red zero shows that the ILC diverge.

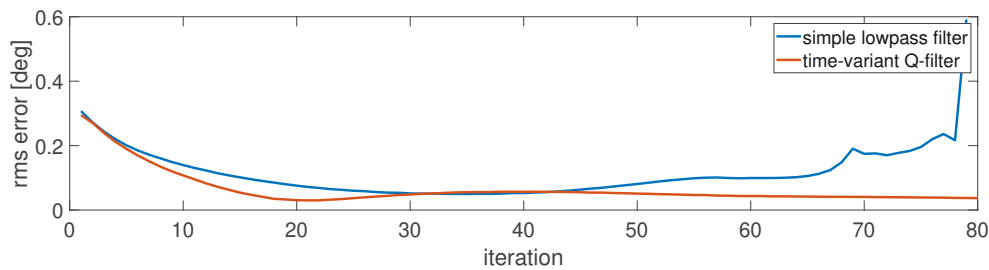


Figure 4.13: Comparison of convergence of ILC with lowpass filter and time-variant Q-filter for a sawtooth with 1.5° and 10 Hz. The RMS error is always taken from the lowest point.

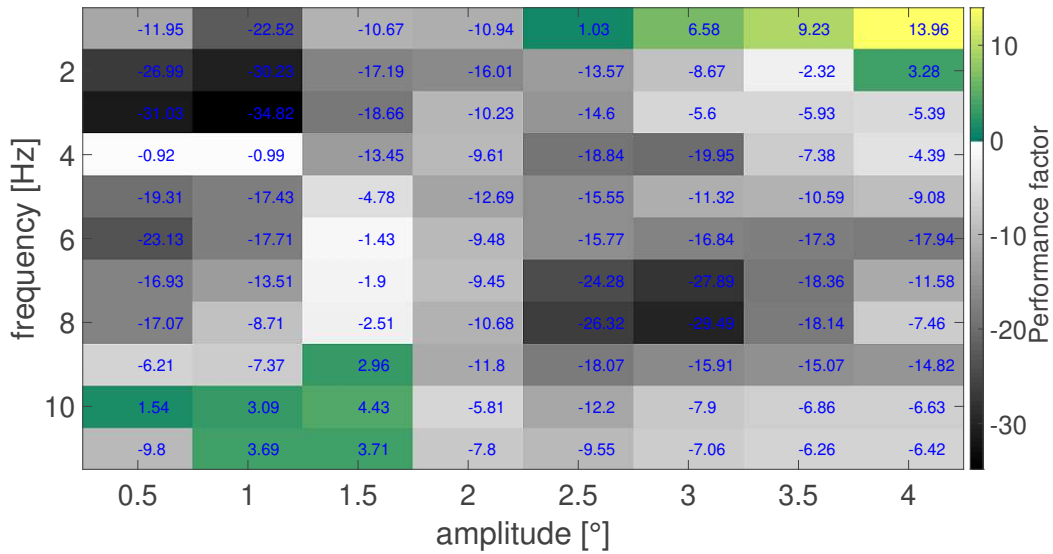


Figure 4.14: Performance factor diagram. Comparison between the RMS error after the learning between ILC with simple low-pass filter and the time variant low-pass filter. The factor where calculated with Equation 4.4. A factor value > 0 means that the time variant low-pass filter has a lower RMS error value, then the simple low-pass filter.

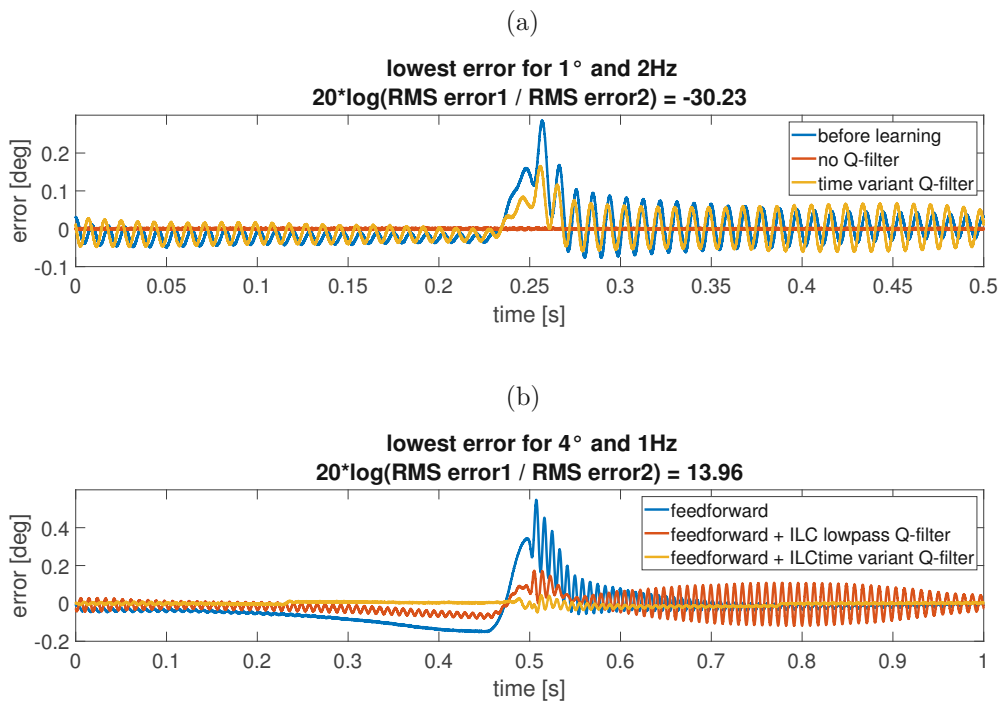


Figure 4.15: Two different results for the time variant Q-filter. (a) shows an example where the new Q-filter reduced the efficiency of the ILC. (b) shows an example where the new Q-filter increased the efficiency of the ILC

4.4 Input Shaping with ILC

Input shaping is implemented by adding impulses shortly after zero crossing. An example of this method can be seen in 4.16(c). The impulse can only reduce the oscillation, which is excited through the switching of the input. The error from the model uncertainties in the flatness-based feedforward controller would remain. In addition to input shaping, a frequency-domain ILC is used. The ILC should only reduce the error from the model uncertainties and not the oscillation, so the learning gain $\rho(j\omega)$ bandwidth is set to a lower value than the switching oscillation,

$$\rho = \begin{cases} 0.5 & \text{for } \omega \leq 2\pi 100 \\ 0 & \text{for } \omega > 2\pi 100 \end{cases} \quad (4.5)$$

The lower bandwidth of the ILC eliminates the problem with convergence of the ILC. The error reduction of the angle signal is done in two steps. First, the ILC reduces the error of the model uncertainties until the RMS error converges. Afterwards, the ILC algorithm is stopped, and the impulses are added to the new input signal.

The efficiency of input shaping is verified with a sawtooth signal with an amplitude of 2° and frequency of 2 Hz as reference signal, 4.16(a). In the error signal, 4.16(b) the oscillation was reduced with the help of the added impulses. The error before the added impulses already includes the ILC, as a result there is no model error visible. Compared with the feedforward control only case, the RMS error was reduced from 84.8 mdeg to 12.1 mdeg. Input shaping is used only as a proof of concept, therefore the impulse parameters, such as position and amplitude, are set manually. The best position of the impulses is most of the time a little bit after zero-crossing. Normally, the best position would be around the distance half of the period of the resonance frequency from the zero crossing. This difference could be because the oscillation, which is excited through the input shaping, is not the same as the oscillation from the input switching, but already a 180° shifted signal.

Figure 4.17 shows the RMS error before implementing the input shaping with ILC and Figure 4.18 shows the RMS error after using input shaping with ILC. Comparing these two figures shows that input shaping with ILC reduces the the RMS error.

Figure 4.19 shows the performance diagram compared to the ILC with simple low-pass filter from subsection 4.2.2. The factor is calculated with Equation 4.4. The comparison shows that the input shaping does not produce a similar or better result as the ILC method. About 80% of all sawtooth trajectory cases have a reduction in performance Figure 4.20 and Figure 4.21 show four performance examples of the ILC combined with the input shaping compared to the ILC with simple low-pass Q-filter. The top left shows an example where the performance of the input shaping is much worse than the performance from the previous ILC. The oscillation error, especially around the fast turnaround, is only reduced by a small part. Top right shows an example where input shaping performance is not as good as ILC from the previous chapter. Bottom left shows an example where input shaping performance is a little bit better than ILC from the previous chapter. However, the reduction of the oscillation error with input shaping is not uniform. The bottom right shows an example, where the input shaping performance is better than the ILC performance from the previous chapter. Here, a

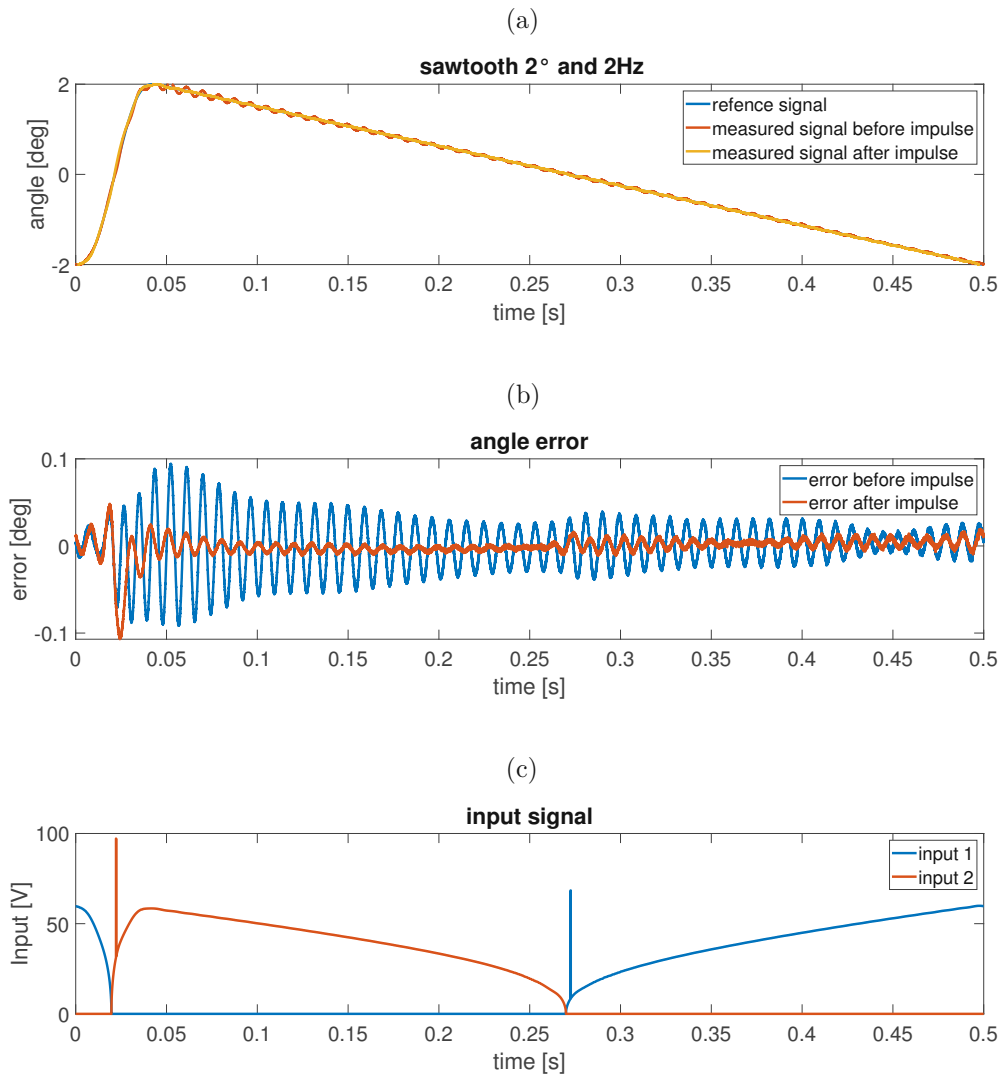


Figure 4.16: Result of the input shaping combined with ILC for sawtooth trajectory with an amplitude of 2° and a frequency of 2 Hz. (a) shows the measured angle signal before and after adding the impulses together with the reference signal. In (b) the error between measured angle and reference signal from before as well as after adding the impulses to the input signal. The input signal can be seen in (c). The two impulses are added slightly after the zero-crossover.

reduction of the oscillation error is clearly visible.

4 Iterative Learning Control for QS MEMS Mirror

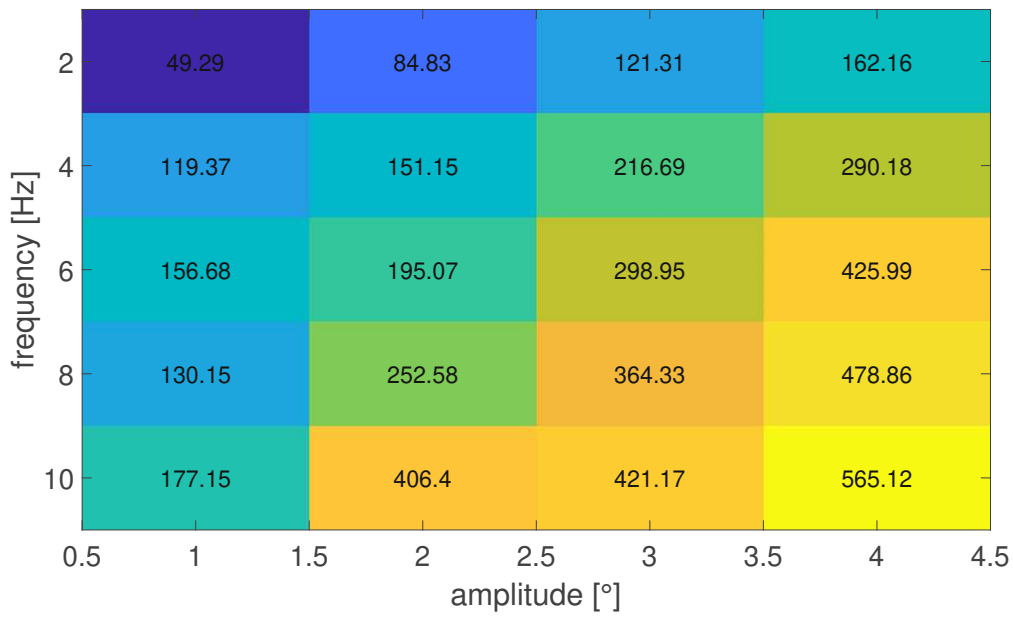


Figure 4.17: RMS error for the feedforward only case.

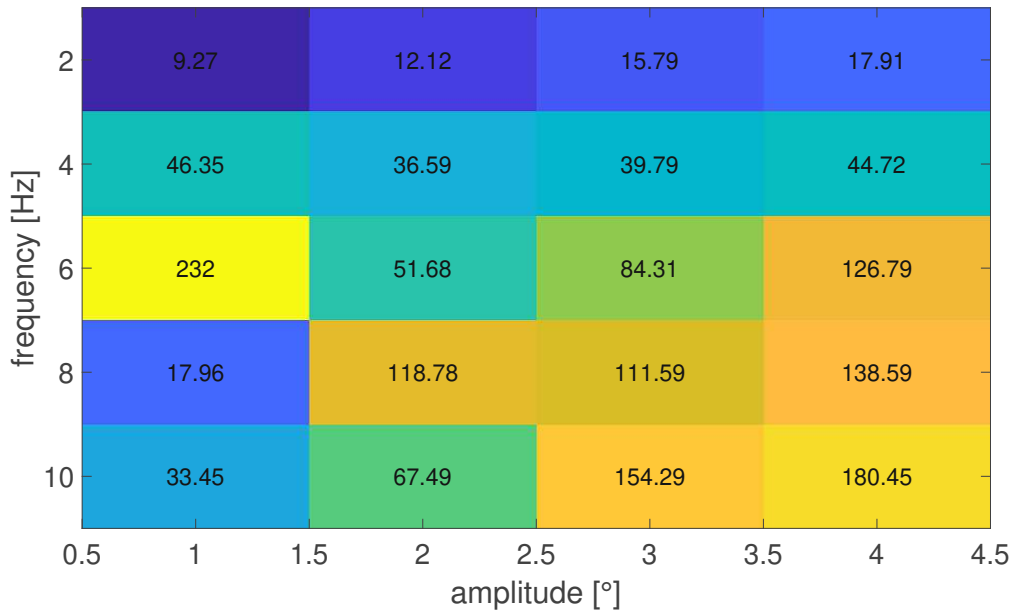


Figure 4.18: RMS error for the feedforward with input shaping and ILC case.

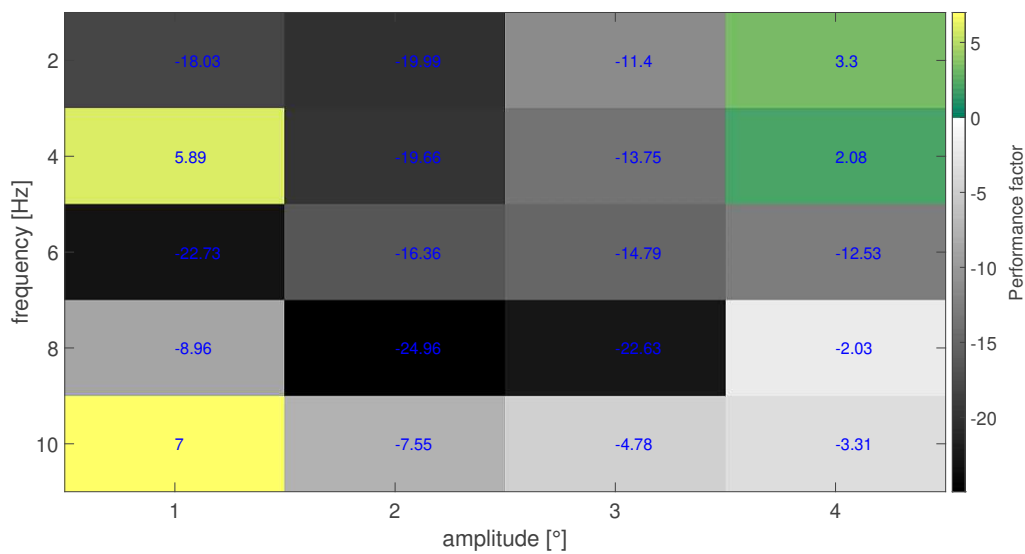


Figure 4.19: Performance-diagram for input shaping. Comparison between the RMS error after the learning between ILC with simple low-pass filter and ILC combined with input shaping. The factor was calculated with Equation 4.4. A factor value > 0 means that the input shaping has a lower RMS error value, then the simple low-pass filter.

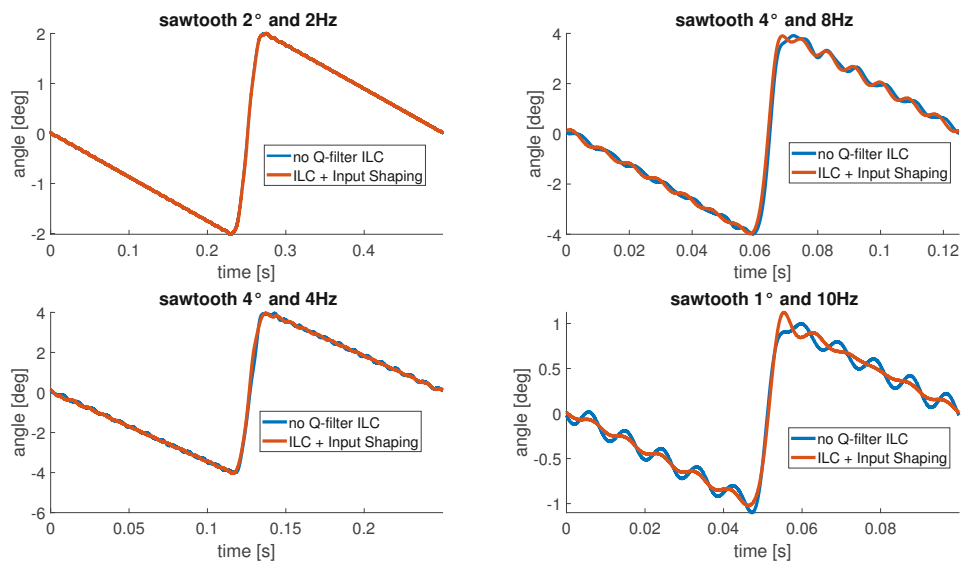


Figure 4.20: Four different sawtooth parameter angle signal comparison between ILC with simple low-pass Q-filter and ILC combined with input shaping. Top left shows an example, where the input shaping performance is much worse than the ILC from previous chapter. Top right shows an example, where input shaping performance is not as good as ILC from previous chapter. Bottom left shows an example, where input shaping performance is a little bit better than ILC from previous chapter. Bottom right shows an example, where input shaping performance better than ILC performance from previous chapter.

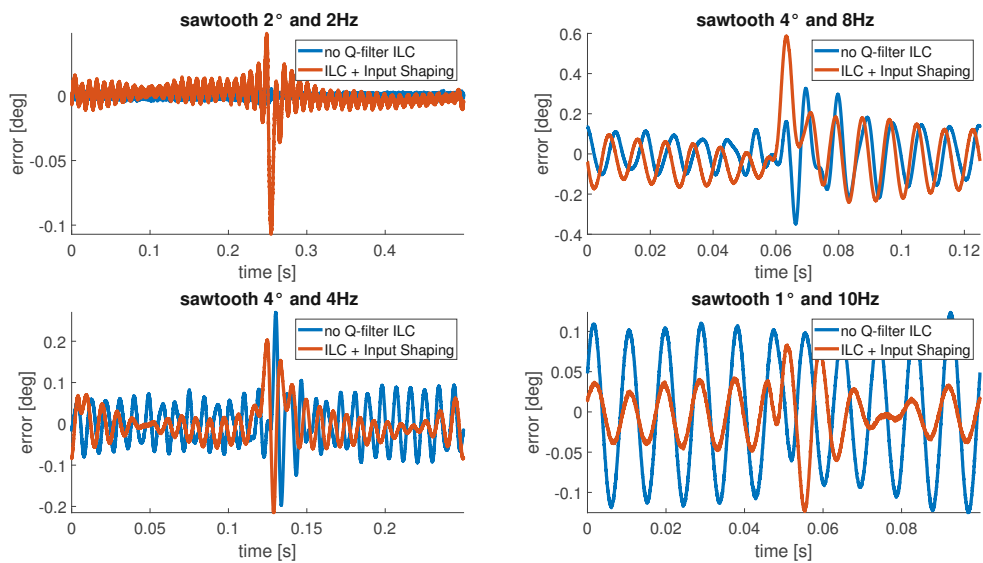


Figure 4.21: Four different sawtooth parameter error signal comparison between ILC with simple low-pass Q-filter and ILC combined with input shaping. Top left shows an example, where the input shaping performance is much worse than the ILC from previous chapter. Top right shows an example, where input shaping performance is not as good as ILC from previous chapter. Bottom left shows an example, where input shaping performance is a little bit better than ILC from previous chapter. Bottom right shows an example, where input shaping performance better than ILC performance from previous chapter

4.5 ILC with Feedback Control

Combining feedback controller together with the ILC is a good practice to increase the overall performance of the system. The feedback controller does help to compensate nonrepeating error, which the ILC cannot compensate. Additionally, by using a PD controller as feedback controller, the resonance peak from the mirror can be reduced, making the system easier to handle and, therefore, increasing the performance of the ILC. As feedback controller, a PD controller is used together with an observer, which is described in [9].

The controller values are

$$k_P = 13478. \quad (4.6)$$

$$k_D = 635.8874. \quad (4.7)$$

The observer gain is selected as

$$l_1 = 2\lambda = 11305, \quad (4.8)$$

$$l_2 = \lambda^2 = 3.1949 \cdot 10^7. \quad (4.9)$$

The complete block diagram of the feedback controller together with the feed forward signal can be seen in Figure 4.22. Since by adding the feedback controller, the transfer function of the system is changed for the ILC. The transfer function is again measured with the same method as described in subsection 4.2.1.

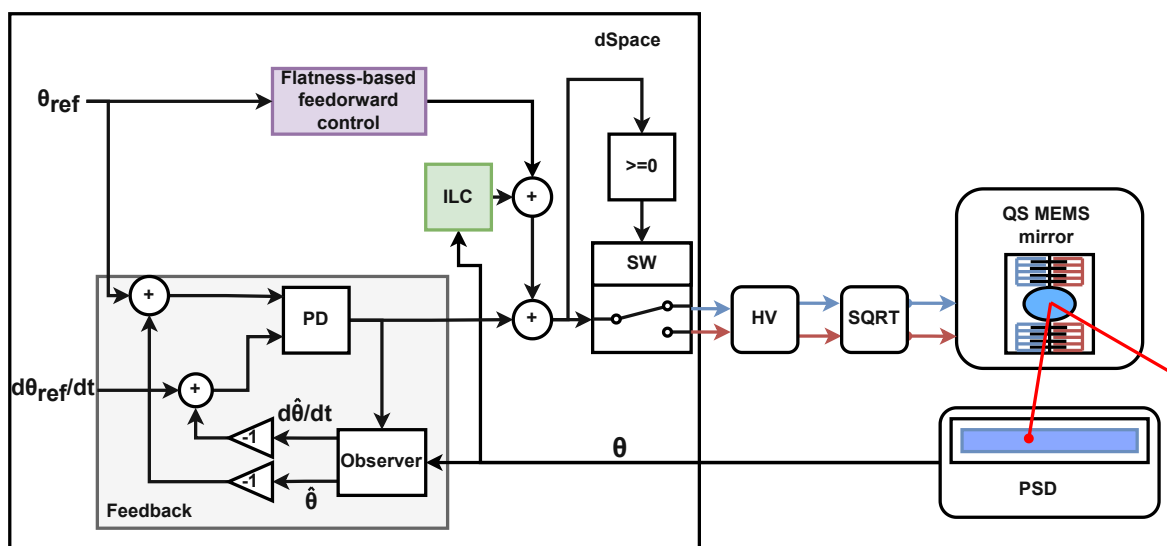


Figure 4.22: Block diagram of the feedback controller together with the feed forward signal. The feed forward signal is calculated through the flatness based feed forward controller and ILC.

Figure 4.23 shows the RMS error for the feedforward with feedback only case and Figure 4.24 shows the RMS error after adding the ILC to the system. By adding the

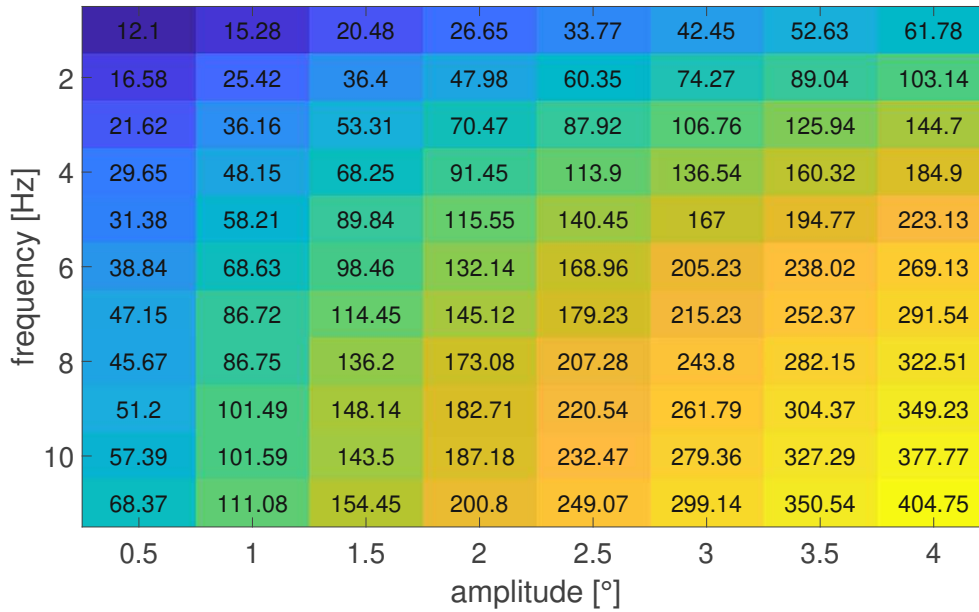


Figure 4.23: RMS error for the feedforward with feedback only case.

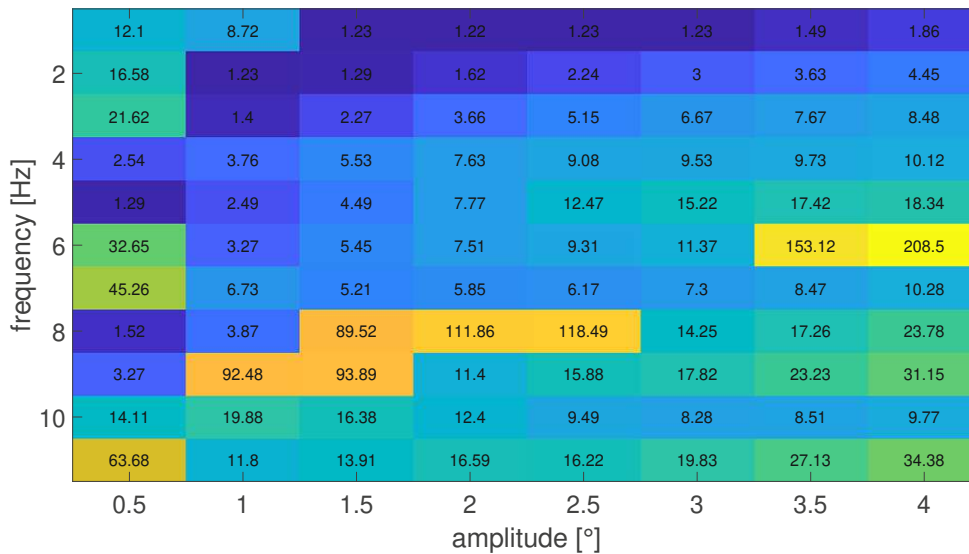


Figure 4.24: [RMS error for the feedforward with feedback and ILC ca

ILC to the feedforward and feedback case, it is possible to obtain a reduction in the RMS error in all cases. Similarly to the case without feedback, the effect of the ILC variant to the different sawtooth cases.

Also interesting to see is if adding the feedback controller significantly increases the performance. Figure 4.25 show the performance factor between the RMS error after the ILC learning process with a simple low-pass filter and the ILC combined with the feedback controller. In high parameter ranges, adding the feedback controller to the

system helps to further reduce the RMS error. An example of this can be seen in 4.26(b), where the error signal is drawn. Here, it is visible that the oscillation error was further reduced. For the lower parameter set of the sawtooth signal, the feedback decreases the efficiency of the ILC. An example can be seen in 4.26(a). In the middle parameter range, the factor is around 0, which means that the ILC performance is about the same, when the feedback controller is added. By adding the feedback controller, an improvement in performance of 63.6% of all cases compared to the ILC without the feedback controller can be achieved.

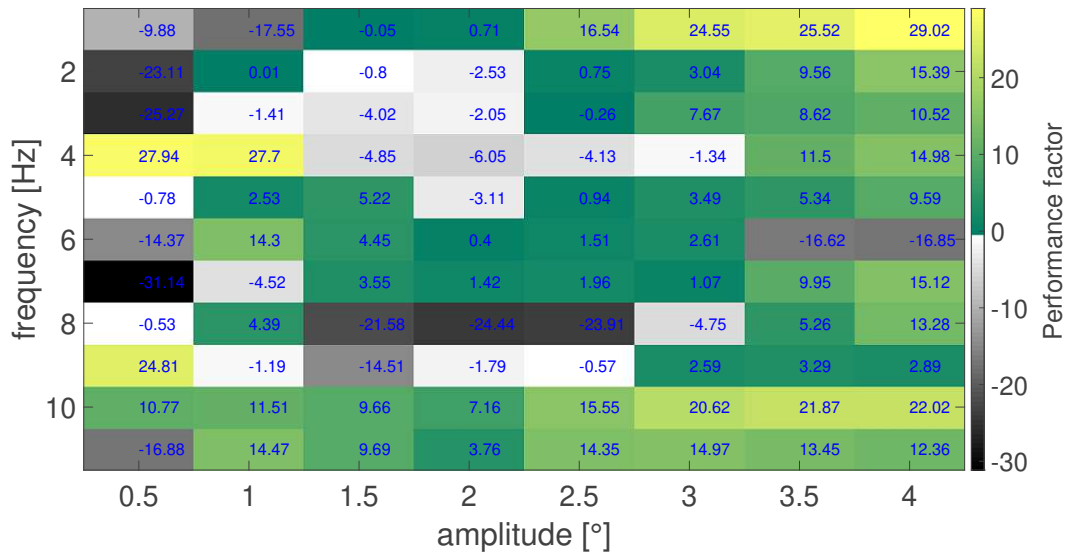


Figure 4.25: Performance factor diagram. Comparison between the RMS error after the learning between ILC with simple low-pass filter and feedback combined with ILC with simple low-pass filter. The factor was calculated with Equation 4.4. A factor value > 0 means that the feedback system has a lower RMS error value, then the simple low-pass filter.

4.6 Discussion

In general, the results of the four methods demonstrate the feasibility of compensating the error of the trajectory from the model uncertainty and oscillation at the eigenfrequency from the input switching problem. For a 2 Hz sawtooth reference trajectory with a 2° amplitude, the flatness-based feedforward only case has an RMS error of 84.8 millidegrees. The flatness-based feedforward control with ILC can reduce the RMS error by a factor of 69.9 down to 1.2 millidegrees. Analyzing the performance for a variety of sawtooth reference signals shows that the performance decreases as the frequency and amplitude increase and for most cases the ILC diverges. The flatness-based feedforward control with ILC and time-variant Q-filter has an RMS error of 7.6 millidegrees for the 2 Hz and 2° amplitude case. Adding the time-variant Q-filter can increase convergence from 29.5% of all cases to 78.4%, but it comes with the cost of a reduction of performance for 87.5% of all sawtooth cases. Flatness-based

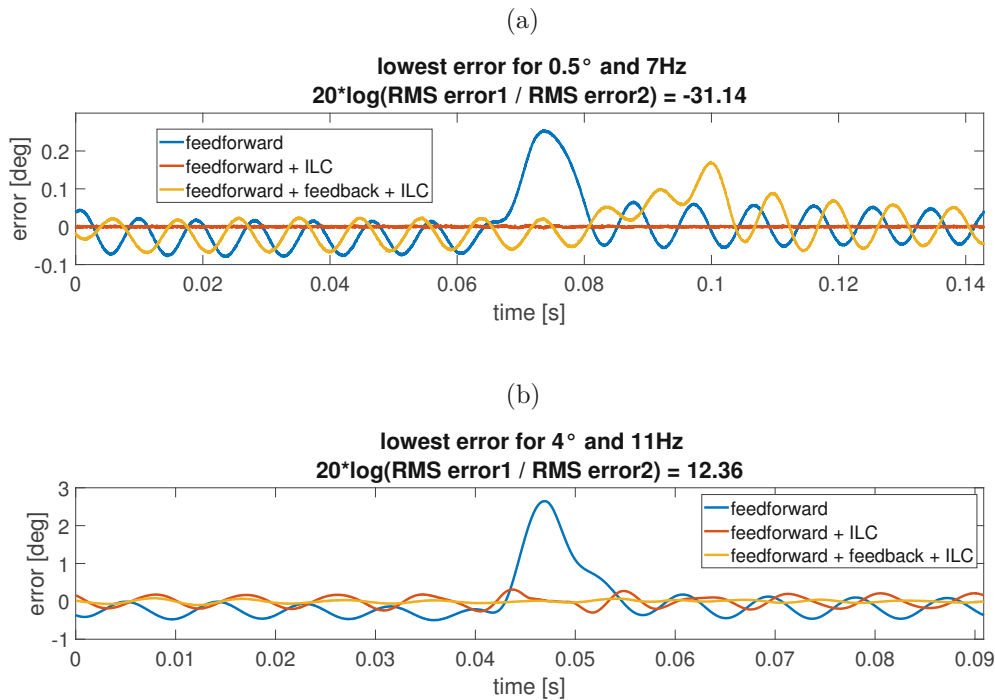


Figure 4.26: Two different results for the feedback with simple low-pass Q-filter. (a) shows the worst example where by adding the feedback, the ILC efficiency was reduced. Only the model error in the fast part of the sawtooth was reduced. (b) shows an example where adding the feedback increased the efficiency of the ILC

feedforward control with ILC with lower bandwidth and input shaping has an RMS error of 12.1 millidegrees for the 2 Hz and 2° amplitude case. Testing this method with different sawtooth cases shows that the RMS error can be reduced for all cases, but the performance also decrease for increasing sawtooth parameters. Comparing the different sawtooth cases shows a reduction of performance for 80% of all cases. The flatness-based feedforward control with PD-feedback controller and ILC has a RMS error of 1.6 millidegrees for the specific sawtooth case of 2 Hz frequency and 2° amplitude which is not the best of all methods, but by adding the feedback controller, the performance increase can be achieved for 63.6% of all cases compared to the first method, but some cases are also show a decrease in performance. By adding the ILC to the feedforward with feedback controller case a reduction of the RMS for the tested sawtooth is achieved, but the feedforward with ILC only case still has the sawtooth case with the smallest RMS error. All ILC-based methods can reduce the oscillation from the switching inputs and model errors regardless of high nonlinearity of the QS MEMS mirror, demonstrating the potential of the ILC for the precise and accurate control of the QS MEMS mirror.

5.1 Conclusion

The quasi-static (QS) MEMS mirrors have the advantage of holding a static position or tracking an arbitrary motion in spite of using simple and CMOS-compatible electrostatic actuation. Since the electrostatic force is only a pulling force, however, the QS MEMS mirror is necessary to switch between two electrodes for scanning trajectories with the whole range. This input switching can introduce an unwanted oscillation around the resonance frequency of the MEMS mirror. This thesis focuses on reducing the oscillation as much as possible and iterative learning control and input shaping are investigated as a solution.

Before implementing the different reduction method, the QS MEMS mirror system is analyzed by dynamic error budgeting. A QS MEMS mirror with a PD feedback controller under an external vibration is assumed for calculation, where the vibration profile of LV124 is used for the evaluation. The cumulative power spectrum (CPS) shows that the errors of the system does not depend on the angular operation point of the mirror, and the most error is contributed by the PSD sensor and vibration influence is negligible.

As first method to reduce the oscillation, a frequency-domain iterative learning control combined with a flatness-based feedforward controller is proposed, where the ILC use a simple lowpass Q filter with 200 Hz bandwidth. For a sawtooth reference trajectory with an amplitude of 2° and a frequency of 2 Hz the RMS error is reduced from 84.82 mdeg to 1.2 mdeg, which is a reduction by a factor of 69.9. The reduced RMS error coincides with the RMS error result of the DEB of 1.3 mdeg. Testing the ILC for a variety of sawtooth references from 1° to 4° and 1 Hz to 10 Hz shows that the ILC performance decreases with increasing sawtooth amplitude and frequency. As the next ILC method, a time-variant Q-filter is used for the ILC to achieve convergence for all parameters as a mean to increase the performance. The time-variant Q-filter based on the Butterworth-filter with crossover frequency at 160 Hz and 100 Hz is used. The time-variant Q-filter shows an improvement in convergence from 29.5% of all cases to

78.4% but has a reduction in performance up to 87.5%. As next method, input shaping, in form of adding impulses to the input signal, in combination with ILC from the first method with lower bandwidth is used. Comparing the input shaping method with the first method shows a reduction of performance for 80% of all sawtooth trajectory cases for the input shaping method, but still has a reduction of the RMS error for all tested sawtooth cases. As last ILC method, the frequency-domain ILC is combined with a feedback PD controller. The ILC with the feedback control improves the RMS error for 63.6% cases of all sawtooth trajectories compared to the ILC with feedforward control. Comparison of the results of all methods shows that the feedforward with ILC only case has the sawtooth case with the lowest RMS error while general RMS reduction performance is better with feedback control. The time-variant Q filter and input shaping also shows the benefits but only for special cases and specific aspects such as convergence and simplicity. In conclusion, ILC and input shaping successfully demonstrate the feasibility of reducing the oscillation introduced through input switching in a quasi-static MEMS mirror and DEB confirms that the reduction can reach the limitation of the optical feedback.

5.2 Outlook

Possible next steps can be raised as follows:

- Further tests of the time-variant Q-filter algorithm showed that the algorithm may introduce some errors in the system. Improving the algorithm could improve the performance with time-variant Q-filter
- The best RMS reduction gives the setup with a simple low-pass filter. Trying another method of Q-filter could resolve in better convergence and better performance. This could also improve the result of the ILC with feedback controller.
- In the current setup for the input shaping method, the position and strength of the impulse is manually set. For a better result, a heuristic finding algorithm could be used or a reinforcement learning algorithm.

Bibliography

- [1] J. Huang, Q. Wen, Q. Nie, F. Chang, Y. Zhou, and Z. Wen, “Miniaturized nir spectrometer based on novel moems scanning tilted grating,” *Micromachines*, vol. 9, p. 478, 09 2018.
- [2] Y. Liu, L. Wang, Y. Su, Y. Zhang, Y. Wang, and Z. Wu, “Alscn piezoelectric mems mirrors with large field of view for lidar application,” *Micromachines*, vol. 13, no. 9, 2022. [Online]. Available: <https://www.mdpi.com/2072-666X/13/9/1550>
- [3] D. Brunner, H. Yoo, T. Thurner, and G. Schitter, “Data based modelling and identification of nonlinear sdof moems mirror,” 03 2019, p. 43.
- [4] R. Schroedter, *Modellbasierter Systementwurf zur Steuerung und Regelung quasi-statischer Mikroscoannerspiegel mit elektrostatischem Kammantrieb*. Jörg Vogt Verlag, 2018.
- [5] Volkswagen AG, “Electric and electronic components in motor vehicles up to 3,5 t - general requirements, test conditions and tests,” 2013.
- [6] U. Weiss and P. Biber, “Plant detection and mapping for agricultural robots using a 3d lidar sensor,” *Robotics and Autonomous Systems*, vol. 59, no. 5, pp. 265–273, 2011, special Issue ECMR 2009. [Online]. Available: <https://www.sciencedirect.com/science/article/pii/S0921889011000315>
- [7] W. O. Davis, R. Sprague, and J. Miller, “Mems-based pico projector display,” in *2008 IEEE/LEOS International Conference on Optical MEMS and Nanophotonics*, 2008, pp. 31–32.
- [8] T. Xie, H. Xie, G. Fedder, and Y. Pan, “Endoscopic optical coherence tomography with new mems mirror,” *Electronics Letters*, vol. 39, pp. 1535 – 1536, 11 2003.
- [9] R. Schroedter, M. Schwarzenberg, J. Grahmann, T. Sandner, and K. Janschek, “Repetitive nonlinear control for linear scanningmicro mirrors,” 01 2018.

Bibliography

- [10] R. Schroedter, M. Roth, K. Janschek, and T. Sandner, "Flatness-based open-loop and closed-loop control for electrostatic quasi-static microscanners using jerk-limited trajectory design," *Mechatronics*, vol. 56, pp. 318–331, 2018. [Online]. Available: <https://www.sciencedirect.com/science/article/pii/S0957415817300363>
- [11] T. Juneau, K. Unterkofler, T. Seliverstov, S. Zhang, and M. Judy, "Dual-axis optical mirror positioning using a nonlinear closed-loop controller," in *TRANSDUCERS '03. 12th International Conference on Solid-State Sensors, Actuators and Microsystems. Digest of Technical Papers (Cat. No.03TH8664)*, vol. 1, 2003, pp. 560–563 vol.1.
- [12] H. Chen, M. Pallapa, W. Sun, Z. Sun, and J. Yeow, "Nonlinear control of an electromagnetic polymer mems hard-magnetic micromirror and its imaging application," *Journal of Micromechanics and Microengineering*, vol. 24, 03 2014.
- [13] W. Wang, Q. Chen, D. Wang, L. Zhou, and H. Xie, "A bi-directional large-stroke electrothermal mems mirror with minimal thermal and temporal drift," in *2017 IEEE 30th International Conference on Micro Electro Mechanical Systems (MEMS)*, 2017, pp. 331–334.
- [14] S. Gu-Stoppel, T. Lisec, S. Fichtner, N. Funck, C. Eisermann, F. Lofink, B. Wagner, and A. Müller-Groeling, "A highly linear piezoelectric quasi-static MEMS mirror with mechanical tilt angles of larger than 10° ," in *MOEMS and Miniaturized Systems XVIII*, W. Piyawattanametha, Y.-H. Park, and H. Zappe, Eds., vol. 10931, International Society for Optics and Photonics. SPIE, 2019, p. 1093102. [Online]. Available: <https://doi.org/10.1117/12.2509577>
- [15] H. Schenk, T. Sandner, C. Drabe, T. Klose, and H. Conrad, "Single crystal silicon micro mirrors," *physica status solidi (c)*, vol. 6, pp. 728 – 735, 03 2009.
- [16] H. Urey, "Mems scanners for display and imaging applications," in *Optomechatronic Micro Nano Components, Devices, and Systems*, Y. Katagiri, Ed., vol. 5604, International Society for Optics and Photonics. SPIE, 2004, pp. 218 – 229. [Online]. Available: <https://doi.org/10.1117/12.580450>
- [17] N. Boni, R. Carminati, G. Mendicino, and M. Merli, "Quasi-static PZT actuated MEMS mirror with $4 \times 3 \text{mm}^2$ reflective area and high robustness," in *MOEMS and Miniaturized Systems XX*, H. Zappe, W. Piyawattanametha, and Y.-H. Park, Eds., vol. 11697, International Society for Optics and Photonics. SPIE, 2021, p. 1169708. [Online]. Available: <https://doi.org/10.1117/12.2576526>
- [18] U. Baran, D. Brown, S. Holmstrom, D. Balma, W. Davis, A. Mazzalai, P. Muralt, and H. Urey, "High frequency torsional mems scanner for displays," *Proceedings of the IEEE International Conference on Micro Electro Mechanical Systems (MEMS)*, pp. 636–639, 01 2012.
- [19] J. Zhong, X. Xiong, Z. Yao, J. Hu, and P. Patra, "Design and optimization of piezoelectric dual-mode micro-mirror," *Technological Developments in Networking, Education and Automation*, 01 2010.

Bibliography

- [20] J. Grahmann, A. Dreyhaupt, C. Drabe, R. Schroedter, J. Kamenz, and T. Sandner, “Mems-mirror based trajectory resolution and precision enabled by two different piezoresistive sensor technologies,” 03 2016, p. 976006.
- [21] D. Brunner, *Evaluation of resonant MEMS scanner for optical ranging application*, Masterthesis, TU Wien, 2017.
- [22] K. Koh, T. Kobayashi, and C. Lee, “Investigation of piezoelectric driven mems mirrors based on single and double s-shaped pzt actuator for 2-d scanning applications,” *Sensors and Actuators A: Physical*, vol. 184, pp. 149–159, 09 2012.
- [23] D. Brunner, *Design and Evaluation of Resonant MEMS Scanning Systems for High Performance Automotive Applications*, Wien, 2022.
- [24] W. Shahid, Z. Qiu, X. Duan, H. Li, T. D. Wang, and K. R. Oldham, “Modeling and simulation of a parametrically resonant micromirror with duty-cycled excitation,” *Journal of Microelectromechanical Systems*, vol. 23, no. 6, pp. 1440–1453, 2014.
- [25] J. M. Londoño, S. A. Neild, and J. E. Cooper, “Identification of backbone curves of nonlinear systems from resonance decay responses,” *Journal of Sound and Vibration*, vol. 348, pp. 224–238, 2015. [Online]. Available: <https://www.sciencedirect.com/science/article/pii/S0022460X15002333>
- [26] D. Mukhopadhyay, D. Antonio, I. W. Jung, and D. Lopez, “Self sustained oscillation of mems torsional micromirrors,” in *MOEMS and Miniaturized Systems XI*, H. Schenk, W. Piyawattanametha, and W. Noell, Eds., vol. 8252, International Society for Optics and Photonics. SPIE, 2012, pp. 252 – 257. [Online]. Available: <https://doi.org/10.1117/12.906746>
- [27] Y. Zhao, F. E. Tay, G. Zhou, and F. S. Chau, “Fast and precise positioning of electrostatically actuated dual-axis micromirror by multi-loop digital control,” *Sensors and Actuators A: Physical*, vol. 132, no. 2, pp. 421–428, 2006. [Online]. Available: <https://www.sciencedirect.com/science/article/pii/S0924424706001567>
- [28] V. Utkin and J. Lee, “Chattering problem in sliding mode control systems,” 07 2006, pp. 346 – 350.
- [29] C. Hui, S. ZhenDong, S. WeiJie, and T. W. Y. John, “Twisting sliding mode control of an electrostatic mems micromirror for a laser scanning system,” in *2015 34th Chinese Control Conference (CCC)*, 2015, pp. 8331–8336.
- [30] Y. Wang, F. Gao, and F. J. Doyle, “Survey on iterative learning control, repetitive control, and run-to-run control,” *Journal of Process Control*, vol. 19, no. 10, pp. 1589–1600, 2009. [Online]. Available: <https://www.sciencedirect.com/science/article/pii/S0959152409001681>
- [31] J. Li and T.-C. Tsao, “Robust Performance Repetitive Control Systems,” *Journal of Dynamic Systems, Measurement, and Control*, vol. 123, no. 3, pp. 330–337, 01 1998. [Online]. Available: <https://doi.org/10.1115/1.1387015>

Bibliography

- [32] T. Glück, A. Kugi, and A. Steinböck, *Fortgeschrittene Methoden der nichtlinearen Regelung*. Wien: ACIN, 2021. [Online]. Available: <https://www.acin.tuwien.ac.at/file/teaching/master/fortgeschrMethodenNichtlinReg/WS2020/FMNR.pdf>
- [33] D. Bristow, M. Tharayil, and A. Alleyne, “A survey of iterative learning control,” *IEEE Control Systems Magazine*, vol. 26, no. 3, pp. 96–114, 2006.
- [34] M. Tomizuka, “Zero phase error tracking algorithm for digital control,” *Journal of Dynamic Systems Measurement and Control-transactions of The Asme - J DYN SYST MEAS CONTR*, vol. 109, 05 1987.
- [35] Z. Cai, C. T. Freeman, P. L. Lewin, and E. Rogers, “Iterative learning control for a non-minimum phase plant based on a reference shift algorithm,” *Control Engineering Practice*, vol. 16, no. 6, pp. 633–643, 2008, special Section on Large Scale Systems. [Online]. Available: <https://www.sciencedirect.com/science/article/pii/S0967066107001372>
- [36] H. W. Yoo, S. Ito, and G. Schitter, “High speed laser scanning microscopy by iterative learning control of a galvanometer scanner,” *Control Engineering Practice*, vol. 50, pp. 12–21, 2016. [Online]. Available: <https://www.sciencedirect.com/science/article/pii/S096706611630020X>
- [37] S. Tien, Q. Zou, and S. Devasia, “Iterative control of dynamics-coupling-caused errors in piezoscanners during high-speed afm operation,” *IEEE Transactions on Control Systems Technology*, vol. 13, no. 6, pp. 921–931, 2005.
- [38] H. W. Yoo, C. J. Kerschner, S. Ito, and G. Schitter, “Iterative learning control for laser scanning based micro 3d printing,” *IFAC-PapersOnLine*, vol. 52, no. 15, pp. 169–174, 2019, 8th IFAC Symposium on Mechatronic Systems MECHATRONICS 2019. [Online]. Available: <https://www.sciencedirect.com/science/article/pii/S2405896319316581>
- [39] C. Hua, Y. Qiu, and X. Guan, “Enhanced model-free adaptive iterative learning control with load disturbance and data dropout,” *International Journal of Systems Science*, vol. 51, no. 11, pp. 2057–2067, 2020. [Online]. Available: <https://doi.org/10.1080/00207721.2020.1784492>
- [40] S. Ito, H. W. Yoo, and G. Schitter, “Comparison of modeling-free learning control algorithms for galvanometer scanner’s periodic motion,” in *2017 IEEE International Conference on Advanced Intelligent Mechatronics (AIM)*, 2017, pp. 1357–1362.
- [41] K.-S. Kim and Q. Zou, “A modeling-free inversion-based iterative feedforward control for precision output tracking of linear time-invariant systems,” *IEEE/ASME Transactions on Mechatronics*, vol. 18, no. 6, pp. 1767–1777, 2013.
- [42] Y. Li and J. Bechhoefer, “Model-free iterative control of repetitive dynamics for high-speed scanning in atomic force microscopy,” *The Review of scientific instruments*, vol. 80, p. 013702, 02 2009.

Bibliography

- [43] E. Madadi and D. Söffker, “Comparison of different model-free iterative learning control methods concerning a nonlinear mechanical structure,” in *2017 11th Asian Control Conference (ASCC)*, 2017, pp. 1560–1565.
- [44] M. Tharayil and A. Alleyne, “A time-varying iterative learning control scheme,” 01 2004, pp. 3782 – 3787 vol.4.
- [45] D. A. Bristow, A. Alleyne, and M. Tharayil, “A time-varying q-filter design for iterative learning control,” in *2007 American Control Conference*, 2007, pp. 5503–5508.
- [46] B. Cong, J. Schlarp, and G. Schitter, “Iterative learning control for the active error correction of polygon mirror based laser scanning,” in *2022 IEEE/ASME International Conference on Advanced Intelligent Mechatronics (AIM)*, 2022, pp. 522–527.
- [47] V. Milanović, A. Kasturi, H. J. Kim, and F. Hu, “Iterative learning control algorithm for greatly increased bandwidth and linearity of mems mirrors in lidar and related imaging applications,” in *MOEMS and Miniaturized Systems XVII*, W. Piyawattanametha, Y.-H. Park, and H. Zappe, Eds., vol. 10545, International Society for Optics and Photonics. SPIE, 2018, p. 1054513. [Online]. Available: <https://doi.org/10.1117/12.2291428>
- [48] M. P. Chaffe and L. Y. Pao, “Iterative learning control for near-field scanning optical microscope applications,” in *2011 IEEE International Conference on Control Applications (CCA)*, 2011, pp. 1075–1080.
- [49] A. Shkoruta, W. Caynoski, S. Mishra, and S. Rock, “Iterative learning control for power profile shaping in selective laser melting,” in *2019 IEEE 15th International Conference on Automation Science and Engineering (CASE)*, 2019, pp. 655–660.
- [50] J. v. E. L. Jabben, “Dynamic error budgeting. performance analysis and design of mechatronic systems.” *Mikroniek*, vol. 51, pp. 5–11, 2011.
- [51] W. Monkhorst, “Dynamic error budgeting: A design approach,” 2004.
- [52] R. Munnig Schmidt, G. Schitter, and J. van Eijk, *The Design of High Performance Mechatronics*. Delft University Press, 2011.
- [53] T. Riel, R. Saathof, A. Katalenic, and G. Schitter, “Noise analysis and improvement of a permanent magnet synchronous motor by dynamic error budgeting,” *IFAC-PapersOnLine*, vol. 49, no. 21, pp. 339–346, 2016, 7th IFAC Symposium on Mechatronic Systems MECHATRONICS 2016. [Online]. Available: <https://www.sciencedirect.com/science/article/pii/S2405896316321681>
- [54] S. Garrido, M. Abderrahim, A. Gimenez, R. Diez, and C. Balaguer, “Anti-swinging input shaping control of an automatic construction crane,” *IEEE Transactions on Automation Science and Engineering*, vol. 5, no. 3, pp. 549–557, 2008.

Bibliography

- [55] A. Component, W. Singhose, N. Singer, and W. Seering, “Comparison of command shaping methods for reducing residual vibration,” vol. 2, 03 1996.
- [56] G. Schitter, P. J. Thurner, and P. K. Hansma, “Design and input-shaping control of a novel scanner for high-speed atomic force microscopy,” *Mechatronics*, vol. 18, no. 5, pp. 282–288, 2008, special Section on Optimized System Performances Through Balanced Control Strategies. [Online]. Available: <https://www.sciencedirect.com/science/article/pii/S0957415808000202>
- [57] H. W. Yoo, D. Brunner, T. Thurner, and G. Schitter, “Mems test bench and its uncertainty analysis for evaluation of mems mirrors. this work has been supported in part by the austrian research promotion agency (ffg) under the scope of the lidcar project (ffg project number 860819),” *IFAC-PapersOnLine*, vol. 52, no. 15, pp. 49–54, 2019, 8th IFAC Symposium on Mechatronic Systems MECHATRONICS 2019. [Online]. Available: <https://www.sciencedirect.com/science/article/pii/S2405896319316374>
- [58] B. Lizon, *Fundamentals of Precision ADC Noise Analysis*. Texas Instruments, 2020. [Online]. Available: <https://www.ti.com/lit/eb/slyy192/slyy192.pdf>
- [59] P. V. J. Mr. Vikas G. Gaikwad, “Adc errors affect on system performance,” *International Journal of Current Engineering And Scientific Research (IJCESR)*, vol. 2, pp. 1–18, 2015.
- [60] J. Grahmann, R. Schroedter, O. Kiethe, and U. Todt, “Vibration analysis of micro mirrors for lidar using on-chip piezo-resistive sensor,” 02 2020, p. 7.
- [61] H. W. Yoo, R. Riegler, D. Brunner, S. Albert, T. Thurner, and G. Schitter, “Experimental evaluation of vibration influence on a resonant mems scanning system for automotive lidars,” *IEEE Transactions on Industrial Electronics*, vol. 69, no. 3, pp. 3099–3108, 2022.
- [62] A. K. W. Kemmetmüller, *REGELUNGSSYSTEME 1*. Wien: ACIN, 2020. [Online]. Available: https://www.acin.tuwien.ac.at/file/teaching/master/Regelungssysteme-1/VO_Regelungssysteme1_WS2020.pdf

Appendix A

Figure 1 to Figure 5 shows the RMS error in milidegree for different sawtooth reference signal for the 5 different cases. Flatness-based feedforward case only, flatness-based feedforward control with ILC, flatness-based feedforward control with ILC and time-variant Q-filter, input shaping with ILC and flatness-based feedforward control with ILC and PD-feedback controller.

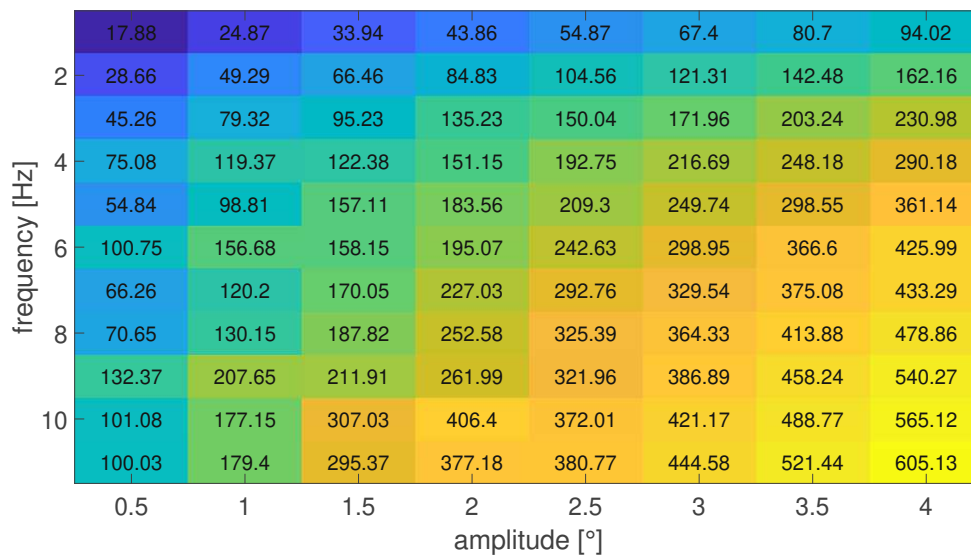


Figure 1: RMS error in milidegree of the feedforward control only case

Appendix A

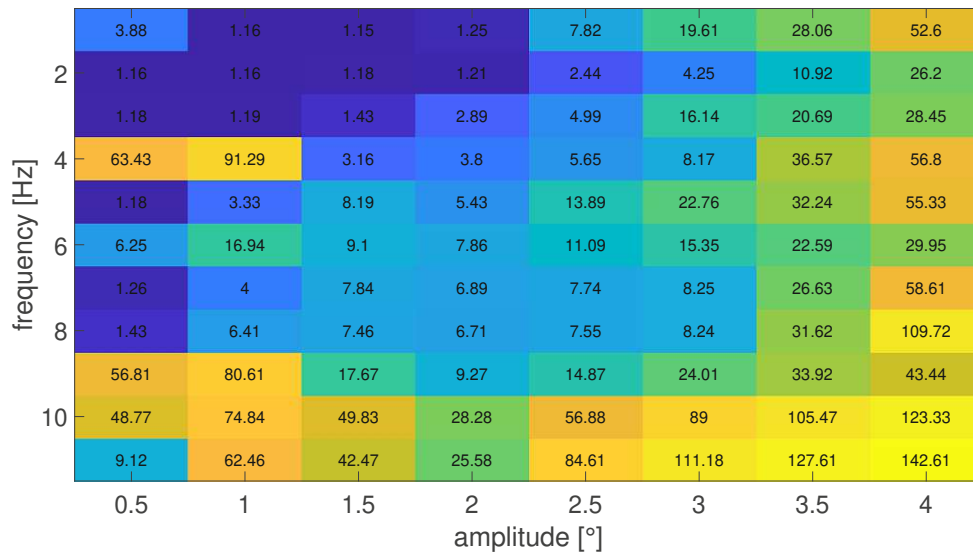


Figure 2: RMS error of the flatness-based feedforward control with ILC

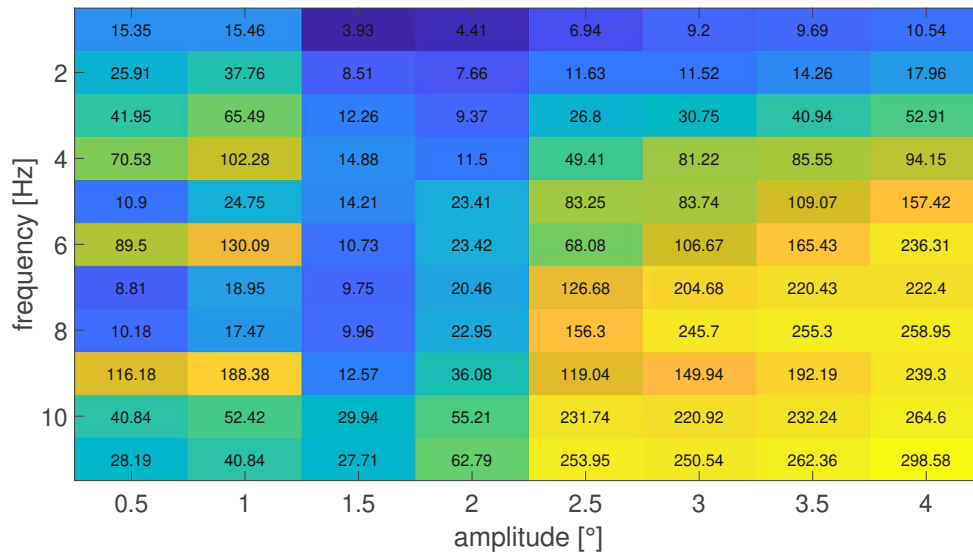


Figure 3: RMS error in milidegree of the flatness-based feedforward control with ILC and time-variant Q-filter

Appendix A

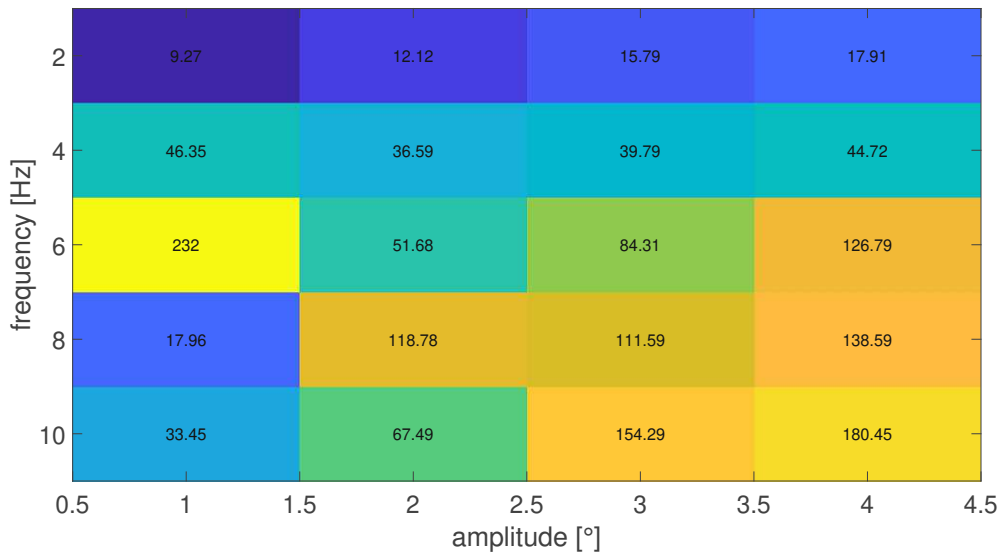


Figure 4: RMS error in milidegree of the input shaping with ILC

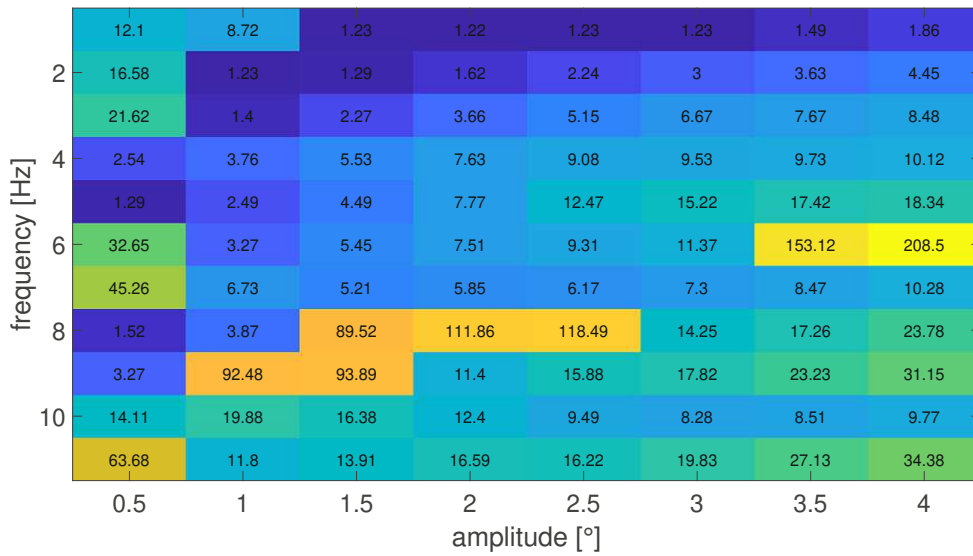


Figure 5: RMS error in milidegree of the flatness-based feedforward control with ILC and PD-feedback controller